UNIVERSITY OF CALIFORNIA SAN DIEGO

Integrative control of breathing and pain by parabrachial opioidergic circuits

A dissertation submitted in partial satisfaction of the
requirements for the degree Doctor of Philosophy

in

Biology

by

Shijia Liu

Committee in charge:

Professor Sung Han, Chair
Professor Matthew Banghart
Professor Edward Callaway
Professor Thomas Hnasko
Professor David Kleinfeld
Professor Byungkook Lim

2022

The Dissertation of Shijia Liu is approved, and it is acceptable in quality and form for publication on microfilm and electronically.

University of California San Diego

2022

TABLE OF CONTENTS

LIST OF FIGURES

LIST OF TABLES

ACKNOWLEDGEMENTS

First and foremost, I would like to thank my Ph.D. advisor, Sung Han, for his guidance and support throughout the past five years. It is my honor to be the first graduate student of your lab, which is an unforgettable and invaluable experience. You taught me the importance of critical thinking and the meaning of resilience, and I am forever grateful for your mentorship and trust.

I also thank my wonderful colleagues in the Han lab, Sukjae Joshua Kang, Mao Ye, Jinho Jhang, Dong-Il Kim, and Jong-Hyun Kim, for being my teachers, teammates, role models, and friends. I learned so much from each one of you. I want to thank my collaborators, Gerald Pao, Xiangyu Ren, Hanqing Liu, and neighbors at Salk, particularly the Kuo-Fen Lee lab, for expanding my research horizons and providing stimulating discussions. I also thank my undergraduate mentees, Samuel Song, Annie Haibei Jiang, and Ashley Lanling Jia, as well as rotation students, Desiree Chu, Benjamin Roberts, and Qiurui Zeng, for bringing your unique talents, energy, and passion into the lab.

I would also like to acknowledge my committee members, Matthew Banghart, Edward Callaway, Thomas Hnasko, David Kleinfeld, and Byungkook Lim, for your generous support and guidance throughout my graduate experience. Your brilliant insights have shaped both my projects and my scientific career.

Importantly, I thank my friends in San Diego and beyond, who always bring me laughter, inspiring stories, and tons of luck. Special thanks to those of you at UCSD and Salk; it has been a fun rollercoaster ride with you, and I am beyond excited to see what your future holds.

Finally, I would like to thank my parents and extended family for their love and support. It is a privilege to have parents whom I admire, who process excellent scientific insights while being first-class therapists and travel companions. You have continuously

inspired me with your devotion to lifelong learning, connecting with others, and creating a better world.

Chapter 2, in full, is a reprint of the material as it appears in **Liu, S.**, Ye, M., Pao, G.M., Song, S., Jhang, J., Jiang, H., Kim, J.H., Kang, S., Kim, D., Han, S. Divergent brainstem opioidergic pathways that coordinate breathing with pain and emotions. *Neuron*, (2021). S0896-6273(21)00990-9. The dissertation author was a primary investigator and the first author of this material.

Chapter 3, in full, is a reprint of the material as it appears in **Liu, S.**, Kim, D.I., Oh, T.G., Pao, G.M., Kim, J.H., Palmiter, R.D., Banghart, M.R., Lee, K.F., Evans, R.M., Han, S. Neural basis of opioid-induced respiratory depression and its rescue. *Proc. Natl. Acad. Sci.,* 2021, 118(23). The dissertation author was a primary investigator and the first author of this material.

VITA

2012 - 2016 B.S. in Biology (honors), Shandong University

2016 - 2022 Ph.D. in Biology, University of California San Diego

Thesis advisor: Sung Han (Salk Institute for Biological Studies)

PUBLICATION

Liu, S., Ye, M., Pao, G.M., Song, S., Jhang, J., Jiang, H., Kim, J.H., Kang, S., Kim, D., Han, S. Divergent brainstem opioidergic pathways that coordinate breathing with pain and emotions. *Neuron*, (2021).

Liu, S., Kim, D.I., Oh, T.G., Pao, G.M., Kim, J.H., Palmiter, R.D., Banghart, M.R., Lee, K.F., Evans, R.M., Han, S. Neural basis of opioid-induced respiratory depression and its rescue. *Proc. Natl. Acad. Sci.,* 2021, 118(23).

MANUSCRIPT IN PREPARATION

Kang, S.J.*, **Liu, S.***, Ye, M., Kim, D.I., Pao, G.M., Copits, B.A., Bruchas, M.R., Lee, K.F., Roberts, B.Z., Han, S. A central alarm system that gates multisensory innate threat cues to the amygdala. *Under revision.*

Ren. X.*, Acton, D.*, **Liu, S.***, Virlogeux, A., Han, S.$^{\#}$, Goulding, M.$^{\#}$. A dedicated spinoparabrachial pathway for mechanical itch. *Manuscript in preparation.*

ABSTRACT OF THE DISSERTATION

Integrative control of breathing and pain by parabrachial opioidergic circuits

by

Shijia Liu

Doctor of Philosophy in Biology

University of California San Diego, 2022

Professor Sung Han, Chair

Breathing and pain perception are often investigated as separate behaviors, yet they are tightly connected. For example, severe pain induces hyperventilation, whereas paced slow breathing alleviates perceived pain. Moreover, opioids can reduce pain while resulting in opioid-induced respiratory depression (OIRD), which is the direct cause of death in opioid overdose. Yet, the neurobiological mechanisms of breathing-pain interaction and how their balance is disrupted by opioid overdose are not well understood.

This dissertation describes original work investigating the neural circuit mechanisms of how *Oprm1* (μ-opioid receptor)-expressing neurons in the lateral parabrachial nucleus

(PBL) coordinate breathing with pain and emotions in mice. Exogenous opioids modulate these neurons, which in turn are involved in the expression and rescue of OIRD. Together, these results highlight parabrachial opioidergic pathways as critical nodes for orchestrating breathing and pain, as well as therapeutic candidates for developing side-effect-free painkillers and OIRD treatments.

Chapter 1: Introduction

1.1 The breathing control network

Breathing is a fundamental, life-sustaining function for animals (Dick et al., 2018). The neural circuitry of breathing in mammals is largely conserved (Alheid et al., 2004). There are three critical respiratory centers in the brain, namely, the ventral respiratory group (VRG), the dorsal respiratory group (DRG), and the pontine respiratory group (PRG). The VRG and DRG are located in the medulla and generate the breathing rhythm (Cui et al., 2016; Del Negro et al., 2018; Tan et al., 2010). DRG neurons are activated during inspiration and are located in the nucleus tractus solitarius (NTS). VRG neurons are activated during both inspiration and expiration and are located in the ventrolateral column of the medulla (from the facial nucleus to the rostral cervical spinal cord). VRG also contains the majority of breathing rhythm generation centers: the pre-Bötzinger Complex (preBötC; inspiratory), the lateral parafacial nucleus (pF_L; expiratory), the ventral parafacial respiratory group (pF_V; chemosensitive, rhythmogenic in the perinatal period only), and the post-inspiratory complex (PiCo; possibly mediating post-inspiration) (Ashhad and Feldman, 2020; Del Negro et al., 2018).

PRG comprises the parabrachial (PB) and Kölliker-Fuse (KF) nuclei in the dorsolateral pons, as well as the intertrigeminal region in the central pons (Dutschmann and Dick, 2012). Opposite to the VRG, the PRG neurons are not involved in generating the breathing rhythm, as the rhythm continues after PRG removal in decerebrated animals (Wang et al., 1957). Instead, the PRG has been proposed to modulate the changes in overall breathing rhythm in response to interoceptive and exteroceptive signals due to its location at the crossroads of forebrain limbic structures and medullary respiratory centers (Dutschmann and Dick, 2012). For example, hypoxia (low levels of blood O_2) or hypercapnia (high levels of blood CO_2) activates PB neurons to increase respiratory rhythm and bring blood oxygen

levels back to normal. Moreover, silencing PB neurons by injecting the GABA agonist, muscimol, attenuated the respiratory response to cutaneous noxious stimulation (Jiang et al., 2004).

The PB complex includes at least 11 cytoarchitectonically distinct subnuclei surrounding the superior cerebellar peduncle (Fulwiler and Saper, 1984). Compared to its neighbor, KF, which is the well-known “inspiratory off-switch” (the transition from inspiration to expiration) (Dutschmann and Dick, 2012; Dutschmann and Herbert, 2006), PB plays multiple different roles in breathing, such as inspiratory facilitation (hyperpnea), expiratory facilitation (apneusis), and prevention of breathing (apnea). These different roles were nicely illustrated by injecting glutamate into distinct PB subregions, which resulted in specific and sometimes opposing effects in breathing (Chamberlin and Saper, 1994). To better understand the contribution of PB in breathing modulation, one strategy is to dissociate the roles of specific cell types by manipulating and recording their activities during breathing with better spatial and temporal resolutions, which is one of the main goals of this dissertation.

1.2 The coupling of breathing with other behaviors

Besides its life-sustaining role in maintaining physical homeostasis, breathing has been reported to bidirectionally influence other behaviors. These behaviors include orofacial behaviors such as sniffing and whisking, vocalization, emotion, and pain, as described below.

1.2.1 Orofacial behavior

In rodents, olfactory signaling has been well documented to be tightly coupled to breathing across various frequencies (Cury and Uchida, 2010; Uchida and Mainen, 2003). The brain structures that display synchronized activity with breathing include the primary

trigeminal neurons that innervate the nasal cavity (Wallois et al., 1991), the olfactory bulb (Moberly et al., 2018; Shusterman et al., 2011), and the olfactory cortex (Miura et al., 2012). Notably, the saliency of odorants can be precisely mapped to the phase of the breathing cycle when mitral cells are activated (Smear et al., 2011).

Synchronization of whisking with breathing was first discovered in the aroused rat in the 1960s (Welker, 1964). Recently, studies have further shown that whisking and sniffing can be robustly phase-locked on a cycle-by-cycle basis, and corresponding cortical areas—vibrissa cortex (for vibrissa touch during exploratory whisking) and olfactory cortex (for odor detection during sniffing)—also displayed synchronized activity (Kleinfeld et al., 2014). The preBötC has been proposed as a “master clock” to synchronize various orofacial behaviors due to its widespread connections to other ventrolateral medulla structures (Moore et al., 2013).

Together, these reports revealed that breathing could serve as a medium to phase-lock the olfactory and touch information for coincidence detection, as well as a broadcast signal to synchronize the global activity.

1.2.2 Vocalization

Voluntary control of respiration is needed during vocalization, including taking a deep breath before speaking and postponing inspiration to complete a sentence (Smotherman et al., 2010). One candidate structure that is thought to mediate the vocal-respiratory interaction is the PB, which receives descending inputs from the vocalizing regions of the anterior cingulate cortex and the laryngeal area of the motor cortex (Jürgens, 1976; Saper, 1982), and is reciprocally connected to the DRG and VRG (Herbert et al., 1990). More PB neurons showed cFos immunoreactivity in vocalizing bats than silent bats (Smotherman et al., 2010). In cats, PB single unit activities synchronized with basal respiration and vocalization (Farley

et al., 1992). Moreover, injecting the GABAA receptor antagonist bicuculline into the lateral PB decreased the call durations in bats (Smotherman et al., 2006). These reports suggest that the PB acts as a state-dependent filter that regulates respiratory behavior according to the vocalization requirements.

1.2.3 Emotion and pain

Breathing rhythms are known to be regulated non-homeostatically by emotional and sensory stimuli (Boiten et al., 1994). Breathing becomes faster and shallower under fearful conditions (Feleky, 1916) and under certain pathophysiological conditions that induce intense emotional changes, such as panic attack, posttraumatic stress disorder (PTSD), or phobias (Bass and Gardner, 1985).

Pain exhibits both emotional and sensory components. Intense and uncontrollable pain induces hyperventilation in humans (Jafari et al., 2017). Conversely, slow breathing is widely used as a non-pharmacological intervention for treating pain (Garland et al., 2017; Garland et al., 2020) and affective disorders, such as anxiety, PTSD, and depression (Arch and Craske, 2006; Garland et al., 2017; Garland et al., 2020; Han et al., 1996).

So far, a few brain regions have been suggested to link emotion with breathing. One candidate is the sighing generation microcircuit in the preBötC and the pF, implicated in controlling physiological and emotional sighing (Li et al., 2016). Another candidate is the Cdh9 (cadherin-9)/Dbx1 (developing brain homeobox 1) double-positive neurons in the preBötC, which promotes arousal via its projection to the locus coeruleus and possibly regulates emotion through the same pathway (Yackle et al., 2017). Other candidate structures outside the breathing central pattern generator include the olfactory bulb, which displays sniffing-related rhythmic activity and associates a particular odor (such as a predator odor) with fear memory through its projection to the prelimbic cortex (Moberly et al., 2018).

To further investigate how breathing can be coordinated with pain and emotions, I focused on the PB in the PRG, which is also a part of the neural network that regulates pain (Peirs and Seal, 2016) and emotions (Janak and Tye, 2015). Chapter 2 of this dissertation will describe the neural circuit mechanisms to achieve such coordinations by a specific neural population in the lateral PB. Namely, the parabrachial nucleus sends bifurcate projections to the breathing center, preBötC, and the pain center, the central amygdala, which differentially regulates breathing, pain, and anxiety. On the other hand, the interaction between breathing and pain or anxiety is achieved through the recurrent excitation of both pathways.

1.3 Breathing and the neuromodulator system

Both endogenous and exogenous signaling molecules have been implicated in the control of breathing. Examples include opioids (Dahan et al., 2001), serotonin (Hodges et al., 2008), orexin (Williams and Burdakov, 2008), cholecystokinin (Ellenberger and Smith, 1999), and substance P (Hedner et al., 1984). Their receptors belong to the G protein-coupled receptor (GPCR) family and are widely expressed in many of the critical breathing centers (Varga et al., 2020). Here, I will focus on the first two signaling molecules, opioids and serotonin, whose roles in breathing have been relatively well described.

1.3.1 Opioids

Opioid drugs are the most commonly used and effective analgesics to treat acute and severe pain. At the same time, opioids also carry various side effects, among which respiratory depression is the direct cause of death by opioid overdose. In the United States, more than 70,000 people died in 2017 by opioid-induced respiratory depression (OIRD) (Hedegaard et al., 2020), and the death rate has been on an exponential rise due to increased misuse and addiction of prescription opioid drugs and illicit opioids.

Opioid receptors (namely, δ-, κ-, and μ-opioid receptor) inhibit cellular activity via $G_{i/o}$-mediated GPCR signaling pathway. The μ-opioid receptor (MOR) is the primary opioid receptor that mediates the clinical effects of opioids, such as analgesia (Matthes et al., 1996) and respiratory depression. In mice lacking the MOR-encoding gene *Oprm1*, systemic injection of morphine fails to induce respiratory depression (Dahan et al., 2001).

MOR is widely expressed throughout the respiratory control network. Therefore, it is likely that multiple brain structures act in synchrony to account for OIRD. Recently, there has been an intense race to identify the candidate brain structures for OIRD pathogenesis. One of them is the preBötC, which is at the core of breathing rhythm generation. A recent study reported the existence of 70–140 MOR-expressing neurons in the preBötC of mice, and the deletion of MOR from those neurons significantly abolished the respiratory depression to systemic morphine and fentanyl injection (Bachmutsky et al., 2020). Another candidate structure is the KF in the PRG, where 60% of neurons are opioid-sensitive (Levitt et al., 2015). Using the same genetic approach, Varga et al. deleted the MORs specifically from the KF neurons in mice and reported attenuated respiratory rate depression of morphine across a wide range of doses. However, when they deleted the MOR from preBötC neurons, respiratory depression was only attenuated at the low dose (Varga et al., 2019). Furthermore, blocking MOR signaling in the KF by microinjecting a MOR-specific antagonist, CTAP, partially recovered the breathing rate in the arterially perfused rats after fentanyl injection (Saunders and Levitt, 2020). More interestingly, a recent study combing optogenetic manipulation and in silico modeling found that opioids action in the preBötC is a combination of inhibiting MORs in the pre-synaptic terminals (likely from the PB and KF) and post-synaptic cell bodies (Baertsch et al., 2021), further supporting the synergistic view.

1.3.2 Serotonin

There is considerable evidence demonstrating the role of serotonin in respiratory regulation. The caudal raphe serotonergic neurons project extensively to the PRG and VRG, including the PB, KF, nucleus ambiguous (NA), retrotrapezoid nucleus (RTN), Bötzinger complex (BötC), and preBötC. Various subtypes of the serotonin receptors have also been found throughout the respiratory network (Niebert et al., 2011). For example, medullary 5-HT1A, spinal 5-HT2A, and spinal 5-HT1B modulate both the frequency and amplitude of the phrenic motoneuron discharge in neonatal rats and mice (Bou-Flores et al., 2000).

An alteration of the 5-HT system is linked to severe breathing disorders, such as sudden infant death syndrome (SIDS) at the early post-natal period and sleep apnea which is more prevalent in the aging population. In SIDS victims, there is a reduced expression of 5-HT1A and 5-HT2A, as well as reduced brain 5-HT levels and binding (Paterson et al., 2009). Mice lacking 5-HT2A displayed an increased incidence of sleep apnea (Popa et al., 2005). However, the detailed neurobiological mechanisms regarding the function of individual subtypes in the breathing network remain elusive.

The serotonin system has also been proposed as a therapeutic target to combat the opioid crisis, yet the result remains inconclusive. 5-HT4A has been found in preBötC neurons, and its specific agonist was able to revert OIRD without loss of analgesia in mice (Manzke et al., 2003). However, preliminary tests in humans failed to reproduce the beneficial effect (Lötsch et al., 2005).

Chapter 3 of this dissertation will report our discovery of another important mediator of OIRD, the parabrachial MOR neurons. Multiple neuromodulator systems, including the serotonin system, converge onto these neurons. I will also discuss our proof of principle of leveraging the artificial and endogenous GPCR systems to rescue OIRD in mice.

1.4 References

Alheid, G.F., Milsom, W.K., and McCrimmon, D.R. (2004). Pontine influences on breathing: an overview. Respir. Physiol. Neurobiol. *143*, 105-114.

Arch, J.J., and Craske, M.G. (2006). Mechanisms of mindfulness: emotion regulation following a focused breathing induction. Behav. Res. Ther. *44*, 1849-1858.

Ashhad, S., and Feldman, J.L. (2020). Emergent elements of inspiratory rhythmogenesis: network synchronization and synchrony propagation. Neuron *106*, 482-497.

Bachmutsky, I., Wei, X.P., Kish, E., and Yackle, K. (2020). Opioids depress breathing through two small brainstem sites. eLife *9*, e52694.

Baertsch, N.A., Bush, N.E., Burgraff, N.J., and Ramirez, J.-M. (2021). Dual mechanisms of opioid-induced respiratory depression in the inspiratory rhythm-generating network. eLife *10*, e67523.

Bass, C., and Gardner, W. (1985). Emotional influences on breathing and breathlessness. J. Psychosom. Res. *29*, 599-609.

Boiten, F.A., Frijda, N.H., and Wientjes, C.J.E. (1994). Emotions and respiratory patterns: review and critical analysis. Int. J. Psychophysiol. *17*, 103-128.

Bou-Flores, C., Lajard, A.-M., Monteau, R., De Maeyer, E., Seif, I., Lanoir, J., and Hilaire, G. (2000). Abnormal phrenic motoneuron activity and morphology in neonatal monoamine oxidase A-deficient transgenic mice: possible role of a serotonin excess. J. Neurosci. *20*, 4646-4656.

Chamberlin, N.L., and Saper, C.B. (1994). Topographic organization of respiratory responses to glutamate microstimulation of the parabrachial nucleus in the rat. J. Neurosci. *14*, 6500-6510.

Cui, Y., Kam, K., Sherman, D., Janczewski, W.A., Zheng, Y., and Feldman, J.L. (2016). Defining preBötzinger complex rhythm- and pattern-generating neural microcircuits in vivo. Neuron *91*, 602-614.

Cury, K.M., and Uchida, N. (2010). Robust odor coding via inhalation-coupled transient activity in the mammalian olfactory bulb. Neuron *68*, 570-585.

Dahan, A., Sarton, E., Teppema, L., Olievier, C., Nieuwenhuijs, D., Matthes, H.W., and Kieffer, B.L. (2001). Anesthetic potency and influence of morphine and sevoflurane on respiration in mu-opioid receptor knockout mice. Anesthesiology *94*, 824-832.

Del Negro, C.A., Funk, G.D., and Feldman, J.L. (2018). Breathing matters. Nat. Rev. Neurosci. *19*, 351-367.

Dick, T.E., Dutschmann, M., Feldman, J.L., Fong, A.Y., Hulsmann, S., Morris, K.M., Ramirez, J.M., Smith, J.C., and Respiratory Neurobiology, C. (2018). Facts and challenges in respiratory neurobiology. Respir. Physiol. Neurobiol. *258*, 104-107.

Dutschmann, M., and Dick, T.E. (2012). Pontine mechanisms of respiratory control. Compr. Physiol. *2*, 2443-2469.

Dutschmann, M., and Herbert, H. (2006). The Kölliker-Fuse nucleus gates the postinspiratory phase of the respiratory cycle to control inspiratory off-switch and upper airway resistance in rat. Eur. J. Neurosci. *24*, 1071-1084.

Ellenberger, H.H., and Smith, F.M. (1999). Sulfated cholecystokinin octapeptide in the rat: pontomedullary distribution and modulation of the respiratory pattern. Can. J. Physiol. Pharmacol. *77*, 490-504.

Farley, G.R., Barlow, S.M., and Netsell, R. (1992). Factors influencing neural activity in parabrachial regions during cat vocalizations. Exp. Brain Res. *89*, 341-351.

Feleky, A. (1916). The influence of the emotions on respiration. J. Exp. Psychol. *1*, 218-241.

Fulwiler, C.E., and Saper, C.B. (1984). Subnuclear organization of the efferent connections of the parabrachial nucleus in the rat. Brain Res. Rev. *7*, 229-259.

Garland, E.L., Baker, A.K., Larsen, P., Riquino, M.R., Priddy, S.E., Thomas, E., Hanley, A.W., Galbraith, P., Wanner, N., and Nakamura, Y. (2017). Randomized controlled trial of brief mindfulness training and hypnotic suggestion for acute pain relief in the hospital setting. J. Gen. Intern. Med. *32*, 1106-1113.

Garland, E.L., Brintz, C.E., Hanley, A.W., Roseen, E.J., Atchley, R.M., Gaylord, S.A., Faurot, K.R., Yaffe, J., Fiander, M., and Keefe, F.J. (2020). Mind-body therapies for opioid-treated pain: A systematic review and meta-analysis. JAMA Intern. Med. *180*, 91-105.

Han, J.N., Stegen, K., De Valck, C., Clément, J., and Van De Woestijne, K.P. (1996). Influence of breathing therapy on complaints, anxiety and breathing pattern in patients with hyperventilation syndrome and anxiety disorders. J. Psychosom. Res. *41*, 481-493.

Hedegaard, H., Miniño, A.M., and Warner, M. (2020). Drug overdose deaths in the United States, 1999-2018. NCHS data brief *356*.

Hedner, J., Hedner, T., Wessberg, P., and Jonason, J. (1984). Interaction of substance P with the respiratory control system in the rat. J. Pharmacol. Exp. Ther. *228*, 196-201.

Herbert, H., Moga, M.M., and Saper, C.B. (1990). Connections of the parabrachial nucleus with the nucleus of the solitary tract and the medullary reticular formation in the rat. J. Comp. Neurol. *293*, 540-580.

Hodges, M.R., Tattersall, G.J., Harris, M.B., McEvoy, S.D., Richerson, D.N., Deneris, E.S., Johnson, R.L., Chen, Z.F., and Richerson, G.B. (2008). Defects in breathing and thermoregulation in mice with near-complete absence of central serotonin neurons. J. Neurosci. *28*, 2495-2505.

Jafari, H., Courtois, I., Van den Bergh, O., Vlaeyen, J.W.S., and Van Diest, I. (2017). Pain and respiration: a systematic review. Pain *158*, 995-1006.

Janak, P.H., and Tye, K.M. (2015). From circuits to behaviour in the amygdala. Nature *517*, 284-292.

Jiang, M., Alheid, G.F., Calandriello, T., and McCrimmon, D.R. (2004). Parabrachial-lateral pontine neurons link nociception and breathing. Respir. Physiol. Neurobiol. *143*, 215-233.

Jürgens, U. (1976). Projections from the cortical larynx area in the squirrel monkey. Exp. Brain Res. *25*, 401-411.

Kleinfeld, D., Deschenes, M., Wang, F., and Moore, J.D. (2014). More than a rhythm of life: breathing as a binder of orofacial sensation. Nat. Neurosci. *17*, 647-651.

Levitt, E.S., Abdala, A.P., Paton, J.F., Bissonnette, J.M., and Williams, J.T. (2015). Mu opioid receptor activation hyperpolarizes respiratory-controlling Kölliker-Fuse neurons and suppresses post-inspiratory drive. J. Physiol. *593*, 4453-4469.

Li, P., Janczewski, W.A., Yackle, K., Kam, K., Pagliardini, S., Krasnow, M.A., and Feldman, J.L. (2016). The peptidergic control circuit for sighing. Nature *530*, 293-297.

Lötsch, J., Skarke, C., Schneider, A., Hummel, T., and Geisslinger, G. (2005). The 5-hydroxytryptamine 4 receptor agonist mosapride does not antagonize morphine-induced respiratory depression. Clin. Pharmacol. Ther. *78*, 278-287.

Manzke, T., Guenther, U., Ponimaskin, E.G., Haller, M., Dutschmann, M., Schwarzacher, S., and Richter, D.W. (2003). 5-HT4 (a) receptors avert opioid-induced breathing depression without loss of analgesia. Science *301*, 226-229.

Matthes, H.W., Maldonado, R., Simonin, F., Valverde, O., Slowe, S., Kitchen, I., Befort, K., Dierich, A., Le Meur, M., Dolle, P., Tzavara, E., Hanoune, J., Roques, B.P., and Kieffer, B.L. (1996). Loss of morphine-induced analgesia, reward effect and withdrawal symptoms in mice lacking the mu-opioid-receptor gene. Nature *383*, 819-823.

Miura, K., Mainen, Z.F., and Uchida, N. (2012). Odor representations in olfactory cortex: distributed rate coding and decorrelated population activity. Neuron *74*, 1087-1098.

Moberly, A.H., Schreck, M., Bhattarai, J.P., Zweifel, L.S., Luo, W., and Ma, M. (2018). Olfactory inputs modulate respiration-related rhythmic activity in the prefrontal cortex and freezing behavior. Nat. Commun. *9*, 1528.

Moore, J.D., Deschenes, M., Furuta, T., Huber, D., Smear, M.C., Demers, M., and Kleinfeld, D. (2013). Hierarchy of orofacial rhythms revealed through whisking and breathing. Nature *497*, 205-210.

Niebert, M., Vogelgesang, S., Koch, U.R., Bischoff, A.M., Kron, M., Bock, N., and Manzke, T. (2011). Expression and function of serotonin 2A and 2B receptors in the mammalian respiratory network. PLoS One *6*, e21395.

Paterson, D.S., Hilaire, G., and Weese-Mayer, D.E. (2009). Medullary serotonin defects and respiratory dysfunction in sudden infant death syndrome. Respir. Physiol. Neurobiol. *168*, 133-143.

Peirs, C., and Seal, R.P. (2016). Neural circuits for pain: recent advances and current views. Science *354*, 578-584.

Popa, D., Léna, C., Fabre, V., Prenat, C., Gingrich, J., Escourrou, P., Hamon, M., and Adrien, J. (2005). Contribution of 5-HT2 receptor subtypes to sleep–wakefulness and respiratory control, and functional adaptations in knock-out mice lacking 5-HT2A receptors. J. Neurosci. *25*, 11231-11238.

Saper, C.B. (1982). Reciprocal parabrachial-cortical connections in the rat. Brain Res. *242*, 33-40.

Saunders, S.E., and Levitt, E.S. (2020). Kölliker-Fuse/Parabrachial complex mu opioid receptors contribute to fentanyl-induced apnea and respiratory rate depression. Respir. Physiol. Neurobiol. *275*, 103388.

Shusterman, R., Smear, M.C., Koulakov, A.A., and Rinberg, D. (2011). Precise olfactory responses tile the sniff cycle. Nat. Neurosci. *14*, 1039.

Smear, M., Shusterman, R., O'Connor, R., Bozza, T., and Rinberg, D. (2011). Perception of sniff phase in mouse olfaction. Nature *479*, 397-400.

Smotherman, M., Kobayasi, K., Ma, J., Zhang, S., and Metzner, W. (2006). A mechanism for vocal-respiratory coupling in the mammalian parabrachial nucleus. J. Neurosci. *26*, 4860-4869.

Smotherman, M., Schwartz, C., and Metzner, W. (2010). Vocal–respiratory interactions in the parabrachial nucleus. Handbook of Behavioral Neuroscience *19*, 383-392.

Tan, W., Pagliardini, S., Yang, P., Janczewski, W.A., and Feldman, J.L. (2010). Projections of preBötzinger complex neurons in adult rats. J. Comp. Neurol. *518*, 1862-1878.

Uchida, N., and Mainen, Z.F. (2003). Speed and accuracy of olfactory discrimination in the rat. Nat. Neurosci. *6*, 1224-1229.

Varga, A.G., Maletz, S.N., Bateman, J.T., Reid, B.T., and Levitt, E.S. (2021). Neurochemistry of the Kölliker-Fuse nucleus from a respiratory perspective. J. Neurochem. *156*, 16-37.

Varga, A.G., Reid, B.T., Kieffer, B.L., and Levitt, E.S. (2020). Differential impact of two critical respiratory centres in opioid-induced respiratory depression in awake mice. J. Physiol. *598*, 189-205.

Wallois, F., Macron, J.M., Jounieaux, V., and Duron, B. (1991). Trigeminal nasal receptors related to respiration and to various stimuli in cats. Respir. Physiol. *85*, 111-125.

Wang, S.C., Ngai, S.H., and Frumin, M.J. (1957). Organization of central respiratory mechanisms in the brain stem of the cat: genesis of normal respiratory rhythmicity. Am. J. Physiol. *190*, 333-342.

Welker, W. (1964). Analysis of sniffing of the albino rat 1. Behaviour *22*, 223-244.

Williams, R.H., and Burdakov, D. (2008). Hypothalamic orexins/hypocretins as regulators of breathing. Expert Rev. Mol. Med. *10*, e28.

Yackle, K., Schwarz, L.A., Kam, K., Sorokin, J.M., Huguenard, J.R., Feldman, J.L., Luo, L., and Krasnow, M.A. (2017). Breathing control center neurons that promote arousal in mice. Science *355*, 1411-1415.

Chapter 2: Divergent brainstem opioidergic pathways that coordinate breathing with pain and emotions

2.1 Abstract

Breathing can be heavily influenced by pain or internal emotional states, but the neural circuitry underlying this tight coordination is unknown. Here we report that *Oprm1* (μ-opioid receptor)-expressing neurons in the lateral parabrachial nucleus (PBL) are crucial for coordinating breathing with affective pain in mice. Individual PBL^{Oprm1} neuronal activity synchronizes with breathing rhythm and responds to noxious stimuli. Manipulating PBL^{Oprm1} activity directly changes breathing rate, affective pain perception, and anxiety. Furthermore, PBL^{Oprm1} neurons constitute two distinct subpopulations in a “core-shell” configuration that divergently projects to the forebrain and hindbrain. Through non-overlapping projections to the central amygdala and pre-Bötzinger complex, these two subpopulations differentially regulate breathing, affective pain, and negative emotions. Moreover, these subsets form recurrent excitatory networks through reciprocal glutamatergic projections. Together, our data define the divergent parabrachial opioidergic circuits as a common neural substrate that coordinates breathing with various sensations and behaviors such as pain and emotional processing.

2.2 Introduction

Breathing is a fundamental, life-sustaining function (Dick et al., 2018). This rhythmic behavior originates from the network activity of the ventrolateral medulla (Ashhad and Feldman, 2020) and contributes to a variety of homeostatic processes, particularly the maintenance of pH and blood O2/CO2 levels (Del Negro et al., 2018). To date, most breathing research has focused on the mechanism by which pacemaking networks in medullary respiratory centers generate breathing rhythm (Dick et al., 2018). However, little is known about neural mechanisms regulating changes in breathing rhythm by such factors as emotional and sensory stimuli (Boiten et al., 1994). For example, in humans, intense and

uncontrollable pain induces hyperventilation (Jafari et al., 2017). Breathing also becomes faster and more shallow with fear (Feleky, 1916) and in psychiatric conditions such as panic attacks, posttraumatic stress disorder, and phobias (Bass and Gardner, 1985). Breathing rhythm can also be controlled by volitional processes, such as sniffing (Moore et al., 2013), vocalizing (Smotherman et al., 2010), swallowing (Bautista et al., 2014), and sighing (Li et al., 2016).

The breathing center most likely to mediate the breathing changes by emotional and sensory inputs is the pontine respiratory group (PRG) (Del Negro et al., 2018). Unlike the medullary respiratory groups (Cui et al., 2016; Del Negro et al., 2018; Tan et al., 2010), the PRG is not involved in the direct generation of respiratory rhythms, but instead modulates the rate and pattern of breathing (Del Negro et al., 2018; Wang et al., 1957) in response to various forebrain and hindbrain inputs (Dutschmann and Dick, 2012). One crucial component of the PRG is the parabrachial nucleus (PB), a small but heterogeneous nucleus composed of various cytoarchitecturally distinct subnuclei (Fulwiler and Saper, 1984). Direct electrical stimulation of this area, or glutamate injection altered breathing rhythm in cats (Cohen, 1971) and rats (Chamberlin and Saper, 1994), respectively. Interestingly, alternately facilitatory and inhibitory effects have been reported on this behavior depending on stimulation protocol and location (Chamberlin and Saper, 1994; Cohen, 1971; Dutschmann and Dick, 2012; Navarrete-Opazo et al., 2020). For example, activating the dorsal PB induced tachypnea, whereas the ventral PB—especially the Kölliker-Fuse nucleus—induced variable responses such as apneusis, bradypnea, and tachypnea (Chamberlin, 2004; Chamberlin and Saper, 1994; Dutschmann and Dick, 2012; Dutschmann and Herbert, 2006).

Among the subdivisions of the PB, the lateral PB (PBL, or referred to as PBL, lPB, PBNl, or lPBN in other papers) is known to relay affective pain signals from the spinal cord to the forebrain (Gauriau and Bernard, 2002; Han et al., 2015). The PBL neurons are mostly

glutamatergic (Yokota et al., 2015) and express several specific molecular markers such as Oprm1, which encodes the μ-opioid receptor (MOR) (Chamberlin et al., 1999). The MOR is the primary inhibitory opioid receptor mediating opioid-induced analgesia, as Oprm1-knockout mice lacked antinociceptive responses to morphine administration (Matthes et al., 1996). The MOR is also highly expressed among the respiratory centers of the brain and is regarded as a primary contributor to opioid-induced respiratory depression (OIRD) (Dahan et al., 2001; Montandon et al., 2011; Prkic et al., 2012). Indeed, conditional deletion of the Oprm1 gene in the parabrachial complex ameliorates OIRD (Bachmutsky et al., 2020; Liu et al., 2021; Varga et al., 2020). Together, these findings suggest possible roles of the parabrachial MOR signaling pathway in both pain perception and breathing regulation.

Based on the above observations, we hypothesized that *Oprm1*-expressing neurons in the PBL (PBL^{Oprm1}) coordinate breathing with pain and emotions, as in pain-induced hyperventilation. Using cell type-, and projection-specific circuit dissection approaches that allow us to map, monitor, and manipulate defined neural circuits, we found that PBL^{Oprm1} neurons regulate breathing rate, affective pain, and anxiety-like behaviors. Furthermore, our results demonstrate that these behaviors are collectively controlled by the recurrent excitatory neural network of two distinct subpopulations of *Oprm1* neurons in the core and shell of the PBL, which diverge to the central amygdala (CeA, the emotion center) and the pre-Bötzinger complex (preBötC, the ventral respiratory center).

2.3 Material and Methods

Mouse lines

All protocols for animal experiments were approved by the IACUC of the Salk Institute for Biological Studies according to NIH guidelines for animal experimentation. The *Oprm1-Cre:GFP* transgenic mouse line used in this study was generated by the lab of Dr. Richard Palmiter (Palmiter, 2018), and heterozygous animals were used unless otherwise noted. The wild type mice were purchased from the Jackson Laboratory (Stock No. 000664). Both male and female mice were used in all studies. Animals were randomized to experimental groups, and no sex differences were noted. Mice were maintained on a 12 h light/dark cycle and provided with food and water *ad libitum*.

Respiratory measurements

Inductance plethysmography

Inductance plethysmography was performed by placing a piezoelectric film beneath the chest of an anesthetized animal, which converted chest movements into voltage signals. Isoflurane was selected for anesthesia for its dose adjustment flexibility and instant feedback. Test mice were kept under light anesthesia until a stable breathing rate of 100–130 bpm—much lower than awake animals—was reached. Breathing rhythm was monitored with inductance plethysmography by placing a piezoelectric sensor beneath the chest of the test mouse to detect the chest expansion that accompanied each breathing cycle. The PowerLab system with LabChart 8 software (ADInstruments) was used for data acquisition, inspiratory and expiratory peak detection, and rate and amplitude calculation. Breathing rate was calculated by counting the number of peaks per minute. Breathing amplitude was estimated by the plethysmograph amplitude, i.e., the height of the plethysmograph waveform. Data

were sampled at 100–400 Hz, low-pass filtered at 10 Hz, and smoothed with a 100-ms moving window. Automatic peak detection was validated with manual peak detection.

Whole body plethysmography (WBP)

A custom-built WBP chamber was utilized to measure breathing parameters. The PowerLab system with LabChart 8 software was used for data acquisition, inspiratory and expiratory peak detection, and rate and amplitude calculation. Breathing rate was calculated by counting the number of peaks. Breathing amplitude was estimated by the plethysmograph amplitude, i.e., the height of the plethysmograph waveform. Data were sampled at 1 kHz, band-pass filtered at 1–10 Hz, and smoothed with a 100-ms moving window. Automatic peak detection was validated with manual peak detection.

Mice were placed into the WBP chamber for three 20-min habituation sessions before testing. To test whether thermistor sensor implant alters normal breathing patterns, implanted and naïve mice were kept in the WBP chamber for 10–12 min. For chemogenetics experiments, mice were kept in the chamber for 10–12 min during the testing session before and after drug injection. After 5–10 min of chamber habituation, a stable pattern was reached and the averaged value of a stabilized 1-min segment was analyzed.

Micro thermistor-based plethysmography

A custom-built micro thermistor was implanted into the mouse nasal cavity to detect changes in temperature between inspiratory and expiratory airflow (McAfee et al., 2016). In contrast to traditional breathing measurements like whole-body plethysmography (WBP) (Mortola and Frappell, 1998) and tracheostomy airflow sensor measurements, this approach allows us to monitor breathing in awake, unrestrained, behaving mice with unprecedented freedom to access the brain. The sensor was assembled using a Negative Temperature

Coefficient (NTC) thermistor (TE Connectivity), an interconnector (Mill-Max), and a voltage divider (Phidgets). PowerLab (ADInstruments) was used for data acquisition, inspiratory and expiratory peak detection, and rate and amplitude calculation. Voltage increases and decreases indicated expiration and inspiration, respectively. Breathing rate was calculated by counting the number of peaks per minute. Breathing amplitude was estimated by the plethysmograph amplitude, i.e., the height of the plethysmograph waveform. Data were sampled at 1 kHz, filtered with a 0.4–25 Hz band-pass filter, and smoothed with a 50-ms moving window. Automatic peak detection was validated with manual peak detection. For the alignment of calcium activity with the onset of major respiratory events, we defined the “high respiratory activity bout” as a continuous period of high activity distinct from the stable baseline that lasts over 120 seconds.

Stereotaxic surgery

Mice were anesthetized with isoflurane (5% induction, 1.5–2% maintenance with a nose cone; Dräger Vapor 2000, Draegar) and maintained on a water recirculating heating pad throughout the surgery. Mice were placed on a stereotaxic frame (David Kopf Instruments), the skull was exposed, and the cranium was drilled with a micro motor handpiece drill (Foredom); one or two holes were drilled for viral injection, two holes for screws with implantation, one or two holes for optic fibers, and one hole for a micro thermistor. The virus was injected unilaterally or bilaterally into the PBL [anteroposterior (AP), -1 to -1.15 mm from lambda; mediolateral (ML), ±1.5 mm; dorsoventral (DV), -3.5 mm, re-zero at the midline with the same AP], unilaterally to the preBötC (AP, -2.4 to -2.6 mm from lambda; ML, 1.3 mm; DV, -5.7 mm from contralateral skull surface), unilaterally or bilaterally to the CeA (AP, -1.1 mm; ML, ±2.9 mm; DV, -5.2 mm, re-zero at the midline with the same AP), and unilaterally to the dorsal striatum (AP, +0.5 mm; ML, -1.8 mm; DV, -2.2 mm from

brain surface). Viral injection was performed with glass pipettes with tips broken for an inner diameter of 20 μm, which were connected to the Nanoject III Programmable Nanoliter Injector (Drummond Scientific) set to an infusion rate of 60 nL/min. Glass pipettes were retracted from the brain 5–10 min after injection. Optic fibers were implanted above the injection site with the DV noted above. The micro thermistor head was carefully lowered into the hole above the nasal cavity (AP, +3.5 mm from the nasal fissure; ML, 0.3 mm). Implants were covered with superglue and dental cement for stabilization. Unless otherwise noted, behavioral experiments were performed three weeks after viral injection and one week after the micro thermistor implantation, and all viruses were obtained from the Salk Institute Viral Vector core.

For fiber photometry, *Oprm1*$^{Cre/+}$ mice were unilaterally injected with 200 nL of either AAV1-syn-FLEX-jGCaMP7s-WPRE (1.5E+13 GC/mL) or control AAV2-EF1a-DIO-eYFP (2.12E+12 GC/mL) virus into the PBL. For the movement-breathing dissociation experiment, we injected 200 nL of AAV1-Syn-GCaMP6f-WPRE-SV40 (2.30E+12 GC/mL) into the dorsal striatum. For investigation of the involvement of PBL *Oprm1*-negative neurons in breathing, we injected 200 nL of AAV8-hSyn-DO-GCaMP6m (UNC viral vector core) into the PBL of the *Oprm1*$^{Cre/+}$ mice. A custom-made stainless-steel mono fiber-optic cannula (400 μm diameter, 0.37 NA) was implanted 0.05 mm above the injection site.

For single-cell calcium imaging with microendoscope, *Oprm1*$^{Cre/+}$ mice were unilaterally injected with 500 nL of AAVDJ-syn-FLEX-jGCaMP8m-WPRE (5E+12 GC/mL) virus into the PBL. An integrated microendoscope lens (0.6 mm x 7.3 mm, Inscopix) was implanted using the following coordinates: AP, -4.95 mm; ML, 1.5 mm; DV, -3.6 mm, re-zero at Bregma.

For chemogenetics, 200 nL of either AAVDJ-EF1a-DIO-hM3D(Gq)-mCherry (6.56E+11 GC/mL), AAVDJ-EF1a-DIO-hM4D(Gi)-mCherry (6.04E+11 GC/mL), or control AAV2-EF1a-DIO-eYFP (2.12E+12 GC/mL) was injected bilaterally into the PBL of *Oprm1*$^{Cre/+}$ mice.

For optogenetics, mice were bilaterally injected with 200 nL of AAVDJ-EF1a-DIO-hChR2(H134R)-EYFP-WPRE-pA (1.8E+13 GC/mL) for photostimulation, 300 nL of AAVDJ-FLEX-ArchT-GFP (1.26E+12 GC/mL) for photoinhibition, or a corresponding amount of control AAV2-EF1a-DIO-eYFP (2.12E+12 GC/mL) into the PBL of *Oprm1*$^{Cre/+}$ mice. A custom-made ceramic mono fiber-optic cannula (200 µm diameter, 0.22 NA) was implanted 0.3 mm above the injection site.

For monosynaptic rabies tracing of PBL^{Oprm1} neurons, 200 nL of AAV8-hSyn-FLEX-TVA-P2A-GFP-2A-oG (3.64E+13 GC/mL) was injected unilaterally into the PBL of the *Oprm*$^{Cre/+}$ mice or control wild type mice. After three weeks, 200 nL of EnvA-ΔG-rabies-mCherry (3.95E+08 GC/mL) was unilaterally injected into the PBL. Mice were sacrificed seven days following injection.

For investigation of PBL^{Oprm1} projections to the ventrolateral medulla, *Oprm*$^{Cre/+}$ mice were bilaterally injected with 200 nL of AAV2-phSyn1(S)-FLEX-tdTomato-T2A-SypEGFP-WPRE (2.23E+11 GC/mL) into the PBL. Euthanasia and histology were performed three weeks following injection.

For intersectional anatomical tracing and projection-specific electrophysiology, *Oprm*$^{Cre/+}$ mice were bilaterally injected with 200 nL of AAVrg-EF1a-DIO-FLPo-WPRE-hGHpA (1.98E+13 GC/mL) unilaterally into the preBötC, 200 nL of AAVrg-EF1a-DIO-mCherry (1.51E+13 GC/mL) unilaterally into the CeA, and 200 nL of AAV9-EF1a-fDIO-hChR2(H134R)-EYFP (5.21E+12 GC/mL) unilaterally into the PBL.

For projection-specific fiber photometry calcium activity recording, *Oprm*$^{Cre/+}$ mice were bilaterally injected with 200 nL of AAVrg-EF1a-DIO-FLPo-WPRE-hGHpA (1.98E+13 GC/mL) unilaterally into the preBötC or into the CeA, and 200 nL of AAV8-Ef1a-fDIO-GCaMP6s (1.0E+13 GC/mL) unilaterally into the PBL. A custom-made zirconia mono fiber-optic cannula (400 μm diameter, 0.37 NA) was implanted 0.05 mm above the injection site and a breathing sensor was implanted into the nasal cavity.

For projection-specific optogenetics, *Oprm*$^{Cre/+}$ mice were injected with 200 nL of AAVrg-EF1a-DIO-FLPo-WPRE-hGHpA (1.98E+13 GC/mL) unilaterally into the preBötC or bilaterally into the CeA, and 200 nL of AAV9-EF1a-fDIO-hChR2(H134R)-EYFP (5.21E+12 GC/mL) or control AAV8-EF1a-fDIO-EYFP (4.39E+12 GC/mL) bilaterally into the PBL. Unilateral injection was made into the preBötC to minimize damage to the medulla. A custom-made ceramic mono fiber-optic cannula (200 μm diameter, 0.22 NA) was implanted 0.5 mm above the injection site.

For projection-specific chemogenetics, *Oprm*$^{Cre/+}$ mice were injected with 200 nL of AAVrg-EF1a-DIO-FLPo-WPRE-hGHpA (1.98E+13 GC/mL) unilaterally into the preBötC or bilaterally into the CeA, and 250 nL of AAVDJ-hSyn-fDIO-hM4D(Gi)-mCherry-WPREpA (1E+13 GC/mL) or control AAV8-EF1a-fDIO-EYFP (4.39E+12 GC/mL) bilaterally into the PBL.

Fiber photometry

A fiber photometry system (405 and 465 nm Fiber Photometry System, Doric for Fig. 1 and S1G; pyPhotometry for other figures) was used to record PBL^{Oprm1} activity. For the Doric system, GCaMP isosbestic fluorescence (405 nm excitation) and calcium-dependent fluorescence (465-nm excitation) were recorded at a sampling rate of 12 kHz, and data were analyzed with the Doric Neuroscience Studio software. For the pyPhotometry system, both

channels were recorded with the 1-color time-division setting at 100 Hz with its provided Python script, and data were analyzed with custom MATLAB scripts. F0 was calculated by a least mean squares fitting of the 405-nm channel in reference to the 465-nm channel, and ΔF/F was calculated as: $(F_{465}-F_{405\_fitted})/F_{405\_fitted}$.

Cross-correlation analysis between calcium signals and respiration data was performed using the z-scored data and the MATLAB “xcorr” function with the normalized option, which allows autocorrelations at zero lag to equal 1. The area under the curve (AUC) was calculated with the MATLAB “trapz” function with the z-scored data.

In awake behaving animals, concurrent measurements of PBL^{Oprm1} activity and respiration were recorded in the animal’s home cage for 20 min. For sighing analysis, sighing events were identified based on the stereotypical voltage pattern from the breathing recording. For sniffing analysis, rearing-sniffing events were identified based on the video recording. For pinching test, fine forceps were used to deliver a transient tail pinch to the test animal in its home cage 5-6 times with at least 1-min inter-trial interval. Behavioral video recording and synchronization were performed with Raspberry Pi camera (Raspberry Pi Foundation). For hot plate test, animals were placed on a 55°C hot plate custom-built with a TC-720 thermoelectric temperature controller (TE Technology) for four min.

In anesthetized animals, we recorded PBL^{Oprm1} activity and respiration simultaneously during the delivery of mechanical and thermal pain. For mechanical stimuli, 0 g and 300 g of mechanical pressure were delivered to the tail tip using a dial tension gauge (ATG-300-1, Vetus Instruments). For thermal stimuli, 25°C and 55°C heat were administered to the tail tip using a rod connected to a temperature controller (TA4-SNR+K, Mypin). Painful stimuli were delivered for 5 s after a stable 10-s baseline. AUC was calculated for 0–2.5 s before, 2.5–5 s

after the mechanical or thermal stimulation, and during the 2-min segment before and after the start of temperature change during the hot plate assay.

Single-cell calcium imaging

Calcium activities were recorded at 10 Hz and 0.4–1 mW/mm^2 LED power using an Inscopix nVista miniature microscope. Animals were attached to both the breathing sensor and the miniscope, and allowed to habituate in the home cage three times before the actual recording. During the recording, animals freely explored the home cage for 20 minutes while their breathing pattern, calcium activity, and behavior were being recorded. On subsequent imaging sessions, the breathing sensor was removed to reduce the weight of the head attachments, and fine forceps were used to briefly pinch animals' tails 5–6 times. A Raspberry Pi camera was used to record behavior videos and trigger calcium and breathing recordings. Pinching onsets were manually identified from the behavioral video. Inscopix data processing software was used for data post-processing with 2x spatial downsampling, fixing the defective pixels, spatial band-pass filtering, and motion correction using the first frame as the global reference frame. Single cells were identified by the CNMFe algorithm and then validated manually. The output unit was dF over noise and z-scored throughout the whole trace.

For heatmap, we plotted representative breathing trace and averaged pinching trace for each individual cell from one example animal. Cells were sorted by the average value in the breathing trials, and the pinching trials were plotted in the same order. To classify cells that responded to breathing, we generated a series of pairwise CCM models in which the inputs were each neuron's activity and the animal's breathing rate, and the outputs were the predictability scores of each pair. The neurons whose activities displayed a predictive relationship with breathing were classified as "breathing-responsive cells". To identify cells

that responded to pinching, we calculated the maximum or minimum values during 0–4 seconds before and 0–10 seconds after pinching for each episode and compared “pre” and “post” groups with paired t-tests. Neurons that showed significant differences in the statistical tests were classified as pain responsive.

Convergent cross-mapping

State-space reconstruction models were generated using the convergent cross mapping framework (Sugihara et al., 2012), a nonlinear time series embedding method (Sugihara and May, 1990) based on the Takens theorem and its generalized form (Deyle and Sugihara, 2011), which builds low-dimensional manifolds from time series and makes predictions across variables. Analysis and predictions were calculated using the R package rEDM 0.7.2 (https://cran.r-project.org/web/packages/rEDM/) for evaluation and the rEDM 0.7.4 (https://ha0ye.github.io/rEDM/) for model predictions in the RStudio environment. These packages were run on a dual Intel Xeon Gold 6148 Server with 384GB RAM or an Intel Core i9 2.4 GHz MacBook Pro with 32 GB RAM. Key parameters were determined individually by lagged coordinate embedding using the simplex function implementation in rEDM to optimize predictive skill as measured by the predicted over observed rho. Parameters include the delay tau, which calculates the characteristic timescale of the series, and the embedding dimensionality, which estimates the number of variables driving the system and approximates variable number as given by the Whitney embedding theorem (Whitney, 1936) as minimally equal to the real number n of variables, but no more than two times n + 1 ($n \leq E \leq 2n+1$). The choice of tau was informed by minimizing mutual information (Fraser and Swinney, 1986). This approximately corresponds to an autocorrelation of ~0.3, which was applied if data maximized predictive skill across datasets. To prevent data contamination, an exclusion radius was applied that was larger than the

respiration rate smoothing window of five timesteps. When data allowed, an exclusion radius of E*tau was applied. If not, the exclusion radius was set just larger than tau. In this paper, CCM was utilized to generate multidimensional models from embeddings of GCaMP activity which were used to predict breathing rate, or vice versa.

Chemogenetics

For behavioral testing, CNO (Cayman Chemical) was diluted in 0.9% saline to make a 1 mg/mL working solution. No precipitate was observed in the solution, indicating that the specific polymorph of the drug exhibits sufficient water solubility. CNO solution was injected intraperitoneally (i.p.) with a final concentration of 5 mg/kg (for whole population breathing measurement and all projection-specific silencing experiments) or 7.5 mg/kg (for whole population silencing experiments). Behavioral testing began 45–60 min after CNO injection. Animals that did not exhibit expression on one side were excluded.

For medullary activation of PBL^{Oprm1} projections, clozapine, a high-affinity agonist for DREADDs (Gomez et al., 2017), was used to activate the PBL^{Oprm1} axon terminals in the ventrolateral medulla (VLM) breathing center. eYFP-expressing controls ensured that CLZ selectively activated DREADD-expressing neurons. CLZ was first solubilized at pH 2.0 with HCl and then diluted. HPBCD [(2-Hydroxypropyl)-β-cyclodextrin] was added to solubilize clozapine with an HBPCD:CLZ molar ratio of 4:1. Solutions were titrated to neutral pH using NaOH and filter sterilized (0.22 μm) prior to intracranial administration (Abrams et al., 2008). CLZ (1 μg/μL) was injected bilaterally to the VLM with 100 nL/side using a glass pipette. A 50-nL aliquot of Cholera Toxin Subunit B-488 was injected using the same coordinates to mark the injection site. Data from 0–3 min before and 7–10 min after CLZ injection were used for quantification.

Ex vivo electrophysiology

Mice were anesthetized with isoflurane and the vascular system was perfused with ice-cold cutting solution (110.0 mM choline chloride, 25.0 mM $NaHCO_3$, 1.25 mM NaH_2PO_4, 2.5 mM KCl, 0.5 mM $CaCl_2$, 7.0 mM $MgCl_2$, 25.0 mM glucose, 5.0 mM ascorbic acid and 3.0 mM pyruvic acid, bubbled with 95% O_2 and 5% CO_2). Mice were decapitated, and brains were quickly removed and chilled in ice-cold cutting solution. Coronal slices containing the PBL (250 μm) were cut using a VT 1200S Vibratome (Leica) and transferred to a storage chamber containing artificial cerebrospinal fluid (aCSF; 124 mM NaCl, 2.5 mM KCl, 26.2 mM $NaHCO_3$, 1.2 mM NaH_2PO_4, 13 mM glucose, 2 mM $MgSO_4$ and 2 mM $CaCl_2$, at 32 °C, pH 7.4, bubbled with 95% O_2 and 5% CO_2). After recovery of at least 30 min, slices were transferred to room temperature (22–24 °C) for at least 60 min before use.

Slices were transferred into the recording chamber and perfused with aCSF at a flow rate of 2 mL/min. The temperature of the aCSF was controlled at 32 °C by a TC-324C Temperature controller (Warner Instruments). PBL^{Oprm1} neurons were visualized with 490 nm epifluorescence illumination with a Scientifica SliceScope Pro (Scientifica). Whole-cell and cell-attached patch-clamp electrophysiology was performed with Multiclamp 700B amplifiers (Molecular Devices). Signals were digitized at 10 kHz with Digidata 1550B (Molecular Devices).

For cell-attached patch-clamp, aCSF was the internal solution. Spontaneous firing was measured before and after a 3 μM CNO perfusion. For whole-cell patch-clamp recordings, K^+-containing internal solution was used (130 mM K-gluconate, 20 mM HEPES, 2 mM NaCl, 4 mM $MgCl_2$, 0.25 mM EGTA, 4 mM Na-ATP, 0.4 mM Na-GTP, pH 7.2). Under current-clamp conditions, a 50 pA current was injected into the cell to induce action potential firing before and after a 3 μM CNO perfusion.

For the projection-specific electrophysiology experiment, 2-ms blue light pulse was emitted from a collimated 473 nm light-emitting diode (pE-300, CoolLED) under the control of an Axon Digidata 1440A Data Acquisition System and pClamp 10 software (Molecular Devices). Light was delivered through the reflected light fluorescence illuminator port and a 40X objective. AMPA-mediated EPSCs were blocked by bath application of 10 mM CNQX (Tocris). Quantitation was performed with the Clampfit module in the pClamp 10 software.

Optogenetics

For photostimulation and photoinhibition, a 470 nm collimated diode and a 589 nm diode-pumped solid-state (DPSS) laser system (LaserGlow Tech.) were used. For breathing measurements, mice were placed under light isoflurane anesthesia and subjected to either 470 nm photostimulation at 20 Hz or continuous 589 nm photostimulation to activate or silence PBL^{Oprm1} neurons. The selection of pulsed and continuous light was determined to optimize the excitation and inhibition experiments, respectively. In general, light-driven ion pumps, such as halorhodopsin and archaerhodopsin both require continuous light to sustain the ion pumping activity (Mahn et al., 2021; Zhang et al., 2007). Particularly, ArchT has a fast photocycle and quickly recovers from the opening state in the dark (Chow et al., 2012; Chow et al., 2010). Pulsed light was used for ChR2-mediated excitation since this is sufficient for activating the neurons of interest while reducing tissue heating (Stujenske et al., 2015). The output power was 5 ± 1 mW, as measured from the tip of the optic fiber. For investigation of ChR2-induced breathing changes, 5-ms square pulses were given at 20 Hz for 10 s. The maximum breathing parameters 10 s before and 10 s after the stimulation onset were analyzed. For ArchT-induced breathing changes, a 30 s continuous-wave stimulation was delivered, and the average breathing parameters 10 s before and 10 s after the stimulation onset were analyzed.

For behavioral tests with projection-specific optogenetic activation experiments, the output power was 10 ± 2 mW, as measured from the tip of the optic fiber, and 2-ms square pulses at 40 Hz were given with different burst patterns (RTPA: 2-s on, 10-s off; formalin: 1-s on; 3-s off; EPM: 2-s on, 2-s off; other assays: continuous).

For ArchT-stimulation combined with mechanical and thermal pain stimulation, 300 g of mechanical pressure and 55°C heat were administered to the mouse tail tip using a dial tension gauge (ATG-300-1, Vetus Instruments) and a temperature controller (TA4-SNR+K, Mypin), respectively. Painful stimuli were administered for 5 s after a stable 10 s baseline, and a subsequent 5 s photoinhibition was administered for 3–5 s. For quantification purposes, three 3-s breathing episodes were analyzed: immediately before and immediately after the painful stimuli, and during the 5 s photostimulation.

For the ArchT- and ChR2- stimulation combined with the RTPP or RTPA assay, a two-chamber arena (30 x 60 x 30 cm^3) was used. A Gigabit Ethernet (GigE) USB camera (DFK 33GX236, Imagine Source; 25 frames/s, FPS), together with video-tracking software (EthoVision XT 12, Noldus Information Technology), tracked the animal and controlled the stimulation. After connecting to the patch cord, mice were placed in one side of the chamber for a 10 min baseline session and a subsequent 10 min test session, where a continuous wave of photoinhibition (ArchT) or 40 Hz photostimulation (ChR2) was administered when mice entered one side of the chamber. The stimulation side was counterbalanced among animals. A 70% ethanol solution and deionized water were used for cleaning immediately after each test. For the ArchT experiment, animals that did not show bilateral expression were excluded from the analysis.

Histology

Mice were euthanized with CO_2 at a flow rate of 1.2 liters/min (LPM), perfused intracardially with ice-cold phosphate-buffered saline (PBS), and fixed with 4% paraformaldehyde (PFA, 19210, Electron Microscopy Sciences) in phosphate buffer (PB). The brain was extracted, post-fixed in 4% PFA overnight, and dehydrated in 30% sucrose in PBS until sliced. Frozen brains were cut into 50-μm coronal slices using a CM 1950 cryostat (Leica) and stored in PBS prior to mounting. The slices were mounted on Superfrost microscope slides (Fisher Scientific) with DAPI Fluoromount-G mounting media (Southern Biotech) for imaging.

Immunohistochemistry

To investigate PBL^{Oprm1} projections onto preBötC neurons, anti-somatostatin (SST, a marker for preBötC) and anti-choline acetyltransferase (ChAT, a marker for motor neurons in the nearby nucleus ambiguous) staining was performed on medulla (AP -7.3 mm, coronal) sections. To confirm MOR expression on the jGCaMP7s-expressing cells or Rabies tracing starter cells, anti-MOR staining was performed on parabrachial sections. Mice were euthanized with CO_2 at a flow rate of 1.2 LPM, then perfused intracardially with ice-cold PBS and followed by 4% PFA in PB. The brain was extracted, post-fixed in 4% PFA overnight, and dehydrated in 30% sucrose in PBS until sliced. Frozen brains were cut into 30 μm coronal slices with a CM 1950 cryostat and stored in PBS. For anti-MOR staining, slices were treated in 1% SDS at room temperature for 5 min for antigen retrieval.

Sections were washed with 0.2% PBST and blocked with 3% NDS (or 5% NDS in 0.3% PBST for anti-MOR) for 1 h at room temperature. After rinsing with PBST, slices were incubated with rabbit anti-SST14 (1:250, Peninsula Laboratories) and goat anti-ChAT (1:100, Sigma-Aldrich), or rabbit anti-MOR (1:250, Immunostar) at 4° C for 24 h. The following day, brain tissues were rinsed with PBST and incubated in Cy3-conjugated Donkey Anti-Rabbit

IgG and Alexa Fluor 647-conjugated Donkey Anti-Goat IgG (1:500 in 3% NDS, for SST/ChAT staining) or Alexa Fluor 647-conjugated Donkey Anti-Rabbit IgG (1:300 in 5% NDS, for MOR staining) for 90 min at room temperature. After washing with PBS, the slices were mounted on Superfrost microscope slides with DAPI Fluoromount-G mounting media for imaging.

RNA in situ hybridization

RNA in situ hybridization was performed using the RNAscope Fluorescent Multiplex Assay using the probes and kits purchased from Advanced Cell Diagnostics. Brains were collected from wild type mice and immediately frozen with 2-methylbutane chilled with dry ice. Frozen brains were cut into 20-µm coronal slices with a CM 1950 cryostat and directly mounted onto the Superfrost Plus Microscope Slides (Fisher Scientific). Sample preparation, pretreatment, and signal detection were performed according to the ACD protocols.

For quantification, one representative image from the PBL were selected from n = 5-6 mice, and all fluorescent cells within a field of view of 600 µm x 600 µm were included. DAPI-stained nuclei were first identified, then the cell contour was defined with a ~2-µm radius surrounding the DAPI signals. Cells containing at least five puncta inside the imaginary boundary were labeled as positive.

Imaging

Images for histological confirmation were taken with the BZ-X710 all-in-one fluorescence microscope with the BZ-X viewer software under a 10X, 0.45 NA objective (Keyence). Images for the monosynaptic Rabies tracing were taken at the Salk Institute Waitt Advanced Biophotonics Core with the Olympus VS-120 Virtual Slide Scanning Microscope under an Olympus UPLSAPO 4X, 0.16 NA objective. Images for MOR immunohistochemistry, SypGFP terminals in the preBötC, projection mapping, and

RNAscope were taken by an FV3000 Confocal Laser Scanning Microscope with FV31S-SW software under Olympus UPLSAPO 4X, 0.16 NA; 10X, 0.40 NA; 20X, 0.75 NA; 40X, 1.30 NA, or 60X, 1.42 NA objectives (Olympus). For quantification, images were processed with the same gain, offset, and exposure time.

Monosynaptic rabies tracing

Brain slice collection and region assignments were performed according to the Allen Brain Atlas. Every 50 μm section from AP + 2.62 mm to AP -7.455 mm was collected and imaged by an Olympus VS-120 Virtual Slide Scanning Microscope using the OlyVIA software with identical magnification and exposure time. Neurons with mCherry-positive cell bodies were counted manually. Brain slices located ± 0.4 mm anterior and posterior to the starter region were excluded. The injection was unilateral (right side), and the quantification of cells was bilateral. The percentage of the total presynaptic inputs from a given brain region was calculated by dividing the number of presynaptic neurons by all neurons registered to the atlas. For quantification of starter cells with MOR immunohistochemistry, a field of view of 300 μm x 300 μm from the PBL area was used for counting.

Subpopulation-specific anatomical mapping

To reveal the expression patterns of PBL^{Oprm1} subpopulations, brain slices containing the PBL (50-μm thickness) were collected three weeks after viral injection. In the PBL, mCherry- and eYFP-labeled cells as well as their overlaps were counted, and the average cell numbers of three slices were displayed. To investigate projection patterns of PBL^{Oprm1} subpopulations, brain sections (30-μm thickness for sections containing ventrolateral medulla, 50-μm thickness otherwise) were collected three weeks after viral injection. SST immunohistochemistry was performed in medullary slices to identify the preBötC area.

Elevated-plus maze test

To measure anxiety-like behavior, a custom-built plus-shaped maze with two 77 cm long opposite closed arms, two 77 cm long opposite open arms, and a central square of 7 cm sides was situated 70 cm above the floor. EthoVision XT 12 software with a GigE USB camera at 25 FPS was used for animal tracking. The test mouse was introduced to the open arm adjacent to the center and explored the maze for 5 min. For the ChR2 experiment, mice were connected with patch cord, put back into the home cage for 10 minutes, then introduced to the arena. Time spent in open and closed arms and entries into open arms were calculated by the EthoVision XT 12 software. A 70% ethanol solution and deionized water were used for cleaning immediately after each test. For hM4Di experiments, to reduce open arm time for control animals, we used bright lighting and opaque walls of closed arm. For ChR2 experiments, to increase open arm time for control animals, we used dim lighting and transparent walls of closed arm.

Hot plate test

To measure thermal sensitivity, mice were placed inside a cylindrical, transparent Plexiglass chamber (D = 11 cm, H = 15 cm) on a hot plate (52 °C or 55 °C, PE34, IITC Life Science). For hM4Di experiments, the temperature was set to 55 °C; the latency of the painful response (hind paw shake, lick or jump) was manually recorded until the animal jumped out or until the animal stayed on the hot plate for 60 sec; for ChR2 experiments, the temperature was set to 52 °C, and a lid was put on top of the cylinder to prevent the animal from jumping out. The number of jumps was manually recorded for 50 sec.

Electronic von Frey test

To measure mechanical sensitivity, the Dynamic Plantar Aesthesiometer (37450, Ugo Basile, Italy) was used and was set to maximum force of 50 g after 20 s. Mice were habituated inside a Plexiglass chamber (10 x 10 x 13 cm) on a metal mesh floor for >2 h until they were awake but largely immobile. The metal rod was placed underneath the left hind paw. The system automatically measured the latency and force delivered upon paw withdrawal. This measurement was taken five times with >1 min intervals. The averaged value was analyzed.

Formalin test

To measure affective pain response, 10 µL of 4% formalin (for hM4Di assays) or 1% formalin (for ChR2 assays) was injected subcutaneously in the left hind paw of an awake mouse. Mice were placed in a Plexiglass chamber (10 x 10 x 13 cm) with a mirror placed behind it. Formalin injection produced a biphasic pain response over a 1 h test period consisting of licks, twitches, and raising or shaking of the injected paw. The number of licks and time spent licking during each 5-min bin were scored through the 1-hour section. The responses during the acute (0–5 min following injection) and the inflammatory phase (20–35 min following injection) were further calculated.

Contextual fear conditioning

The fear conditioning chamber (ENV-007CT, MED Associates) is an arena (26 x 30 x 33 cm) with two Plexiglass walls, two metal walls, and a metal grid floor to deliver electrical shocks (ENV-005, MED Associates). The chamber was connected to a standalone aversive stimulator (ENV-414S, MED Associates) and enclosed in a light- and sound- attenuating cubicle (ENV-018MD, MED Associates). EthoVision XT 12 software with a GigE USB camera with 25 FPS tracked the animal. A 70% ethanol solution and deionized water were used for cleaning immediately after each test. On days 1 and 2, mice underwent two 6-min

habituation sessions in the chamber. On day 3, mice were introduced to the chamber 45–60 min after CNO injection and subsequently received five shocks (2 s, 0.2 mA) with uneven intervals over a 7 min trial. After 24 h, mice were reintroduced to the chamber for a 2-min context-dependent retrieval test. The percentage of time frozen and the total distance moved during each session were calculated by the EthoVision XT 12 software. Freezing behavior was defined as the period during which the velocity of the mouse was less than 1.75 cm/s for at least 3 s. Automatic scoring was validated with manual scoring.

Open field test

A 40 x 40 cm open field arena was used to measure anxiety-like behaviors and general locomotion. Animals were introduced into the center of the open field arena and left to explore the arena for 5 min. Total distance moved, time spent in the center (20 x 20 cm), and entries into the center were measured.

Freezing measurement

For freezing measurement in the projection-specific optogenetics experiment, a 20 x 20 cm chamber was placed in the center of the open field arena. 470 nm laser was triggered with a pattern of 1-min off, 30-s on four times. Freezing behavior was defined as the period during which the velocity of the mouse was less than 1.75 cm/s for at least 3 s. Automatic scoring was validated with manual scoring.

Breathing measurement with pain or anxiety tests

To measure breathing changes under different levels of foot shock stimuli, mice were placed inside a cylindrical, transparent Plexiglass chamber (D = 11 cm, H = 15 cm) inside the fear conditioning chamber (26 x 30 x 33 cm). For the low baseline breathing condition, animals were allowed to habituate for 20–40 min until the baseline breathing rate became

lower than 300 bpm. 0.2 mA or 0.04 mA foot shocks were given for 2 s. To measure breathing changes during the elevated plus maze assay, mice implanted with thermistor sensors were attached to the patch cord and put back into their home cages for a 10-min habituation. Then the test mouse was introduced to the elevated plus maze with transparent walls under a low lighting condition. To measure breathing changes during the elevated platform assay, mice implanted with thermistor sensors were attached to the patch cord, put back into their home cage for baseline recording, and then placed onto an elevated platform (10-cm diameter transparent dish) 100 cm above the floor. Breathing was measured with the thermistor sensor, and velocity and location were measured by the EthoVision XT 12 software. To measure breathing changes during the formalin assay, mice implanted with thermistor sensors were attached to the patch cord and put into the Plexiglass chamber (10 x 10 x 13 cm). After 30 min habituation, 5 mg/kg CNO was injected i.p. into the test mouse. After 30 minutes, 10 μL of 4% formalin was injected subcutaneously into the hind paw. The averaged breathing rate during the acute phase (0–5 min following formalin injection), and the inflammatory phase (15–25 min following injection) were further calculated. The delta breathing rate was calculated by subtracting the averaged rate during the 5 min before each phase.

Quantification and statistical analysis

Quantifications of breathing measurement, fiber photometry, optogenetics, chemogenetics, behavioral tests, and monosynaptic rabies tracing are described in the corresponding sections of text and methods. All data are presented as mean ± SEM. Data were analyzed using either a student's t-test, one-way ANOVA with Tukey's *post hoc* comparison, or two-way ANOVA with Bonferroni's *post hoc* comparison. All statistical analyses were performed with Prism 6 (GraphPad). Statistical significance was defined as

follows: ns, not significant; *, $p < 0.05$; **, $p < 0.01$; ***, $p < 0.001$; ****, $p < 0.0001$. Full details of statistical tests in individual figures are described in the figure legend.

2.4 Results

PBL^{Oprm1} activity is highly correlated with breathing

We investigated the role of PBL^{Oprm1} neurons in breathing by performing concurrent measurements of PBL^{Oprm1} activity and breathing rhythm in freely moving mice. We monitored breathing via micro-thermistor sensor implanted in the nasal cavity, which measured temperature fluctuations between inhaled and exhaled air (Biskamp et al., 2017; Chi et al., 2016; McAfee et al., 2016; Moberly et al., 2018; Moore et al., 2013) without altering normal breathing rhythm (**Figure S2.1A, B**). To monitor PBL^{Oprm1} activity, we delivered a recombinant adeno-associated virus (AAV) encoding the calcium indicator, jGCaMP7s in the PBL of *Oprm1*$^{Cre/+}$ mice and recorded calcium activity with fiber photometry (**Figure 2.1A, B**, validation for MOR co-expression in **Figure S2.1C, D**). Strong cross-correlations were observed between PBL^{Oprm1} activity and breathing rate and plethysmograph amplitude at both second (**Figure 2.1C**) and minute scales (**Figure 2.1D, E, and G**). PBL^{Oprm1} activity closely matched the onset of increases in the plethysmograph amplitude (**Figure 2.1F**) and rate (**Figure 2.1H**) during bouts of high respiratory activity. Interestingly, sighing (identified by the stereotyped respiratory waveforms) (Li et al., 2016) and sniffing events (identified by the rearing-sniffing behaviors) were also strongly associated with PBL^{Oprm1} activity (**Figure 2.1D, S2.1G and H**), indicating that PBL^{Oprm1} neurons are crucial for controlling multiple types of breathing behavior.

To further determine whether this tight correlation is PBL-specific and movement-independent, we expressed Cre-independent GCaMP6f in the dorsal striatum—a region well known for motor control (Kravitz and Kreitzer, 2012)—and simultaneously recorded calcium and breathing signals in freely moving mice. Dorsal striatum activity was tightly correlated with animals' velocity rather than breathing rate, while PBL^{Oprm1} activity was tightly coupled with breathing rate even when mice were stationary (**Figure S2.1I, J**). Finally, to evaluate

whether non-PBL^{Oprm1} populations are also involved in breathing regulation, we injected Cre-off GCaMP6m virus into the PBL of *Oprm1*$^{Cre/+}$ mice. The activity of *Oprm1*-negative neurons responded robustly to noxious stimuli (e.g. pinching, **Figure S2.1N**), but displayed less correlation with the breathing rate and plethysmograph amplitude (**Figure S2.1K–M**, see also **Figure 2.1E, G**).

To determine whether this relationship could be leveraged to predict future changes in PBL^{Oprm1} activity using breathing rhythm (and vice versa), we performed convergent cross-mapping (CCM) analysis (Sugihara et al., 2012). CCM is a manifold-based algorithm that generates predictive models to infer causal relationships of nonlinear time series. When calcium signals were utilized as inputs to generate a CCM model that predicted breathing rate, the predicted trace closely matched the observed trace (**Figure 2.1I**), as in the reverse prediction (**Figure 2.1J**). However, across different training sets, the model that used calcium to predict breathing performed better than the opposite model (**Figure 2.1K**), indicating that PBL^{Oprm1} neuronal activity provided a stronger driving force to regulate breathing rate than vice versa. Together, these results suggest that the PBL^{Oprm1} neurons are tightly involved in breathing regulation.

PBL^{Oprm1} manipulation alters breathing rate

To further investigate the causal roles of PBL^{Oprm1} neurons in breathing regulation, we manipulated their activity using both chemogenetic and optogenetic approaches in awake and anesthetized mice (**Figure 2.2A, G**). Chemogenetic activation of PBL^{Oprm1} neurons by hM3Dq produced significant increases in breathing rate (**Figure 2.2B–D and S2.2B**) but did not change plethysmograph amplitude (**Figure S2.2C**). Conversely, inhibiting PBL^{Oprm1} neurons with hM4Di produced significant decreases in breathing rate (**Figure 2.2E, F, and S2.2H**) and increases in plethysmograph amplitude (**Figure S2.2I**), possibly via compensatory effects mediated by medullary synergistic microcircuits (Cui et al., 2016). CNO

effects were confirmed by *ex vivo* slice electrophysiological recordings with cell-attached or whole-cell configurations (**Figure S2.2A, G**).

To eliminate confounding factors that indirectly affect breathing in awake animals, such as affective state or movement, we also tested the role of PBL^{Oprm1} neurons in breathing regulation using optogenetics in isoflurane-anesthetized animals while simultaneously monitoring breathing via a piezoelectric sensor (Levitt et al., 2015) (**Figure 2.2G, H**). Photostimulating PBL^{Oprm1} neurons with ChR2 significantly increased both breathing rate and plethysmograph amplitude in a frequency-dependent manner (**Figure 2.2I, J, M, N, and S2.2D–F**). Conversely, photoinhibition with ArchT suppressed breathing rate in a light intensity-dependent manner (**Figure 2.2K, L, O, P, and S2.2J**) without affecting the plethysmograph amplitude (**Figure S2.2K, L**). However, repeated photoinhibition resulted in apnea in some test mice (**Figure S2.2M**), suggesting that more potent PBL^{Oprm1} inhibition could simultaneously reduce breathing rate and plethysmograph amplitude. Together, these data suggest PBL^{Oprm1} neurons are necessary and sufficient for the regulation of breathing—specifically breathing rate—across a wide range of physiological states.

Input-output anatomical mapping of PBL^{Oprm1} neurons

Next, we sought to identify direct presynaptic inputs of PBL^{Oprm1} neurons, which could reveal the conditions under which breathing may be modulated. We performed monosynaptic retrograde tracing with G-deleted pseudotyped rabies virus (RVdG), which labels all upstream neurons with red fluorescence (**Figure 2.3A**) (Callaway and Luo, 2015). The specificity of our viral tools was demonstrated by the high MOR co-expression in starter cells (96.7 ± 1.2%, n = 3 mice, total 186 cells) (**Figure S2.3A**) and a negligible number of mCherry-positive cells in WT controls (4 ± 2.65 cells, n = 3 mice) (**Figure S2.3B**). Our rabies tracing results revealed a wide range of PBL^{Oprm1} upstream regions throughout the brain (**Figure 2.3A, B**), including limbic areas—e.g., the central nucleus of the amygdala (CeA),

the bed nucleus of the stria terminalis (BNST), and the parvocellular subparafascicular nucleus (SPFp)—as well as areas relaying sensory and autonomic inputs—e.g., the superior colliculus (SC), the nucleus tractus solitarius (NTS), and the spinal cord (**Figure 2.3A and S2.3C**) (Gauriau and Bernard, 2002; Janak and Tye, 2015; Pautrat et al., 2018; Sahibzada et al., 1986). These data suggest that PBL^{Oprm1} neurons may modulate breathing in response to diverse sensory and emotional challenges.

We also investigated the projection patterns of PBL^{Oprm1} neurons by visualizing their axon terminals that express ChR2:eYFP (**Figure S2.3D**). Interestingly, many of the PBL^{Oprm1} output regions send reciprocal projections to PBL^{Oprm1} neurons, echoing previous reports of the tightly interconnected central autonomic network of PBL, CeA, BNST, and hypothalamus (Saper and Loewy, 1980) and the PBL-preBötC breathing network (Dutschmann and Dick, 2012; Herbert et al., 1990).

Among these outputs, we further characterized the PBL^{Oprm1} projections to the preBötC, the central rhythm and pattern generator of breathing (Ashhad and Feldman, 2020; Smith et al., 1991). We expressed AAVs Cre-dependently expressing tdTomato in the nucleus and synaptophysin-eGFP fusion protein in the axon terminals in the PBL^{Oprm1} neurons (**Figure 2.3C**) and observed eGFP signals from their terminals in the preBötC (**Figure 2.3D**). To functionally characterize this circuit, we expressed hM3Dq or control eYFP in the PBL^{Oprm1} neurons and activated their axon terminals in the preBötC by stereotaxically injecting the potent hM3Dq receptor agonist clozapine (Gomez et al., 2017) directly into the preBötC to facilitate immediate hM3Dq activation (**Figure 2.3F**). Stimulation of PBL^{Oprm1}-preBötC terminals in this manner significantly increased breathing rate (**Figure 2.3E, G**). Collectively, these results indicate that PBL^{Oprm1} neurons can regulate breathing behaviors by

conveying signals from the forebrain, hindbrain, and limbic areas to preBötC rhythm-generating neurons.

Noxious stimuli simultaneously increase breathing rate and PBL^{Oprm1} activity

Noxious and anxiogenic stimuli can elevate breathing rhythm in humans (Bass and Gardner, 1985; Jafari et al., 2017). To investigate this phenomenon in mice, we measured breathing in awake mice while challenging the animals with a noxious stimulus, electric foot shock, and two anxiogenic conditions, the Elevated Plus Maze (EPM) and elevated platform. We found that foot shock-induced breathing changes depended upon basal breathing state and stimulus strength. When mild foot shocks (0.04 mA, 2s) were administered to well-habituated mice with low baseline breathing rates, mice displayed an immediate increase in breathing rate as well as locomotor activity (**Figure S2.4A**). However, when stronger foot shocks typically used in fear conditioning (0.2 mA, 2s) were administered to well-habituated mice, mice displayed an initial increase in breathing rate followed by a marked decrease while switching from a stationary pose to a hectic running/jumping behavior (**Figure S2.4B**). When the same magnitude of foot shock (0.2 mA, 2s) was administered to unhabituated mice with high baseline breathing rates, mice immediately decreased their breathing rate and initiated running/jumping behavior (**Figure S2.4C**). These different breathing responses to foot shock suggest that pain-induced breathing change is influenced by multiple factors: the baseline breathing rate, the intensity of the noxious stimuli, and the animal's locomotor activity. During EPM assay, breathing rate decreased as mice exited the open arm and increased as they entered the open arm (**Figure S2.4D, E**). To minimize the involvement of locomotor activity while monitoring anxiety-induced changes in breathing, we placed the animals on an elevated circular platform (10 cm diameter, 100 cm elevated from the floor), which increased the breathing rate and plethysmograph amplitude compared to the home

cage (**Figure S2.4F–H**). These data suggest that affective states and breathing behaviors are tightly correlated in mice.

Since PBL^{Oprm1} neurons receive monosynaptic inputs from the brain areas that mediate pain perception (**Figure 2.3A, B and S2.3C**), they may also be actively involved in breathing increases induced by pain. To explore this possibility, we monitored breathing and PBL^{Oprm1} activity simultaneously during noxious stimulus presentation in both anesthetized and awake mice. In anesthetized mice, we recorded breathing with piezoelectric sensors and calcium signals with fiber photometry (**Figure 2.4A, F**). We challenged the animals with noxious thermal stimuli by touching the tail with a hot rod (55 ^{o}C) (**Figure 2.4A**) and observed an immediate increase in breathing rate (**Figure 2.4B, C**), plethysmograph amplitude (**Figure S2.4I, J**), and PBL^{Oprm1} activity (**Figure 2.4D, E**). Noxious mechanical stimulus (tail pinch with 300 g pressure) (**Figure 2.4F**) also robustly increased breathing rate (**Figure 2.4G, H**), plethysmograph amplitude (**Figure S2.4K, L**), and calcium signals (**Figure 2.4I, J**).

Next, we delivered the noxious thermal stimulus to freely moving mice by first habituating them on a room-temperature metal plate and then increasing the surface temperature to 55°C (**Figure 2.4K**). We observed dramatic increases in breathing rate (**Figure 2.4L–N**), plethysmograph amplitude (**Figure S2.4M, N**), and calcium signals, as well as tight correlations of calcium signals with both breathing rate (**Figure 2.4O**) and amplitude (**Figure S2.4O**). These data indicate that PBL^{Oprm1} neurons are strongly activated by painful stimuli and exhibit dynamics that closely resembles breathing across a broad range of physiological conditions.

Since inhibiting PBL^{Oprm1} neurons decreased breathing, we tested whether doing so could also override pain-induced hyperventilation. Therefore, we optogenetically silenced PBL^{Oprm1} neurons in anesthetized mice with ArchT and monitored breathing rhythm after

applying noxious stimuli (**Figure 2.4P**). Optogenetic PBL^{Oprm1} inhibition significantly attenuated thermal (**Figure 2.4Q**) and mechanical (**Figure 2.4R**) pain-induced increases in breathing rate but did not affect the control group. These results indicate that silencing PBL^{Oprm1} neurons can counteract pain-induced hyperventilation, possibly by lowering baseline breathing rate (**Figure 2.2**) or blocking stimulus-evoked breathing changes (Jiang et al., 2004).

PBL^{Oprm1} inhibition alleviates affective pain and anxiety-like behaviors

Since PBL^{Oprm1} neurons reciprocally project to pain and emotional processing areas such as the CeA and BNST (**Figure 2.3A, B and S2.3C, D**), we hypothesized that they also mediate pain perception and anxiety-like behaviors. However, inhibiting PBL^{Oprm1} neurons by hM4Di did not alter thermal or mechanical pain sensitivity, as measured by paw withdrawal latencies in hot plate (**Figure 2.5A, B**) and von Frey tests (**Figure 2.5D, E**). These results are consistent with a recent report that parabrachial manipulation did not alter baseline pain sensitivity (Chiang et al., 2020). However, these hM4Di animals showed a longer latency to jump (**Figure 2.5C**), suggesting reduced motivation to escape from the hot plate which implies a lower level of affective-motivation pain (Han et al., 2015).

To further assess affective-motivational pain perception, we performed the formalin test (**Figure 2.5F**), which evaluates chemical and inflammatory pain by measuring biphasic licking responses to formalin injection during the first and second inflammatory phases (Le Bars et al., 2001). The first acute phase is mediated by direct stimulation of the nociceptors, while the second inflammatory phase is modulated by areas that process affective pain (Huang et al., 2006; Vaccarino and Melzack, 1989). Compared to controls, hM4Di-expressing mice displayed attenuated paw-licking behaviors in the second but not the first phase, indicating that chemogenetic inhibition of PBL^{Oprm1} neurons reduced affective pain, but not detection of the peripheral stimulus (**Figure 2.5G and S2.5A–E**). We also performed

contextual fear conditioning tests to further evaluate the affective pain response (**Figure 2.5H**). In classical Pavlovian fear conditioning, the unpleasantness of foot shock-induced acute pain drives the animal to display defensive responses and associate specific cues or contexts with fear; thus, the freezing behavior during and after conditioning correlate with the affective aspect of pain. hM4Di mice displayed less freezing than controls in both conditioning (**Figure 2.5I**) and the fear memory retrieval phase (**Figure 2.5J**). Together, these results indicate that inhibiting PBL^{Oprm1} neurons attenuates affective pain perception without altering sensory pain perception.

To further examine the role of PBL^{Oprm1} neurons in mediating negative affect, we first performed the Elevated Plus Maze (EPM) test to test anxiety-like behaviors. The hM4Di-expressing group spent a significantly longer time in the open arms (**Figure 2.5K–M**), visited open arms more frequently (**Figure S2.5F**), and traveled longer distances (**Figure S2.5G**) compared to the control group, indicating that PBL^{Oprm1} neurons are also involved in mediating anxiety. Next, to test whether PBL^{Oprm1} neurons encode positive or negative valence, we performed real-time place preference/aversion (RTPP/RTPA) tests with ArchT (**Figure 2.5N–P**) or ChR2 (**Figure 2.5Q–S**) optogenetics. ArchT-expressing mice stayed significantly longer in the “light-on” chamber compared to the “light-off chamber”, whereas the control group spent equal time in both chambers (**Figure 2.5P**). Although we observed apnea in some anesthetized mice following repeated optogenetic inhibition (**Figure S2.2M**), we did not observe it in mice during the behavioral test, likely due to the different baseline breathing rates between awake (300–600 bpm) and anesthetized animals (<100 bpm). Conversely, the ChR2-expressing mice displayed avoidance behavior toward the “light-on” chamber (**Figure 2.5S**). Overall, these results indicate that PBL^{Oprm1} inactivation alleviated affective pain and anxiety-like behavior while encoding positive valence, whereas PBL^{Oprm1} activation contributed to pain-induced hyperventilation and encoded negative valence.

Single PBL^{Oprm1} neurons respond to both breathing and pain

It is possible that a homogenous PBL^{Oprm1} population may regulate both breathing and pain, or alternatively, heterogeneous subpopulations of PBL^{Oprm1} neurons may independently regulate these behaviors. To test these possibilities, we first investigated the molecular heterogeneity of PBL^{Oprm1} neurons. We performed RNAscope *in situ* hybridization for *Oprm1* and seven known markers of the dorsal (PBdl) and external lateral PB (PBel), namely, the *Calca*, *Tac1*, *Nts*, *Htr2a*, *FoxP2*, *Pdyn*, and *Tacr1* genes, many of which have been reported to mediate pain and breathing behaviors, such as escape and hypercapnic arousal (Barik et al., 2018; Chiang et al., 2020; Deng et al., 2020; Han et al., 2015; Kaur et al., 2020). *Oprm1* transcripts were found in both the PBdl and PBel, exhibiting 10-40% co-localization with each marker gene tested (**Figure S2.6A, B**).

Since PBL^{Oprm1} neurons are molecularly heterogenous, we performed miniscope single-cell calcium imaging to compare the responses of individual PBL^{Oprm1} neurons to breathing and pain (pinching) in the same animal (**Figure 2.6A**). Many neurons displayed activities correlated with breathing (**Figure 2.6B**) and pinching (**Figure 2.6C**). Among 108 cells recorded, 62.0% responded both to breathing and pain (**Figure 2.6D, E**), 14.8% responded to breathing only (**Figure 2.6F**), and 21.3% responded only to pinching (**Figure 2.6G**). These results indicate that the majority of the PBL^{Oprm1} neurons are recruited by both breathing and pain behaviors.

Two distinct PBL^{Oprm1} subpopulations diverge to emotion-processing and breathing centers

PBL^{Oprm1} neurons project to many areas, including medullary breathing centers and limbic regions that process pain and emotion (**Figure S2.3C, D**). To determine whether single PBL^{Oprm1} neurons collaterally project to both areas, or two different subpopulations divergently project to each area, we performed projection-specific anatomical tracing using

intersectional viral approaches. First, we injected retrogradely transported AAVs Cre-dependently encoding mCherry into the CeA of *Oprm1*$^{Cre/+}$ mice to label CeA-projecting PBL^{Oprm1} neurons (*Oprm1*$^{PBL\rightarrow CeA}$ neurons) with mCherry. In the same animals, we then injected retrograde AAVs encoding Cre-dependent codon-optimized FLP-recombinase (FLPo) into the preBötC and FLP-dependent ChR2-eYFP into the PBL to label preBötC-projecting PBL^{Oprm1} neurons (*Oprm1*$^{PBL\rightarrow preBötC}$ neurons) with eYFP (**Figure 2.7A**). Interestingly, these two subpopulations were anatomically segregated. The CeA-projecting neurons were clustered in the PBel while the preBötC-projectors were localized to the surrounding central lateral (PBcl), lateral crescent (PBlc), and the ventral PBel regions, together forming a "core-shell" like structure (**Figure 2.7B and S2.7A, B**) with little overlap (**Figure 2.7C**). Although the PBel and PBlc have previously been distinguished based on projection patterns (Chamberlin and Saper, 1992; Herbert et al., 1990; Yokota et al., 2015), this distinctive core-shell pattern at the same coronal and horizontal levels has not been previously reported. Moreover, the core (*Oprm1*$^{PBL\rightarrow CeA}$) and shell (*Oprm1*$^{PBL\rightarrow preBötC}$) neurons projected to largely non-overlapping downstream regions. The core neurons projected to forebrain areas including the BNST and the intralaminar nucleus (ILN), while the shell neurons extensively projected to hindbrain areas including the caudal pontine reticular nucleus (PnC), retrotrapezoid nucleus (RTN), NTS, spinal vestibular nucleus (SpIV), and spinal trigeminal nucleus (SpV) (**Figure S2.7C, D**). These results imply that the core and shell neurons may exert different functions via projections to the forebrain and the hindbrain, respectively.

Core and shell PBL^{Oprm1} neurons differentially regulate breathing, pain, and anxiety

To test whether core and shell PBL^{Oprm1} subpopulations are differentially involved in breathing and pain regulation, we first simultaneously monitored the activities of each subpopulation and breathing (**Figure 2.7D, I**). The activities of both core and shell neurons

were tightly correlated with breathing rate (**Figure 2.7E, F, J, and K**) and plethysmograph amplitude (**Figure S2.7E, F, L, and M**). Moreover, the breathing rhythm and the activities of each population increased concurrently upon delivery of noxious thermal (**Figure 2.7G, L, S2.7G, H, N, and O**) and mechanical stimuli (same stimuli as in **Figure 2.4**) (**Figure S2.7I–K and S2.7P–R**) in anesthetized mice. Interestingly, breathing rate changes during sniffing events were correlated with activity of shell but not core neurons (**Figure 2.7H, M**). These results indicate that the core and shell neurons are differentially involved in regulating breathing rhythm.

We then performed projection-specific manipulation experiments to investigate the roles of each subpopulation in regulating breathing, affective pain perception, and anxiety-like behaviors by expressing ChR2 and hM4Di in each population using intersectional viral tools (**Figure 2.8A, F**). ChR2-mediated stimulation of core neurons significantly increased breathing rate (**Figure 2.8B**), number of jumps on the hot plate (Barik et al., 2018; Han et al., 2015) (**Figure 2.8C**), and paw licking behavior during the inflammatory phase of the formalin assay (**Figure S2.8A–C**). To examine negative affective behaviors, we performed the EPM, RTPA, and open field freezing tests while activating the core neurons. Compared to controls, animals expressing ChR2 in the core neurons avoided the light-paired chamber in the RTPA test (**Figure 2.8D**), spent significantly less time in the open arm during the EPM test (**Figure 2.8E**), and displayed freezing behaviors in the open field arena when given repeated photostimulation (**Figure S2.8D**). Similar to the core neurons, photostimulation of shell neurons not only elevated breathing rate (**Figure 2.8G**) but also exacerbated affective pain perception (**Figure 2.8H** for hot plate and **S2.8E–G** for formalin assay) and promoted behaviors associated with negative affect (**Figure 2.8I** for RTPA, **2.8J** for EPM, and **S2.8H** for freezing).

For loss-of-function experiments, we inhibited each subpopulation with hM4Di (Runegaard et al., 2018) (**Figure 2.8K, P**). Chemogenetic inhibition of core neurons not only significantly reduced baseline breathing rate (**Figure 2.8L**) but also markedly alleviated affective pain perception (**Figure 2.8M, S2.8I–M** for formalin assay, and **2.8N** for hot plate assay) and anxiety responses (**Figure 2.8O** for EPM, and **S2.8N, O** for open field test). Chemogenetic inhibition of shell neurons also decreased baseline breathing rate (**Figure 2.8Q**), but did not affect affective pain responses (**Figure 2.8R and S2.8P–T** for formalin assay, **Figure 2.8S** for hot plate assay) or anxiety-like behaviors (**Figure 2.8T for** EPM and **Figure S2.8U, V** for open field test) as in the core neurons. These results indicate that both core and shell neurons actively regulate breathing and affective behaviors such as pain and anxiety, but at different levels. Both the core and shell neurons are indispensable for regulating breathing. The core neurons are sufficient and necessary for regulating affective pain and anxiety-like behaviors, whereas the shell neurons are only sufficient but not required for these behaviors.

To test whether shell neurons are necessary for pain-induced breathing increase, if not the pain response itself, we again chemogenetically inhibited the shell neurons and then measured pain-induced breathing changes during the formalin assay (**Figure S2.8W**). During the acute pain period, both the hM4Di and eYFP animals displayed similar levels of dynamic breathing rate changes accompanying excessive licking behaviors (**Figure S2.8X**). However, only the eYFP group displayed a breathing rate increase during the inflammatory pain phase (**Figure S2.8Y**). These results indicate that the shell neurons are required to regulate pain-induced breathing changes, as well as basal breathing rhythm.

PBL^{Oprm1} subpopulations send excitatory inputs to each other

Inhibiting the PBL^{Oprm1} subpopulations resulted in different outcomes in pain and anxiety, yet optogenetic stimulation of both subpopulations induced the same phenotype. We

therefore wondered if the PBL^{Oprm1} subpopulations reciprocally interact with each other. To explore this possibility, we performed projection-specific *ex vivo* whole-cell patch-clamp electrophysiological recording using the same intersectional approach described above (**Figure 2.7A**) to record one subpopulation expressing mCherry while stimulating the other subpopulation via ChR2 (**Figure 2.8U**). Photostimulation of the core neurons evoked excitatory postsynaptic currents (oEPSC) in 42.86% of the shell neurons (**Figure 2.8W**), and stimulating the shell neurons evoked oEPSC in 73.33% of the core neurons (**Figure 2.8Y**). Moreover, we observed that both responses were glutamatergic since no inhibitory postsynaptic current was detected by photostimulation, and the application of the AMPA receptor antagonist CNQX abolished all oEPSCs (**Figure 2.8V, X**). Our data suggest that PBL^{Oprm1} neurons integrate breathing with pain and anxiety via a reciprocally connected excitatory network of core and shell subpopulations that divergently project to the CeA and the preBötC (**Figure 2.8Z**).

2.5 Discussion

By combining cell type- and projection-specific circuit dissection tools with respiratory monitoring approaches, we identify the PBL^{Oprm1} neurons that simultaneously regulate breathing and negative affect through two anatomically distinct but interconnected core and shell subpopulations that diverge to the limbic and medullary breathing areas. We also find that these core/shell subpopulations are reciprocally interconnected with excitatory synapses to collectively regulate breathing, pain, and anxiety-like behaviors. Together, these data provide a circuit-based mechanism of coordinating breathing with pain and emotions.

Our results demonstrate that PBL^{Oprm1} neurons consist of two non-overlapping subpopulations with a “core-shell” configuration determined by divergent projections to the CeA and preBötC. Both the core *Oprm1*$^{PBL\rightarrow CeA}$ and shell *Oprm1*$^{PBL\rightarrow preBötC}$ neurons directly

regulate breathing rhythm, but only the shell neurons are involved in behaviorally entrained breathing behaviors such as sniffing, indicating that these two subpopulations play different roles in breathing regulation. These results are in line with previous reports implicating the existence of the PBL→preBötC breathing circuit (Chamberlin and Saper, 1992; Ellenberger and Feldman, 1990; Fulwiler and Saper, 1984; Herbert et al., 1990), and the involvement of CeA in breathing regulation (Frysinger et al., 1988; Nobis et al., 2018; Yang et al., 2020).

Our results also show that the core *Oprm1*$^{PBL→CeA}$ and shell *Oprm1*$^{PBL→preBötC}$ neurons are differentially involved in regulating pain perception. Optogenetic stimulation of both the core and shell populations exacerbated affective pain and negative emotional behaviors. Chemogenetic inhibition of core neurons substantially attenuates the behaviors associated with affective pain and negative emotions, but these behaviors were unaltered by chemogenetic inhibition of the shell neurons. These results indicate that the core and shell subpopulations are differentially involved in regulating negative affect (e.g., affective pain and anxiety).

Based on these results, we speculate that the dynamic interplays of breathing and negative affect, such as pain-induced hyperventilation (Jafari et al., 2017), hyperventilation during panic attack (Bass and Gardner, 1985), or exacerbated negative affect by voluntary hyperventilation (Hornsveld et al., 1995; Lum, 1981) can be mediated by the recurrent excitatory connection between core and shell PBL^{Oprm1} neurons, and their differential involvement in regulating pain and breathing. However, it should be noted that breathing and negative affect do not always influence each other. For example, a rapid increase of breathing induced by emotionally neutral behaviors, such as sniffing and exercise, does not recruit changes in negative affect. Reciprocally connected core-shell PBL^{Oprm1} neurons may not be involved in these conditions. Instead, shell neurons that do not make synapse onto

the core neurons, possibly the “breathing only” population in **Figure 2.6**, may be actively involved in these conditions. Indeed, the shell neurons, not core neurons, are highly correlated with breathing during exploratory sniffing (**Figure 2.7H, M**). Moreover, chemogenetic inhibition of core neurons, not shell neurons, reduced affective pain and anxiety (**Figure 2.8**). These results suggest that inputs inhibiting PBL^{Oprm1} neurons can alleviate negative affect only by acting upon the core neurons. These results also imply that the hypoalgesia by controlled slow breathing likely requires the recruitment of the cortex or limbic system (Jafari et al., 2017), and are not driven by inhibiting the shell *Oprm1*$^{PBL\rightarrow preBötC}$ neurons.

PBL^{Oprm1} neurons receive monosynaptic inputs from a broad array of sensory and limbic areas and in turn relay this information to both the breathing and affective pain networks through the core and shell neurons (**Figure S2.8Z**). Notably, the core and shell neurons form a recurrent excitatory network, which is uniquely positioned to converge brain-wide top-down and bottom-up inputs and collectively control breathing and internal affective states. Furthermore, these inputs are not limited to pain or anxiety, but can be expanded to a broader range, such as visceral or gustatory inputs relayed by the NTS (Duschek et al., 2013) that is reciprocally connected with the PBL^{Oprm1} neurons (**Figure 2.4 and S2.4**).

The fact that the PBL^{Oprm1} neurons regulate pain and breathing also explains why opioids can simultaneously inhibit both pain and breathing, manifested as opioid analgesia and OIRD. Indeed, PBL^{Oprm1} inhibition by excessive opioids is one of the neural mechanisms of OIRD (Liu et al., 2021). The endogenous opioid system in the PBL has been less explored, however. Possible upstream sources of endogenous opioids in the PBL include proopiomelanocortin (*Pomc*) neurons in the NTS (Wang et al., 2015), proenkephalin (*Penk*) neurons in the CeA (Kim et al., 2017), and prodynorphin (*Pdyn*) and *Penk* neurons in the PB

(Norris et al., 2021). Future studies exploring the modulation of PBL^{Oprm1} neurons by these endogenous opioids are needed to understand the endogenous roles of PBL^{Oprm1} neurons as the converging hub of emotional, sensory, and physiological functions.

2.6 Acknowledgments

This chapter, in full, is a reprint of the material as it appears in **Liu, S.**, Ye, M., Pao, G.M., Song, S., Jhang, J., Jiang, H., Kim, J.H., Kang, S., Kim, D., Han, S. Divergent brainstem opioidergic pathways that coordinate breathing with pain and emotions. *Neuron*, (2021). S0896-6273(21)00990-9. The dissertation author was a primary investigator and the first author of this material. The authors would like to thank the Han lab members for the critical discussion of the paper, Dr. Jane Chen for the technical support of Miniscope calcium imaging, and Benjamin Roberts for the stylistic editing of the manuscript. Supported by grants from the US National Institutes of Health (1R01MH116203 to S.H. and P30 014195 to the Salk Institute), Brain Research Foundation Fay/Frank Seed Grant (to S.H.), the Salk Women & Science Special Award, the Mary K. Chapman Foundation, and the Jesse & Caryl Philips Foundation graduate fellowships (to S.L.).

2.7 References

Abrams, D.J., Zheng, L., Choo, K.S., Yang, J.J., Wei, W., Anchordoquy, T.J., Zawia, N.H., and Stevens, K.E. (2008). An initial animal proof-of-concept study for central administration of clozapine to schizophrenia patients. Schizophr. Res. *100*, 86-96.

Ashhad, S., and Feldman, J.L. (2020). Emergent elements of inspiratory rhythmogenesis: network synchronization and synchrony propagation. Neuron *106*, 482-497.e484.

Bachmutsky, I., Wei, X.P., Kish, E., and Yackle, K. (2020). Opioids depress breathing through two small brainstem sites. eLife *9*, e52694.

Barik, A., Thompson, J.H., Seltzer, M., Ghitani, N., and Chesler, A.T. (2018). A brainstem-spinal circuit controlling nocifensive behavior. Neuron *100*, 1491-1503.e1493.

Bass, C., and Gardner, W. (1985). Emotional influences on breathing and breathlessness. J. Psychosom. Res. *29*, 599-609.

Bautista, T.G., Sun, Q.-J., and Pilowsky, P.M. (2014). The generation of pharyngeal phase of swallow and its coordination with breathing: interaction between the swallow and respiratory central pattern generators. Prog. Brain. Res. *212*, 253-275.

Biskamp, J., Bartos, M., and Sauer, J.-F. (2017). Organization of prefrontal network activity by respiration-related oscillations. Sci. Rep. *7*, 1-11.

Boiten, F.A., Frijda, N.H., and Wientjes, C.J.E. (1994). Emotions and respiratory patterns: review and critical analysis. Int. J. Psychophysiol. *17*, 103-128.

Callaway, E.M., and Luo, L. (2015). Monosynaptic circuit tracing with glycoprotein-deleted rabies viruses. J. Neurosci. *35*, 8979-8985.

Chamberlin, N.L. (2004). Functional organization of the parabrachial complex and intertrigeminal region in the control of breathing. Respir. Physiol. Neurobiol. *143*, 115-125.

Chamberlin, N.L., Mansour, A., Watson, S.J., and Saper, C.B. (1999). Localization of mu-opioid receptors on amygdaloid projection neurons in the parabrachial nucleus of the rat. Brain. Res. *827*, 198-204.

Chamberlin, N.L., and Saper, C.B. (1992). Topographic organization of cardiovascular responses to electrical and glutamate microstimulation of the parabrachial nucleus in the rat. J. Comp. Neurol. *326*, 245-262.

Chamberlin, N.L., and Saper, C.B. (1994). Topographic organization of respiratory responses to glutamate microstimulation of the parabrachial nucleus in the rat. J. Neurosci. *14*, 6500-6510.

Chi, V.N., Müller, C., Wolfenstetter, T., Yanovsky, Y., Draguhn, A., Tort, A.B., and Brankačk, J. (2016). Hippocampal respiration-driven rhythm distinct from theta oscillations in awake mice. J. Neurosci. *36*, 162-177.

Chiang, M.C., Nguyen, E.K., Canto-Bustos, M., Papale, A.E., Oswald, A.-M.M., and Ross, S.E. (2020). Divergent neural pathways emanating from the lateral parabrachial nucleus mediate distinct components of the pain response. Neuron *106*, 927-939.e925.

Chow, B.Y., Han, X., and Boyden, E.S. (2012). Genetically encoded molecular tools for light-driven silencing of targeted neurons. Prog. Brain. Res. *196*, 49-61.

Chow, B.Y., Han, X., Dobry, A.S., Qian, X., Chuong, A.S., Li, M., Henninger, M.A., Belfort, G.M., Lin, Y., and Monahan, P.E. (2010). High-performance genetically targetable optical neural silencing by light-driven proton pumps. Nature *463*, 98-102.

Cohen, M.I. (1971). Switching of the respiratory phases and evoked phrenic responses produced by rostral pontine electrical stimulation. J. Physiol. *217*, 133-158.

Cui, Y., Kam, K., Sherman, D., Janczewski, W.A., Zheng, Y., and Feldman, J.L. (2016). Defining preBötzinger complex rhythm- and pattern-generating neural microcircuits in vivo. Neuron *91*, 602-614.

Dahan, A., Sarton, E., Teppema, L., Olievier, C., Nieuwenhuijs, D., Matthes, H.W., and Kieffer, B.L. (2001). Anesthetic potency and influence of morphine and sevoflurane on respiration in mu-opioid receptor knockout mice. Anesthesiology *94*, 824-832.

Del Negro, C.A., Funk, G.D., and Feldman, J.L. (2018). Breathing matters. Nat. Rev. Neurosci. *19*, 351-367.

Deng, J., Zhou, H., Lin, J.K., Shen, Z.X., Chen, W.Z., Wang, L.H., Li, Q., Mu, D., Wei, Y.C., Xu, X.H. and Sun, Y.G. (2020). The parabrachial nucleus directly channels spinal nociceptive signals to the intralaminar thalamic nuclei, but not the amygdala. Neuron *107*, 909-923.e906.

Deyle, E.R., and Sugihara, G. (2011). Generalized theorems for nonlinear state space reconstruction. PLoS One *6*, e18295.

Dick, T.E., Dutschmann, M., Feldman, J.L., Fong, A.Y., Hulsmann, S., Morris, K.M., Ramirez, J.M., Smith, J.C., and Respiratory Neurobiology, C. (2018). Facts and challenges in respiratory neurobiology. Respir. Physiol. Neurobiol. *258*, 104-107.

Duschek, S., Werner, N.S., and Reyes Del Paso, G.A. (2013). The behavioral impact of baroreflex function: a review. Psychophysiology *50*, 1183-1193.

Dutschmann, M., and Dick, T.E. (2012). Pontine mechanisms of respiratory control. Compr. Physiol. *2*, 2443-2469.

Dutschmann, M., and Herbert, H. (2006). The Kölliker-Fuse nucleus gates the postinspiratory phase of the respiratory cycle to control inspiratory off-switch and upper airway resistance in rat. Eur. J. Neurosci. *24*, 1071-1084.

Ellenberger, H., and Feldman, J. (1990). Brainstem connections of the rostral ventral respiratory group of the rat. Brain. Res. *513*, 35-42.

Feleky, A. (1916). The influence of the emotions on respiration. J. Exp. Psychol. *1*, 218-241.

Fraser, A.M., and Swinney, H.L. (1986). Independent coordinates for strange attractors from mutual information. Phys. Rev. A. Gen. Phys. *33*, 1134-1140.

Frysinger, R.C., Zhang, J., and Harper, R.M. (1988). Cardiovascular and respiratory relationships with neuronal discharge in the central nucleus of the amygdala during sleep-waking states. Sleep *11*, 317-332.

Fulwiler, C.E., and Saper, C.B. (1984). Subnuclear organization of the efferent connections of the parabrachial nucleus in the rat. Brain. Res. Rev. *7*, 229-259.

Gauriau, C., and Bernard, J.-F. (2002). Pain pathways and parabrachial circuits in the rat. Exp. Physiol. *87*, 251-258.

Gomez, J.L., Bonaventura, J., Lesniak, W., Mathews, W.B., Sysa-Shah, P., Rodriguez, L.A., Ellis, R.J., Richie, C.T., Harvey, B.K., Dannals, R.F. and Pomper, M.G. (2017). Chemogenetics revealed: DREADD occupancy and activation via converted clozapine. Science *357*, 503-507.

Han, S., Soleiman, M.T., Soden, M.E., Zweifel, L.S., and Palmiter, R.D. (2015). Elucidating an affective pain circuit that creates a threat memory. Cell *162*, 363-374.

Herbert, H., Moga, M.M., and Saper, C.B. (1990). Connections of the parabrachial nucleus with the nucleus of the solitary tract and the medullary reticular formation in the rat. J. Comp. Neurol. *293*, 540-580.

Hornsveld, H., Garssen, B., and van Spiegel, P. (1995). Voluntary hyperventilation: the influence of duration and depth on the development of symptoms. Biol. Psychol. *40*, 299-312.

Huang, J., Chang, J.-Y., Woodward, D.J., Baccalá, L.A., Han, J.-S., Wang, J.-Y., and Luo, F. (2006). Dynamic neuronal responses in cortical and thalamic areas during different phases of formalin test in rats. Exp. Neurol. *200*, 124-134.

Jafari, H., Courtois, I., Van den Bergh, O., Vlaeyen, J.W.S., and Van Diest, I. (2017). Pain and respiration: a systematic review. Pain *158*, 995-1006.

Janak, P.H., and Tye, K.M. (2015). From circuits to behaviour in the amygdala. Nature *517*, 284-292.

Jiang, M., Alheid, G.F., Calandriello, T., and McCrimmon, D.R. (2004). Parabrachial-lateral pontine neurons link nociception and breathing. Respir. Physiol. Neurobiol. *143*, 215-233.

Kaur, S., De Luca, R., Khanday, M.A., Bandaru, S.S., Thomas, R.C., Broadhurst, R.Y., Venner, A., Todd, W.D., Fuller, P.M., and Arrigoni, E. (2020). Role of serotonergic dorsal raphe neurons in hypercapnia-induced arousals. Nat. Commun. *11*, 1-15.

Kim, J., Zhang, X., Muralidhar, S., LeBlanc, S.A., and Tonegawa, S. (2017). Basolateral to central amygdala neural circuits for appetitive behaviors. Neuron *93*, 1464-1479.e1465.

Kravitz, A.V., and Kreitzer, A.C. (2012). Striatal mechanisms underlying movement, reinforcement, and punishment. Physiology *27*, 167-177.

Le Bars, D., Gozariu, M., and Cadden, S.W. (2001). Animal models of nociception. Pharmacol. Rev. *53*, 597-652.

Levitt, E.S., Abdala, A.P., Paton, J.F., Bissonnette, J.M., and Williams, J.T. (2015). Mu opioid receptor activation hyperpolarizes respiratory-controlling Kölliker-Fuse neurons and suppresses post-inspiratory drive. J. Physiol. *593*, 4453-4469.

Li, P., Janczewski, W.A., Yackle, K., Kam, K., Pagliardini, S., Krasnow, M.A., and Feldman, J.L. (2016). The peptidergic control circuit for sighing. Nature *530*, 293-297.

Liu, S., Kim, D.-I., Oh, T.G., Pao, G.M., Kim, J.-H., Palmiter, R.D., Banghart, M.R., Lee, K.-F., Evans, R.M., and Han, S. (2021). Neural basis of opioid-induced respiratory depression and its rescue. Proc. Natl. Acad. Sci. USA *118*, 23.

Lum, L. (1981). Hyperventilation and anxiety state (SAGE Publications Sage UK: London, England).

Mahn, M., Saraf-Sinik, I., Patil, P., Pulin, M., Bitton, E., Karalis, N., Bruentgens, F., Palgi, S., Gat, A., Dine, J. and Wietek, J. (2021). Efficient optogenetic silencing of neurotransmitter release with a mosquito rhodopsin. Neuron *109*, 1621-1635.

Matthes, H.W., Maldonado, R., Simonin, F., Valverde, O., Slowe, S., Kitchen, I., Befort, K., Dierich, A., Le Meur, M., Dollé, P. and Tzavara, E. (1996). Loss of morphine-induced analgesia, reward effect and withdrawal symptoms in mice lacking the mu-opioid-receptor gene. Nature *383*, 819-823.

McAfee, S.S., Ogg, M.C., Ross, J.M., Liu, Y., Fletcher, M.L., and Heck, D.H. (2016). Minimally invasive highly precise monitoring of respiratory rhythm in the mouse using an epithelial temperature probe. J. Neurosci. Methods *263*, 89-94.

Moberly, A.H., Schreck, M., Bhattarai, J.P., Zweifel, L.S., Luo, W., and Ma, M. (2018). Olfactory inputs modulate respiration-related rhythmic activity in the prefrontal cortex and freezing behavior. Nat. Commun. *9*, 1528.

Montandon, G., Qin, W., Liu, H., Ren, J., Greer, J.J., and Horner, R.L. (2011). PreBötzinger complex neurokinin-1 receptor-expressing neurons mediate opioid-induced respiratory depression. J. Neurosci. *31*, 1292-1301.

Moore, J.D., Deschenes, M., Furuta, T., Huber, D., Smear, M.C., Demers, M., and Kleinfeld, D. (2013). Hierarchy of orofacial rhythms revealed through whisking and breathing. Nature *497*, 205-210.

Mortola, J.P., and Frappell, P.B. (1998). On the barometric method for measurements of ventilation, and its use in small animals. Can. J. Physiol. Pharmacol. *76*, 937-944.

Navarrete-Opazo, A.A., Cook-Snyder, D.R., Miller, J.R., Callison, J.J., McCarthy, N., Palkovic, B., Stuth, E.A., Zuperku, E.J., and Stucke, A.G. (2020). Endogenous glutamatergic inputs to the Parabrachial Nucleus/Kölliker-Fuse Complex determine respiratory rate. Respir. Physiol. Neurobiol. *277*, 103401.

Nobis, W.P., Schuele, S., Templer, J.W., Zhou, G., Lane, G., Rosenow, J.M., and Zelano, C. (2018). Amygdala-stimulation-induced apnea is attention and nasal-breathing dependent. Ann. Neurol. *83*, 460-471.

Norris, A.J., Shaker, J.R., Cone, A.L., Ndiokho, I.B., and Bruchas, M.R. (2021). Parabrachial opioidergic projections to preoptic hypothalamus mediate behavioral and physiological thermal defenses. eLife *10*, e60779.

Palmiter, R.D. (2018). The parabrachial nucleus: CGRP neurons function as a general alarm. Trends Neurosci. *41*, 280-293.

Pautrat, A., Rolland, M., Barthelemy, M., Baunez, C., Sinniger, V., Piallat, B., Savasta, M., Overton, P.G., David, O., and Coizet, V. (2018). Revealing a novel nociceptive network that links the subthalamic nucleus to pain processing. eLife *7*, e36607.

Prkic, I., Mustapic, S., Radocaj, T., Stucke, A.G., Stuth, E.A., Hopp, F.A., Dean, C., and Zuperku, E.J. (2012). Pontine mu-opioid receptors mediate bradypnea caused by intravenous remifentanil infusions at clinically relevant concentrations in dogs. J. Neurophysiol. *108*, 2430-2441.

Runegaard, A.H., Sørensen, A.T., Fitzpatrick, C.M., Jørgensen, S.H., Petersen, A.V., Hansen, N.W., Weikop, P., Andreasen, J.T., Mikkelsen, J.D., and Perrier, J.-F. (2018). Locomotor-and reward-enhancing effects of cocaine are differentially regulated by chemogenetic stimulation of Gi-signaling in dopaminergic neurons. eNeuro *5*, 3.

Sahibzada, N., Dean, P., and Redgrave, P. (1986). Movements resembling orientation or avoidance elicited by electrical stimulation of the superior colliculus in rats. J. Neurosci. *6*, 723.

Saper, C.B., and Loewy, A.D. (1980). Efferent connections of the parabrachial nucleus in the rat. Brain. Res. *197*, 291-317.

Smith, J.C., Ellenberger, H.H., Ballanyi, K., Richter, D.W., and Feldman, J.L. (1991). Pre-Bötzinger complex: a brainstem region that may generate respiratory rhythm in mammals. Science *254*, 726-729.

Smotherman, M., Schwartz, C., and Metzner, W. (2010). Vocal–respiratory interactions in the parabrachial nucleus. In Handbook of Behavioral Neuroscience (Elsevier), pp. 383-392.

Stujenske, J.M., Spellman, T., and Gordon, J.A. (2015). Modeling the spatiotemporal dynamics of light and heat propagation for in vivo optogenetics. Cell. Rep. *12*, 525-534.

Sugihara, G., May, R., Ye, H., Hsieh, C.-h., Deyle, E., Fogarty, M., and Munch, S. (2012). Detecting Causality in Complex Ecosystems. Science *338*, 496-500.

Sugihara, G., and May, R.M. (1990). Nonlinear forecasting as a way of distinguishing chaos from measurement error in time series. Nature *344*, 734-741.

Tan, W., Pagliardini, S., Yang, P., Janczewski, W.A., and Feldman, J.L. (2010). Projections of preBötzinger complex neurons in adult rats. J. Comp. Neurol. *518*, 1862-1878.

Vaccarino, A.L., and Melzack, R. (1989). Analgesia produced by injection of lidocaine into the anterior cingulum bundle of the rat. Pain *39*, 213-219.

Varga, A.G., Reid, B.T., Kieffer, B.L., and Levitt, E.S. (2020). Differential impact of two critical respiratory centres in opioid-induced respiratory depression in awake mice. J. Physiol. *598*, 189-205.

Wang, D., He, X., Zhao, Z., Feng, Q., Lin, R., Sun, Y., Ding, T., Xu, F., Luo, M., and Zhan, C. (2015). Whole-brain mapping of the direct inputs and axonal projections of POMC and AgRP neurons. Front. Neuroanat. *9*, 40.

Wang, S.C., Ngai, S.H., and Frumin, M.J. (1957). Organization of central respiratory mechanisms in the brain stem of the cat: genesis of normal respiratory rhythmicity. Am. J. Physiol. *190*, 333-342.

Whitney, H. (1936). The imbedding of manifolds in families of analytic manifolds. Ann. Math., 865-878.

Yang, C.F., Kim, E.J., Callaway, E.M., and Feldman, J.L. (2020). Monosynaptic projections to excitatory and inhibitory preBötzinger complex neurons. Front. Neuroanat. *14*, 58.

Yokota, S., Kaur, S., VanderHorst, V.G., Saper, C.B., and Chamberlin, N.L. (2015). Respiratory-related outputs of glutamatergic, hypercapnia-responsive parabrachial neurons in mice. J. Comp. Neurol. *523*, 907-920.

Zhang, F., Wang, L.-P., Brauner, M., Liewald, J.F., Kay, K., Watzke, N., Wood, P.G., Bamberg, E., Nagel, G., and Gottschalk, A. (2007). Multimodal fast optical interrogation of neural circuitry. Nature *446*, 633-639.

Figure 2.1. PBL^{Oprm1} activity synchronizes with breathing

(A) Schematic of the simultaneous recording of breathing and neural activity.

(B) Schematic and histology of jGCaMP7s expression in PBL^{Oprm1} neurons. Scale, 200 μm.

(C) 20-s example traces of breathing sensor voltage (top) and PBL^{Oprm1} activity (bottom) illustrating their tight correlation. Scale, 2 sec.

(D) 20-min example traces of the raw voltage trace, plethysmograph amplitude, breathing rate, and PBL^{Oprm1} calcium signals (top to bottom) showing their tight correlation. Asterisks indicate sighing events.

(E and G) Strong correlation between calcium signals and plethysmograph amplitude (E) and breathing rate (G) (n = 4).

(F and H) PBL^{Oprm1} activities synchronized with plethysmograph amplitude (F) and breathing rate (H) during major respiratory bouts.

(I and J) PBL^{Oprm1} activities predicted breathing rate (I) and vice versa (J) as shown by convergent cross-mapping (CCM) analysis.

(K) CCM model using calcium signal to predict breathing rate performed better than the reverse model across different training sample sizes. Data are presented as mean ± SEM**.** See also Figure S2.1.

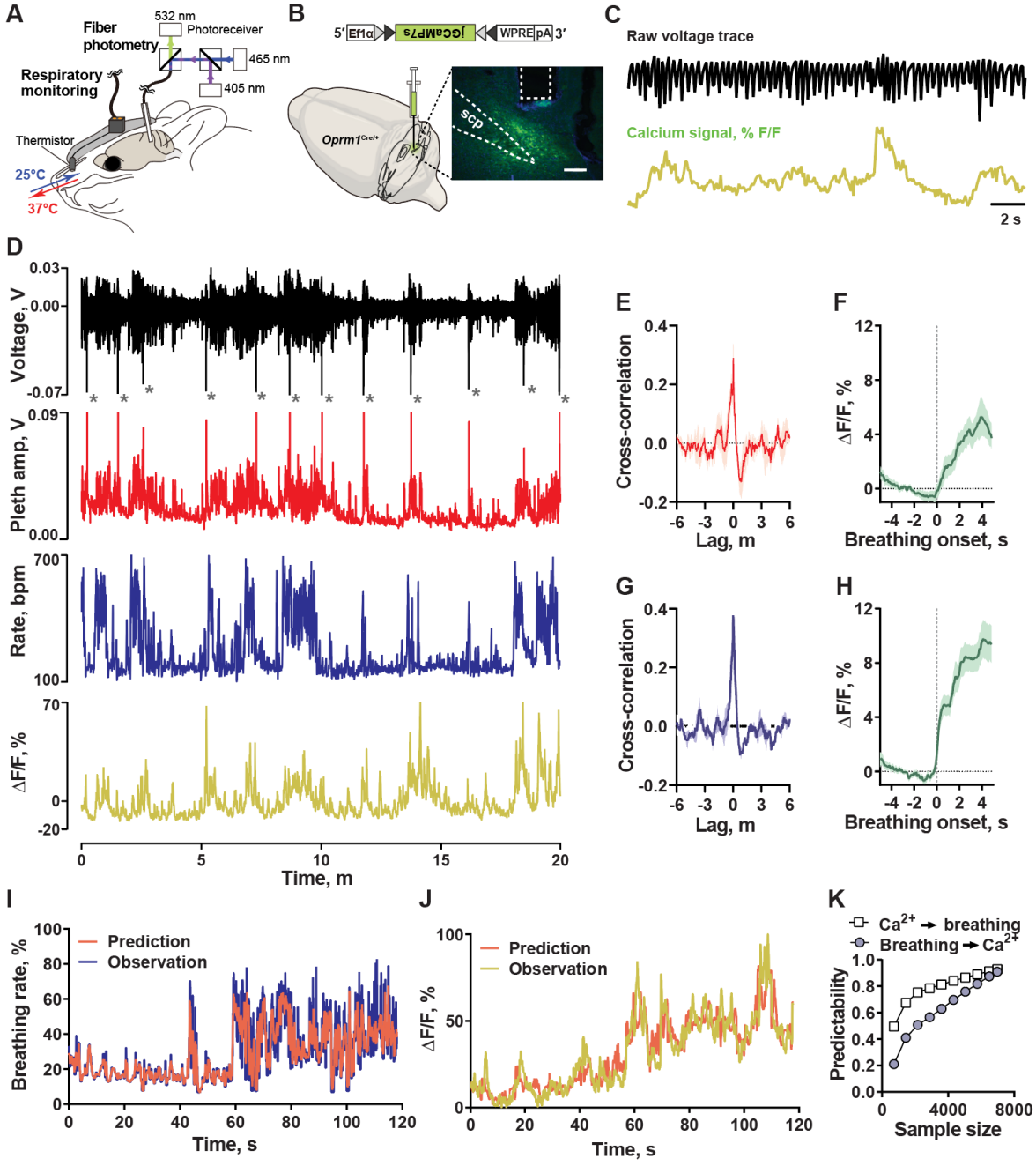
A
Fiber photometry
532 nm
Photoreceiver
465 nm
405 nm
Respiratory monitoring
Thermistor
25°C
37°C
B
5′ Ef1α jGCaMP7s WPRE pA 3′
Oprm1Cre/+
scp
C
Raw voltage trace
Calcium signal, % F/F
2 s
D
Voltage, V
Pleth amp, V
Rate, bpm
ΔF/F, %
Time, m
E
Cross-correlation
Lag, m
F
ΔF/F, %
Breathing onset, s
G
Cross-correlation
Lag, m
H
ΔF/F, %
Breathing onset, s
I
Prediction
Observation
Breathing rate, %
Time, s
J
Prediction
Observation
ΔF/F, %
Time, s
K
Ca2+ → breathing
Breathing → Ca2+
Predictability
Sample size

Figure 2.2. PBL^{Oprm1} neurons regulate breathing rate

(A) Schematic of the use of whole-body plethysmography (WBP) to monitor breathing in awake mice with chemogenetic manipulation.

(B) Schematic and histology of hM3Dq and hM4Di expression in PBL^{Oprm1} neurons. Scale, 200 μm.

(C and E) CNO injection (5 mg/kg i.p.) significantly increased breathing rate in hM3Dq-expressing mice (n = 9) and decreased breathing rate in hM4Di-expressing mice (n = 12), but did not affect eYFP controls (n = 7 for C and n = 9 for E).

(D and F) Representative breathing traces after systemic injection of saline or CNO in hM3Dq (D) or hM4Di (F)-expressing mice and eYFP controls. Scale, 1 sec.

(G) Schematic of the use of inductance plethysmography to monitor breathing in anesthetized mice with optogenetic manipulation.

(H) Schematic and histology of ChR2 and ArchT expression in PBL^{Oprm1} neurons. Scale, 200 μm.

(I) Activating PBL^{Oprm1} neurons via ChR2 significantly increased breathing rate (n = 8) while inhibiting PBL^{Oprm1} neurons via ArchT significantly decreased breathing rate (n = 8). These effects were not observed in controls (n = 8 for I and n = 7 for K).

(J) Representative traces of voltage, breathing rate (range 52.3–201.9 bpm), and plethysmograph amplitude (range 4.3–12.7 mV) during optogenetic stimulation (blue shade, 10 s).

(L) Representative traces of voltage, breathing rate (range 84.5–122.6 bpm), and plethysmograph amplitude (range 6.6–8.6 mV) during optogenetic inhibition (yellow shade, 5 s).

(M and O) Representative traces depicting frequency-dependent photostimulation effects (M) or intensity-dependent photoinhibition effects (O) on breathing rate. Scale, 100 bpm/5 sec (M) or 10 bpm/2 sec (O).

(N and P) Quantification of average breathing rate during the light-on period in M and O, normalized to pre-stimulation baseline (n = 4 for N and n = 3 for P).

Statistical analyses were performed using two-way ANOVA analysis with Bonferroni's multiple comparison post-hoc test (C, E, I, K), and one-way ANOVA with Tukey's post-hoc test, comparing each frequency with the no-stimulation control group (N and P), *, $p < 0.05$; **, $p < 0.01$; ***, $p < 0.001$; ****, $p < 0.0001$. Data are presented as mean ± SEM. See also Figure S2.2.

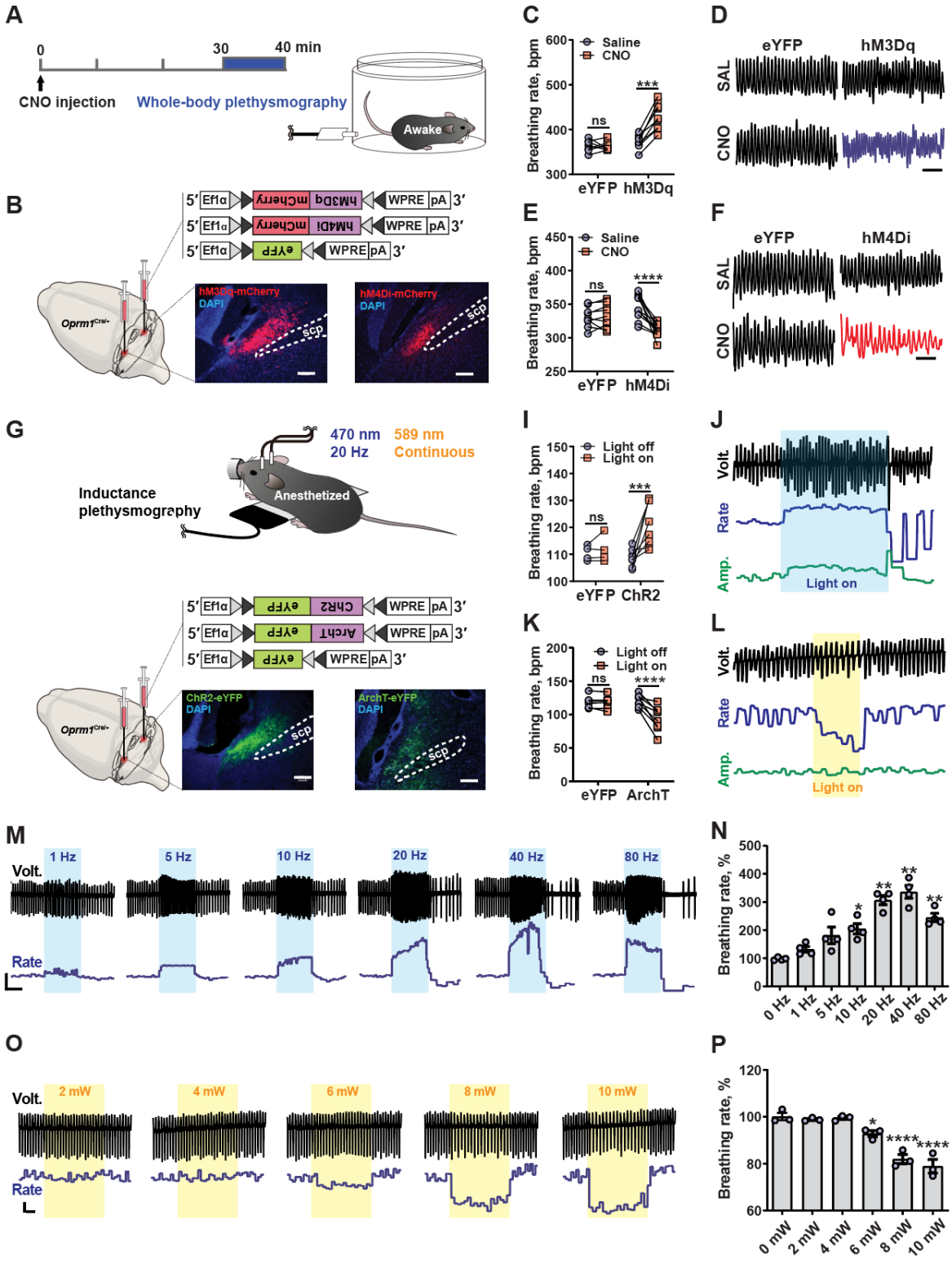
A
0
30
40 min
CNO injection
Whole-body plethysmography
Awake
B
5′ Efl1α hM3Dq mCherry WPRE pA 3′
5′ Efl1α hM4Di mCherry WPRE pA 3′
5′ Efl1α eYFP WPRE pA 3′
Oprm1Cre/+
hM3Dq-mCherry
DAPI
scp
hM4Di-mCherry
DAPI
scp
C
Saline
CNO
Breathing rate, bpm
ns
***
eYFP hM3Dq
D
eYFP
hM3Dq
SAL
CNO
E
Saline
CNO
Breathing rate, bpm
ns
****
eYFP hM4Di
F
eYFP
hM4Di
SAL
CNO
G
470 nm
20 Hz
589 nm
Continuous
Inductance plethysmography
Anesthetized
5′ Efl1α eYFP ChR2 WPRE pA 3′
5′ Efl1α eYFP ArchT WPRE pA 3′
5′ Efl1α eYFP WPRE pA 3′
Oprm1Cre/+
ChR2-eYFP
DAPI
scp
ArchT-eYFP
DAPI
scp
I
Light off
Light on
Breathing rate, bpm
ns
***
eYFP ChR2
J
Volt.
Rate
Amp.
Light on
K
Light off
Light on
Breathing rate, bpm
ns
****
eYFP ArchT
L
Volt.
Rate
Amp.
Light on
M
1 Hz
5 Hz
10 Hz
20 Hz
40 Hz
80 Hz
Volt.
Rate
N
Breathing rate, %
0 Hz
1 Hz
5 Hz
10 Hz
20 Hz
40 Hz
80 Hz
O
2 mW
4 mW
6 mW
8 mW
10 mW
Volt.
Rate
P
Breathing rate, %
0 mW
2 mW
4 mW
6 mW
8 mW
10 mW

Figure 2.3. Input-output mapping of PBL^{Oprm1} neural connections

(A) Schematic of monosynaptic retrograde tracing from PBL^{Oprm1} neurons and representative images of the starter region and upstream areas. SpV: spinal trigeminal nucleus; Spinal: spinal cord dorsal horn; CeA: central amygdalar nucleus; BNST: bed nuclei of the stria terminalis; SPFp: subparafascicular nucleus, parvicellular part; NTS: nucleus tractus solitarius; SC: superior colliculus; PSTN: parasubthalamic nucleus. Scale, 100 μm (spinal) or 200 μm (others).

(B) Quantification of the presynaptic inputs (n = 7). CN: cochlear nucleus; RN: reticular nucleus; VN: vestibular nucleus; SNr: substantia nigra, reticular part; PAG: periaqueductal gray; ZI: zona incerta; LHA: lateral hypothalamic area; PVH: paraventricular hypothalamic nucleus.

(C) Schematic and histology of nucleus-targeting tdTomato and axon-targeting synaptophysin:eGFP expression in PBL^{Oprm1} neurons.

(D) Coronal sections showing PBL^{Oprm1} axon terminals in the preBötC marked by SST immunohistochemistry. Arrowheads and asterisks denoted SST^{+} and SST^{-} preBötC neurons that receive PBL^{Oprm1} inputs. Scale, 200 μm (10 x) or 10 μm (60 x).

(E and G) Clozapine injection into preBötC increased breathing rate in hM3Dq-expressing animals (n = 7) but not in eYFP-expressing animals (n = 6). Representative traces are shown in panel G. Two-way ANOVA analysis with Bonferroni's multiple comparison post-hoc test, *, $p < 0.05$. ****, $p < 0.0001$.

(F) Schematic of chemogenetic terminal stimulation of hM3Dq-expressing PBL^{Oprm1} neurons by stereotaxic injection of clozapine (CLZ, 200 nl, 1 μg/ml) into preBötC of anesthetized mice. Data are presented as mean ± SEM. See also Figure S2.3.

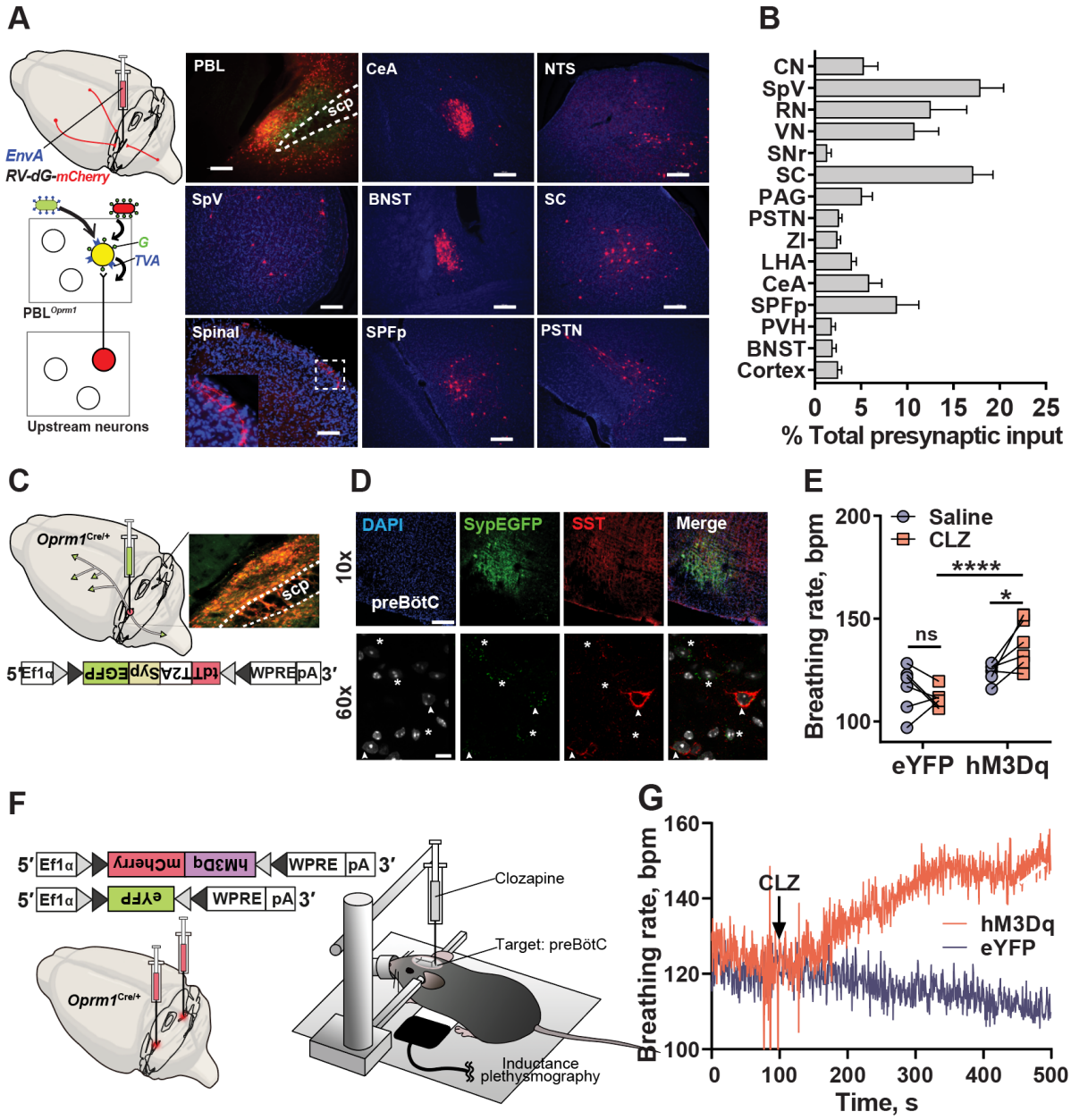
A
EnvA
RV-dG-mCherry
G
TVA
PBL Oprm1
Upstream neurons
PBL
CeA
NTS
SpV
BNST
SC
Spinal
SPFp
PSTN
scp
B
CN
SpV
RN
VN
SNr
SC
PAG
PSTN
ZI
LHA
CeA
SPFp
PVH
BNST
Cortex
0 5 10 15 20 25
% Total presynaptic input
C
Oprm1Cre/+
scp
5′ Ef1α tdTTZASypEGFP WPRE pA 3′
D
DAPI
SypEGFP
SST
Merge
10x
60x
preBötC
E
Saline
CLZ
****
*
ns
Breathing rate, bpm
200
150
100
eYFP hM3Dq
F
5′ Ef1α hM3Dq mCherry WPRE pA 3′
5′ Ef1α eYFP WPRE pA 3′
Oprm1Cre/+
Clozapine
Target: preBötC
Inductance plethysmography
G
CLZ
hM3Dq
eYFP
Breathing rate, bpm
160
140
120
100
0 100 200 300 400 500
Time, s

Figure 2.4. PBL^{Oprm1} neurons are recruited during pain-induced hyperventilation

(A and F) Schematic of simultaneous monitoring of PBL^{Oprm1} activity and breathing rate in anesthetized mice during noxious thermal (55 ^{o}C hot rod, A) and mechanical (tail pinch with 300 g pressure, F) stimulation.

(B, D, G, and I) Average traces of normalized breathing rate (B, G) and PBL^{Oprm1} activity (D, I) before and after applying thermal (B, D) and mechanical (G, I) noxious or control stimuli (thermal control: a room-temperature rod; mechanical control: gentle touch) (grey shade) (B, D: n = 14–17 traces from 7 mice; G, I: n = 15–18 traces from 7 mice). Scale, 2 s/10 bpm (B), 2 s/2% ΔF/F (D), 1 s/10 bpm (G), 1 s/2% ΔF/F (I).

(C, E, H, and J) Thermal (Therm) or mechanical (Mech) stimulation significantly increased the area under the curve (AUCs) of the breathing rate (C, H) and calcium activity (E, J) compared to control (Con) stimulation.

(K and L) Schematic and representative traces of simultaneous monitoring of PBL^{Oprm1} activity and breathing rate in freely moving mice during noxious thermal stimulus presentation (grey shade depicts changing the temperature from 25 to 55°C).

(M and N) Thermal pain increased AUCs of breathing rate (M) and calcium (N) traces compared to baseline (n = 7).

(O) Breathing rate and calcium signals displayed strong cross-correlation during thermal pain stimulation (n = 7).

(P) Schematic of inhibiting PBL^{Oprm1} neurons during thermal and mechanical stimulation.

(Q and R) Inhibiting PBL^{Oprm1} neurons by ArchT attenuated hyperventilation evoked by thermal (Q) and mechanical pain signals (R) (n = 13 stimulations from 3 mice), which was not observed in the eYFP group (n = 9 stimulations from 3 mice).

Statistics analyses were performed using two-way ANOVA analysis with Bonferroni's multiple comparison post-hoc test (Q, R), two-tailed unpaired t-test (C, E, H, J), and two-tailed paired t-test (M, N). Ns, not significant; *, $p < 0.05$; ***, $p < 0.001$; ****; $p < 0.0001$. Data are presented as mean ± SEM. See also Figure S2.4.

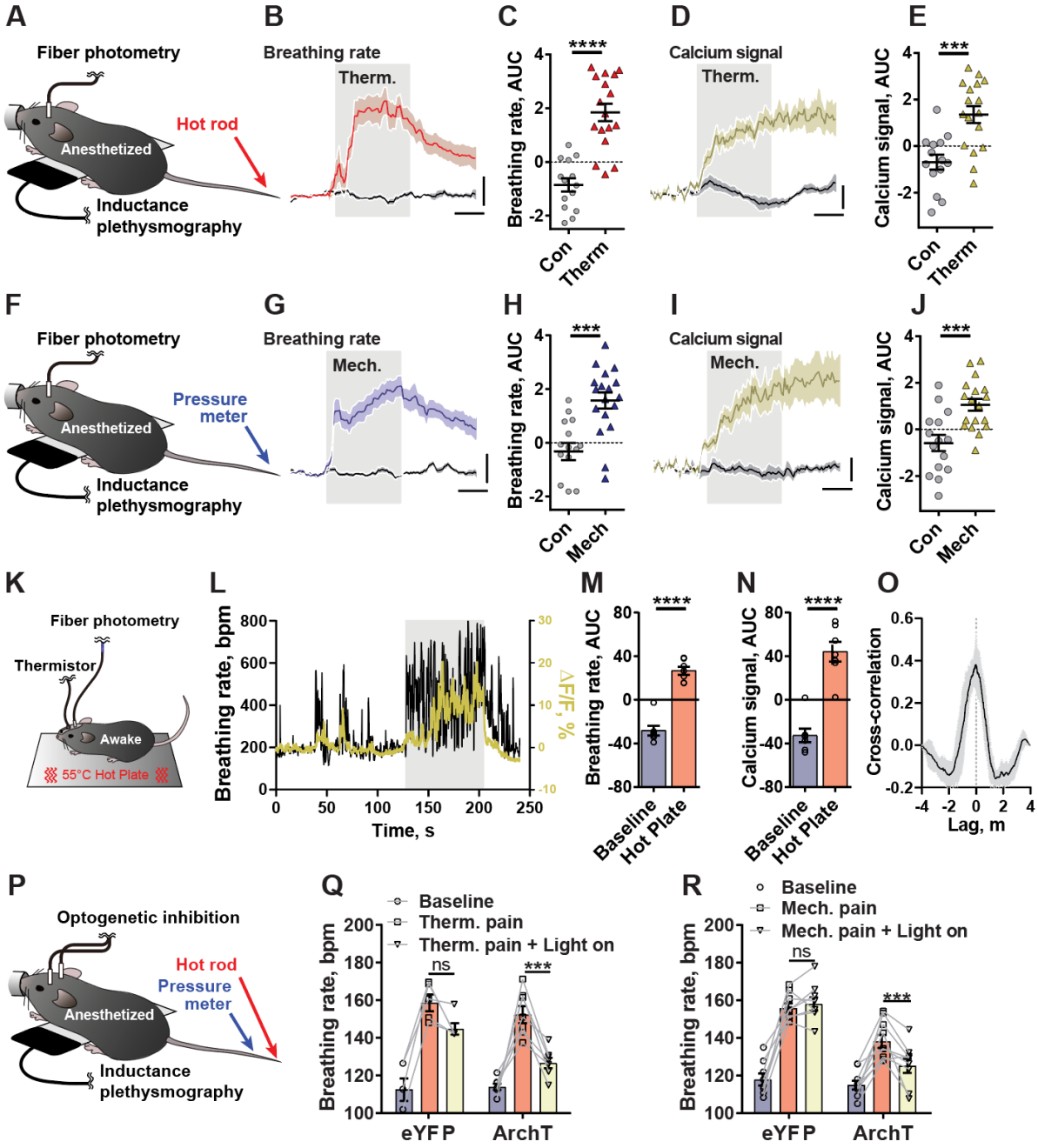
A
Fiber photometry
Anesthetized
Hot rod
Inductance plethysmography
B
Breathing rate
Therm.
C
Breathing rate, AUC
****
Con
Therm
D
Calcium signal
Therm.
E
Calcium signal, AUC
***
Con
Therm
F
Fiber photometry
Anesthetized
Pressure meter
Inductance plethysmography
G
Breathing rate
Mech.
H
Breathing rate, AUC
***
Con
Mech
I
Calcium signal
Mech.
J
Calcium signal, AUC
***
Con
Mech
K
Fiber photometry
Thermistor
Awake
55°C Hot Plate
L
Breathing rate, bpm
ΔF/F, %
Time, s
M
Breathing rate, AUC
****
Baseline
Hot Plate
N
Calcium signal, AUC
****
Baseline
Hot Plate
O
Cross-correlation
Lag, m
P
Optogenetic inhibition
Anesthetized
Hot rod
Pressure meter
Inductance plethysmography
Q
Baseline
Therm. pain
Therm. pain + Light on
Breathing rate, bpm
ns
***
eYFP
ArchT
R
Baseline
Mech. pain
Mech. pain + Light on
Breathing rate, bpm
ns
***
eYFP
ArchT

Figure 2.5. PBL^{Oprm1} inhibition alleviates affective pain perception and attenuates anxiety-like behaviors

(A and D) Schematic of hot plate assay for testing thermal sensitivity and nocifensive behavior (A) and electronic von Frey assay for testing mechanical sensitivity (D).

(B and E) CNO injection (7.5 mg/kg i.p, same as below) did not result in differences in thermal (B) or mechanical (E) sensitivity in mice expressing hM4Di (n = 5) or eYFP (n = 7 for B, n = 5 for E) in PBL^{Oprm1} neurons.

(C) Mice expressing hM4Di (n = 5) in PBL^{Oprm1} neurons displayed a longer latency to jump when stimulated with a von Frey fiber after CNO injection compared to the eYFP group (n = 7).

(F) Schematic of formalin assay for chemical and inflammatory sensitivity test.

(G) CNO injection significantly reduced paw licking time in hM4Di group (n = 5) compared to eYFP controls (n = 7).

(H) Schematic of contextual fear conditioning test, in which CNO was injected before the conditioning session.

(I) CNO injection significantly decreased freezing behavior in the hM4Di group compared to the eYFP group during conditioning (five 0.2 mA, 2 s foot shocks, uneven inter-shock intervals) (n = 5 per group).

(J) CNO injection significantly decreased freezing behavior in the hM4Di group compared to eYFP controls during the contextual retrieval test 24 hr after conditioning (n = 5 per group).

(K) Schematic of elevated plus maze (EPM) assay for testing anxiety-like behavior.

(L) Heatmaps of averaged movement in each group during the EPM test. Arrow denotes open arm.

(M) The hM4Di group, but not the eYFP group, increased open arm time after CNO injection compared to saline injection (n = 7 per group).

(N and Q) Schematics of real-time place preference (RTPP, N) and avoidance (RTPA, Q) tests.

(O and R) Heatmaps of averaged movement in each group during RTPP (O) and RTPA (R) tests.

(P and S) Mice expressing ArchT in PBL^{Oprm1} neurons (n = 6) spent significantly more time in the “light-on” chamber compared to the eYFP group (n = 6, P), whereas mice expressing ChR2 (n = 8) spent significantly less time in the “light-on” chamber compared to the controls (n = 5, S).

Statistical analyses were performed using two-way ANOVA analysis with Bonferroni’s multiple comparison post-hoc test (G, I, J, M, P, S) or two-tailed unpaired t-test (B, C, E). Ns, not significant; *, $p < 0.05$; **, $p < 0.01$; ***, $p < 0.001$; ****, $p < 0.0001$. Data are presented as mean ± SEM. See also Figure S2.5.

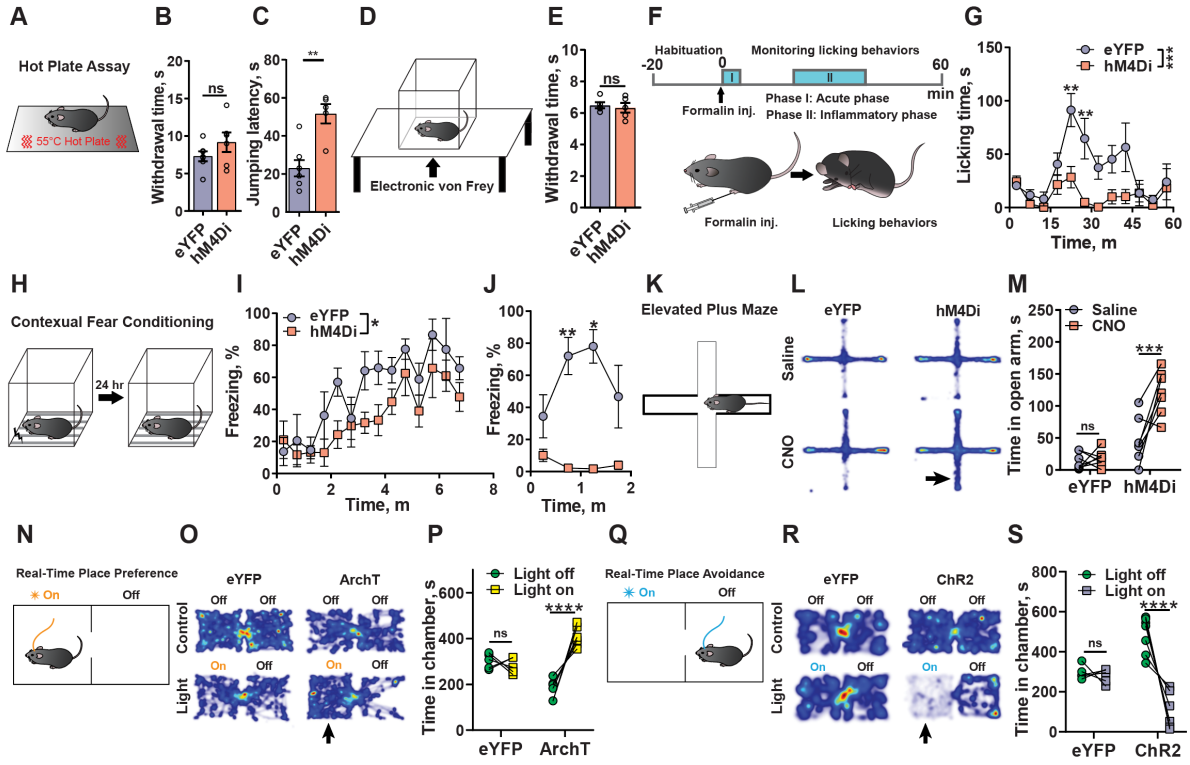
A
Hot Plate Assay
55°C Hot Plate
B
Withdrawal time, s
ns
eYFP
hM4Di
C
Jumping latency, s
**
D
Electronic von Frey
E
Withdrawal time, s
F
Habituation
Monitoring licking behaviors
-20
0
60
min
Formalin inj.
Phase I: Acute phase
Phase II: Inflammatory phase
Licking behaviors
G
Licking time, s
Time, m
H
Contexual Fear Conditioning
24 hr
I
Freezing, %
J
K
Elevated Plus Maze
L
Saline
CNO
M
Time in open arm, s
N
Real-Time Place Preference
On
Off
O
ArchT
Control
Light
P
Light off
Light on
Time in chamber, s
Q
Real-Time Place Avoidance
R
ChR2
S

Figure 2.6. Same PBL^{Oprm1} neurons regulate breathing and pain

(A) Schematic of simultaneous recording of breathing and calcium activity from single PBL^{Oprm1} neurons with a microendoscope. Tail pinching represents noxious stimuli. Scale, 500 μm (4 x) / 200 μm (10 x) / 100 μm (ROI).

(B) Example trace of the breathing rate (top) and heatmaps of individual neuronal activities (bottom) demonstrating their synchronization. Scale, 100 bpm / 10 s.

(C) Heatmap of individual neuronal activities aligned at the onset of pinching (white line). Each row in panels B and C corresponds to the same neuron from one representative mouse.

(D) Pie chart showing the percentage of neurons that respond to breathing only (16/108), pain only (23/108), both (67/108), and neither (2/108, from 5 mice).

(E, F, and G) Example breathing rate and calcium traces (left) and averaged pinching response (right) for an example neuron that showed responses to both breathing and pinching (E), a breathing-only neuron (F), and a pain-only neuron (G). Scale, left panel: 200 bpm (top), 20 (E) / 3 (F) /1 (G) units of z-scored ΔF/F / 20 sec; right panel: 1 unit of z-scored ΔF/F / 5 sec. Data are presented as mean ± SEM. See also Figure S2.6.

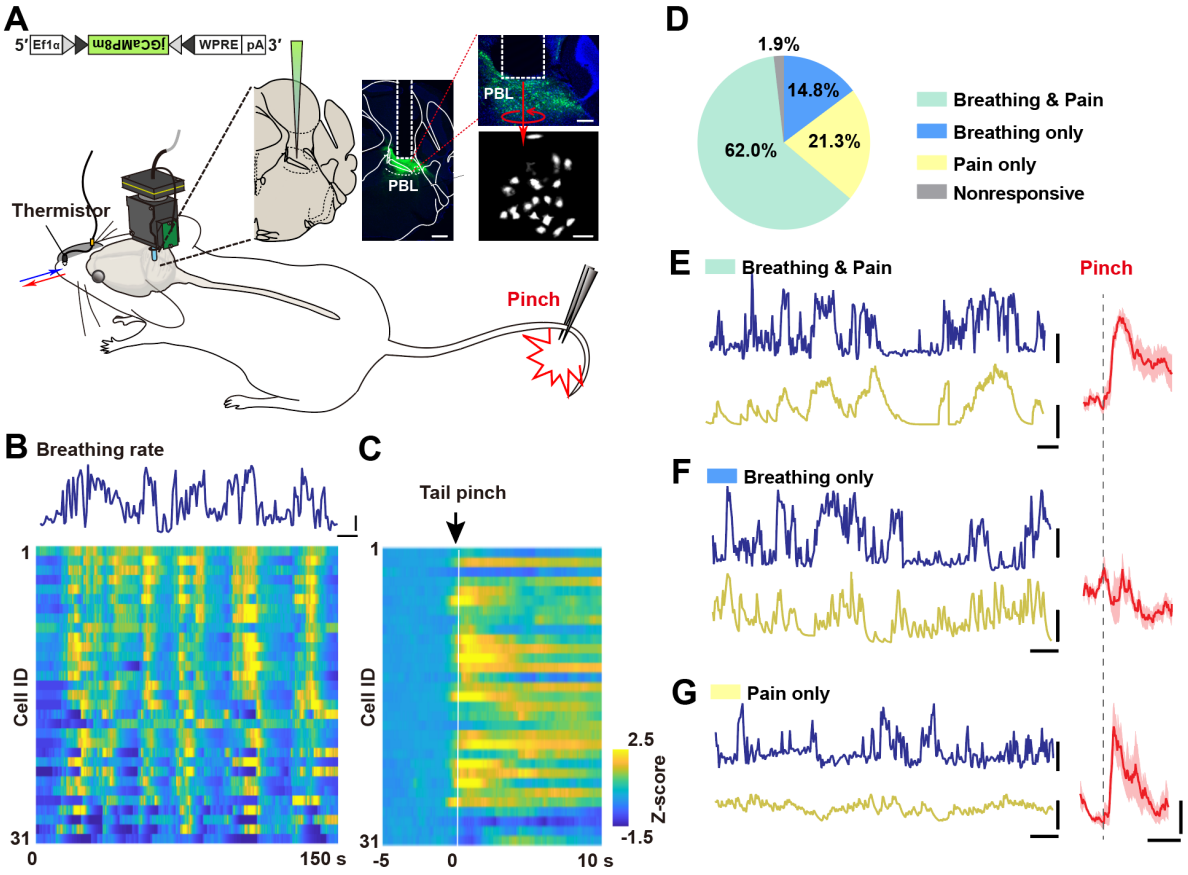
A
5′ Ef1α jGCaMP8m WPRE pA 3′
Thermistor
PBL
PBL
Pinch
B Breathing rate
Cell ID
1
31
0
150 s
C
Tail pinch
Cell ID
1
31
-5
0
10 s
2.5
-1.5
Z-score
D
1.9%
14.8%
21.3%
62.0%
Breathing & Pain
Breathing only
Pain only
Nonresponsive
E Breathing & Pain
Pinch
F Breathing only
G Pain only

Figure 2.7. PBL^{Oprm1} subpopulations projecting to the CeA and the preBötC form a “Core-Shell” pattern, and are differently involved in breathing regulation

(A) Schematic of projection-specific retrograde labeling strategy.

(B) Representative images of preBötC-projecting (eYFP-expressing, green, “shell”) and CeA-projecting PBL^{Oprm1} neurons (mCherry-expressing, red, “core”).

(C) Quantification of labeled core and shell neurons and their overlap (n = 5 animals). One-way ANOVA analysis with Tukey’s multiple comparison post-hoc test. *, $p < 0.05$. **, $p < 0.01$.

(D and I) Viral strategy for subpopulation-specific activity monitoring of shell (D) and core (I) neurons.

(E and J) Both shell (E) and core (J) neurons displayed activities tightly correlated with breathing. Calcium signal ranges, shell: -4.1% to 20.6%; core: -7.7% to 41.7%.

(F and K) Both shell (F) and core (K) activities strongly correlated with breathing rate (n = 4).

(G and L) Both shell (G) and core (L) activities and breathing rate were increased by nociceptive thermal stimulation (n = 15–21 trials from 5–7 animals for each group).

(H and M) Activities from shell neurons (H), but not core (M) neurons, tightly correlated with breathing during rearing-sniffing events (n = 25–35 trials from 3 mice for each group). Data are presented as mean ± SEM. See also Figure S2.7.

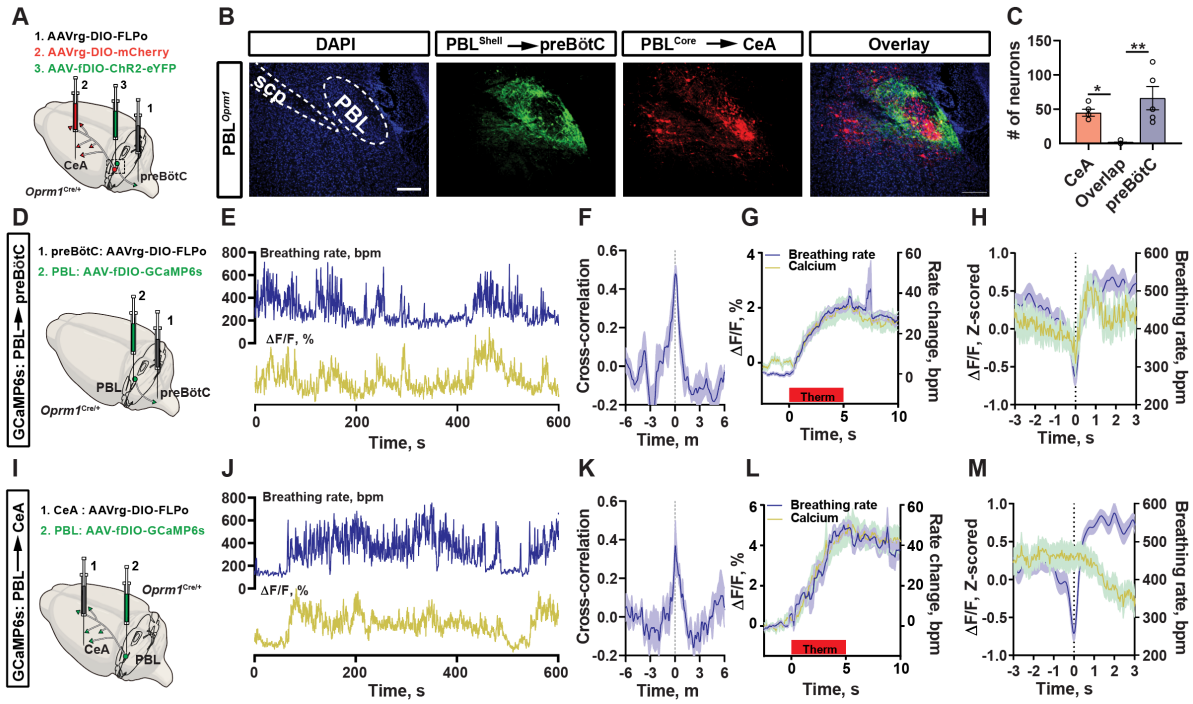
A
1. AAVrg-DIO-FLPo
2. AAVrg-DIO-mCherry
3. AAV-fDIO-ChR2-eYFP
CeA
preBötC
Oprm1Cre/+
B
DAPI
PBLShell → preBötC
PBLCore → CeA
Overlay
PBLOprm1
scp
PBL
C
# of neurons
CeA
Overlap
preBötC
D
GCaMP6s: PBL→preBötC
1. preBötC: AAVrg-DIO-FLPo
2. PBL: AAV-fDIO-GCaMP6s
PBL
preBötC
Oprm1Cre/+
E
Breathing rate, bpm
ΔF/F, %
Time, s
F
Cross-correlation
Time, m
G
Breathing rate
Calcium
ΔF/F, %
Rate change, bpm
Therm
Time, s
H
ΔF/F, Z-scored
Breathing rate, bpm
Time, s
I
GCaMP6s: PBL→CeA
1. CeA : AAVrg-DIO-FLPo
2. PBL: AAV-fDIO-GCaMP6s
CeA
PBL
Oprm1Cre/+
J
Breathing rate, bpm
ΔF/F, %
Time, s
K
Cross-correlation
Time, m
L
Breathing rate
Calcium
ΔF/F, %
Rate change, bpm
Therm
Time, s
M
ΔF/F, Z-scored
Breathing rate, bpm
Time, s

Figure 2.8. PBL^{Oprm1} subpopulations differentially regulate breathing and pain

(A and F) Schematic of projection-specific optogenetic activation of core (A) and shell (F) subpopulations.

(B–E and G–J) Upon light stimulation, animals expressing ChR2 in core (B–E) and shell (G–J) neurons increased breathing rate (B and G), completed more jumps during the hot plate test (C and H), spent less time in the light-paired chamber in the RTPA test (D and I), and spent less time in the open arm of the EPM (E and J) compared with eYFP controls (core: ChR2/eYFP, n = 6/6; shell: ChR2/eYFP, n = 5/7).

(K and P) Schematic for projection-specific chemogenetic inhibition of the core (K) and shell (P) subpopulations.

(L–O) Upon CNO injection (5 mg/kg i.p.), animals expressing hM4Di in core neurons decreased breathing rate (L), decreased licking time in the formalin assay (M), increased latency to the first jump in the hot plate test (N), and increased time spent in the open arm of the EPM (O) compared to the eYFP controls (hM4Di/eYFP, n = 7/7).

(Q–T) Upon CNO injection, animals expressing hM4Di in shell neurons decreased breathing rate (Q), but did not change licking time in the formalin assay (R), latency to the first jump in the hot plate test (S), or time spent in the open arm of the EPM (T) compared to the eYFP controls (hM4Di/eYFP, n = 8/7).

(U) Schematic for projection-specific electrophysiology. Whole-cell patch-clamp recording was performed with one subpopulation expressing mCherry, while blue light was delivered to stimulate the other subpopulation expressing ChR2 under the control of retrogradely transported FLPo.

(V and X) Example EPSC traces in shell (V) and core (X) neurons evoked by 2-ms blue light stimulation of the other subpopulation, before and after CNQX application. Scale, 20 ms/20 pA (V and X-upper); 10 ms/20 pA (X-lower).

(W and Y) Percentage of shell (W, n = 14) and core (Y, n = 15) neurons displaying light-evoked EPSC responses.

(Z) Summary of the inter- and extra- PBL^{Oprm1} circuits that collectively regulate breathing, pain, and anxiety.

Statistical analyses were performed using two-way ANOVA analysis with Bonferroni's multiple comparison post-hoc test (B, D, G, I, L, M, Q, R) or two-tailed unpaired t-test (C, E, H, J, N, O, S, T). Ns, not significant; *, $p < 0.05$; **, $p < 0.01$; ****, $p < 0.0001$. Data are presented as mean ± SEM. See also Figure S2.8.

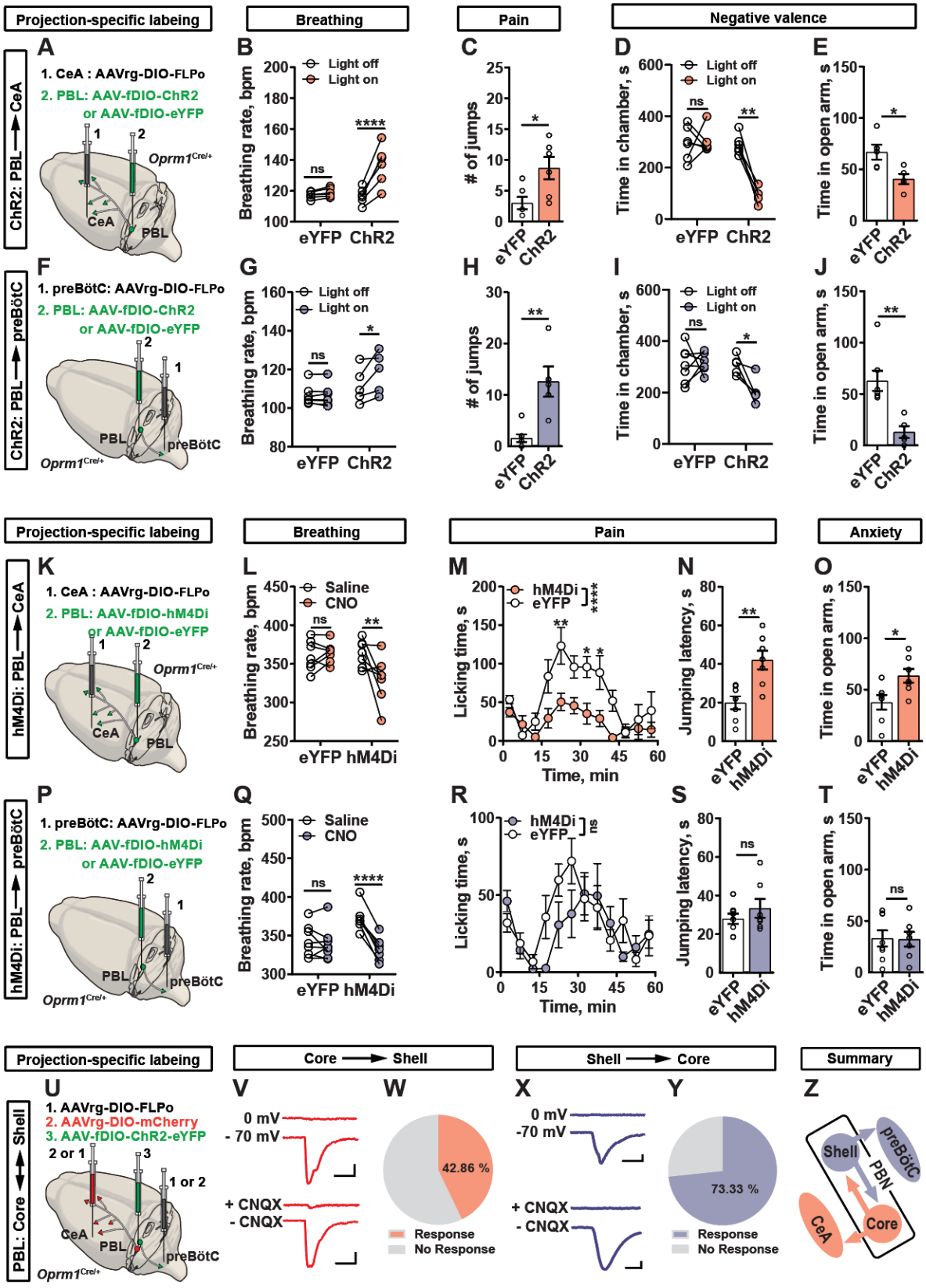
Projection-specific labeling
Breathing
Pain
Negative valence
ChR2: PBL→CeA
A
1. CeA : AAVrg-DIO-FLPo
2. PBL: AAV-fDIO-ChR2
or AAV-fDIO-eYFP
Oprm1Cre/+
CeA
PBL
B
Light off
Light on
Breathing rate, bpm
ns
****
eYFP ChR2
C
# of jumps
*
D
Time in chamber, s
**
E
Time in open arm, s
ChR2: PBL→preBötC
F
1. preBötC: AAVrg-DIO-FLPo
2. PBL: AAV-fDIO-ChR2
or AAV-fDIO-eYFP
preBötC
G
H
I
J
Projection-specific labeling
Breathing
Pain
Anxiety
hM4Di: PBL→CeA
K
1. CeA : AAVrg-DIO-FLPo
2. PBL: AAV-fDIO-hM4Di
or AAV-fDIO-eYFP
L
Saline
CNO
eYFP hM4Di
M
hM4Di
eYFP
Licking time, s
Time, min
N
Jumping latency, s
O
hM4Di: PBL→preBötC
P
1. preBötC: AAVrg-DIO-FLPo
2. PBL: AAV-fDIO-hM4Di
or AAV-fDIO-eYFP
Q
R
S
T
Projection-specific labeling
Core → Shell
Shell → Core
Summary
PBL: Core→Shell
U
1. AAVrg-DIO-FLPo
2. AAVrg-DIO-mCherry
3. AAV-fDIO-ChR2-eYFP
2 or 1
3
1 or 2
V
0 mV
- 70 mV
+ CNQX
- CNQX
W
42.86 %
Response
No Response
X
0 mV
-70 mV
+ CNQX
- CNQX
Y
73.33 %
Response
No Response
Z
Shell
preBötC
PBN
CeA
Core

Figure S2.1. Control experiments for establishing the correlation between PBL^{Oprm1} activity and breathing. Related to Figure 2.1

(A) Experimental setup to test whether breathing sensor affects normal breathing rhythm.

(B) No significant differences in baseline breathing rate were observed between thermistor-implanted (n = 5) and unimplanted mice (n = 5).

(C) Representative images depicting MOR immunohistochemistry on PBL sections expressing jGCaMP7s. Scale, 50 μm.

(D) Quantification of colocalization between jGCaMP7s$^+$ and MOR$^+$ cells. 94.9 ± 4.2% of jGCaMP7s$^+$ cells also express MOR.

(E) Example fiber photometry traces showing simultaneously recorded isosbestic and calcium-dependent signals from an animal expressing jGCaMP7s in PBL^{Oprm1} neurons.

(F) Example fiber photometry traces recorded from an animal expressing GFP in PBL^{Oprm1} neurons.

(G and H) Averaged breathing sensor voltage, plethysmograph amplitude, breathing rate, and PBL^{Oprm1} activity changes aligned to sighing onset (G, n = 24 events from 4 animals) and sniffing onset (H, n = 35 events from 5 animals).

(I and J) Example traces depicting breathing rate, calcium activity, and velocity from an animal expressing jGCaMP7s in PBL^{Oprm1} neurons (I) and GCaMP6f in the dorsal striatum (J).

(K) Strategy and histology of labelling parabrachial *Oprm1*-negative neurons with Cre-off GCaMP virus.

(L) Example traces depicting plethysmograph amplitude, breathing rate, and *Oprm1*-negative neuronal activity.

(M and N) Cross-correlation between non-*Oprm1* neuronal activity and plethysmograph amplitude (M) and breathing rate (N) (n = 3). See also Figures 1E and 1G for comparison with *Oprm1* neurons.

(O) Non-*Oprm1* responds robustly to pinching (as a positive control) (n = 15 trials from 3 mice).

Statistical analyses were performed using two-tailed unpaired t-test (B), ns, not significant. Data are presented as mean ± SEM.

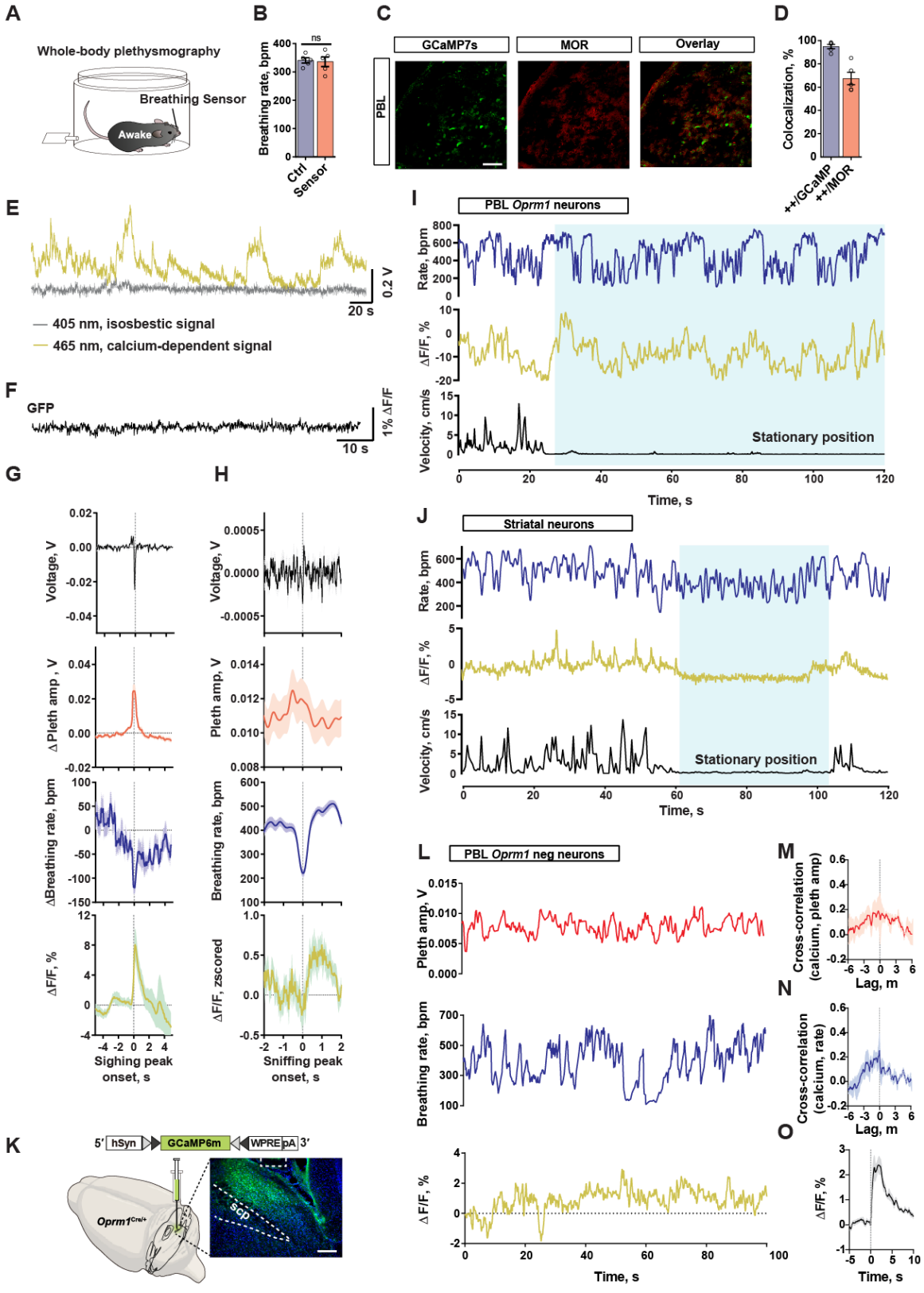
A
Whole-body plethysmography
Breathing Sensor
Awake
B
Breathing rate, bpm
ns
Ctrl
Sensor
C
GCaMP7s
MOR
Overlay
PBL
D
Colocalization, %
++/GCaMP
++/MOR
E
0.2 V
20 s
405 nm, isosbestic signal
465 nm, calcium-dependent signal
F
GFP
1% ΔF/F
10 s
G
Voltage, V
ΔPleth amp , V
ΔBreathing rate, bpm
ΔF/F, %
Sighing peak onset, s
H
Voltage, V
Pleth amp, V
Breathing rate, bpm
ΔF/F, zscored
Sniffing peak onset, s
I
PBL Oprm1 neurons
Rate, bpm
ΔF/F, %
Velocity, cm/s
Stationary position
Time, s
J
Striatal neurons
Rate, bpm
ΔF/F, %
Velocity, cm/s
Stationary position
Time, s
K
5′ hSyn GCaMP6m WPRE pA 3′
Oprm1Cre/+
scp
L
PBL Oprm1 neg neurons
Pleth amp, V
Breathing rate, bpm
ΔF/F, %
Time, s
M
Cross-correlation (calcium, pleth amp)
Lag, m
N
Cross-correlation (calcium, rate)
Lag, m
O
ΔF/F, %
Time, s

Figure S2.2. PBL^{Oprm1} manipulation alters breathing rhythm and pattern. Related to Figure 2.2

(A) CNO-induced firing rate increase in hM3Dq-expressing PBL^{Oprm1} neurons in *ex vivo* cell-attached recording. Scale, 20 sec.

(B and C) CNO injection significantly increased breathing rate in the hM3Dq group (n = 9) compared to eYFP controls (n = 7) (B), but no effects were observed in plethysmograph amplitude between groups (C). Breathing parameters were normalized to the saline-injected group.

(D and E) Both breathing rate (D) and amplitude (E) significantly increased by photostimulation in ChR2 group (n = 8) compared to eYFP controls (n = 8). Breathing parameters were normalized to the pre-stimulation baseline.

(F) 30-s representative traces depicting the changes in plethysmograph amplitude during photostimulation with various frequencies. Scale, 5 sec.

(G) CNO-induced hyperpolarization of hM4Di-expressing PBL^{Oprm1} neurons in *ex vivo* whole-cell patch-clamp recording. Traces depicting resting membrane potential (top) and firing patterns in response to 50 pA current injection (bottom) before and after CNO application. Scale, 2 mV / 20 sec (top); 20 mV / 20 ms (bottom).

(H and I) Breathing rate significantly decreased in CNO-injected mice expressing hM4Di in PBL^{Oprm1} neurons (n = 12) compared to eYFP controls (n = 12) (H). CNO injection significantly increased plethysmograph amplitude in hM4Di mice (n = 12) compared to controls (n = 9) (I). Breathing parameters were normalized to the saline-injected group.

(J and K) Breathing rate significantly decreased after photostimulation in mice expressing ArchT in PBL^{Oprm1} neurons (n = 8) compared to eYFP controls (n = 7) (J), but amplitude was not different between groups (K). Breathing parameters were normalized to the pre-stimulation baseline.

(L) 20-s representative traces depicting the changes in plethysmograph amplitude during photoinhibition with various intensities. Scale, 2 sec.

(M) Repeated photoinhibition (6-min trains) resulted in progressive inhibition of breathing rate and amplitude and led to apnea. Scale, 2 sec.

Statistical analyses were performed using two-tailed unpaired t-test, ns, not significant; *, $p < 0.05$; **, $p < 0.01$; ***, $p < 0.001$; ****, $p < 0.0001$. Data are presented as mean ± SEM.

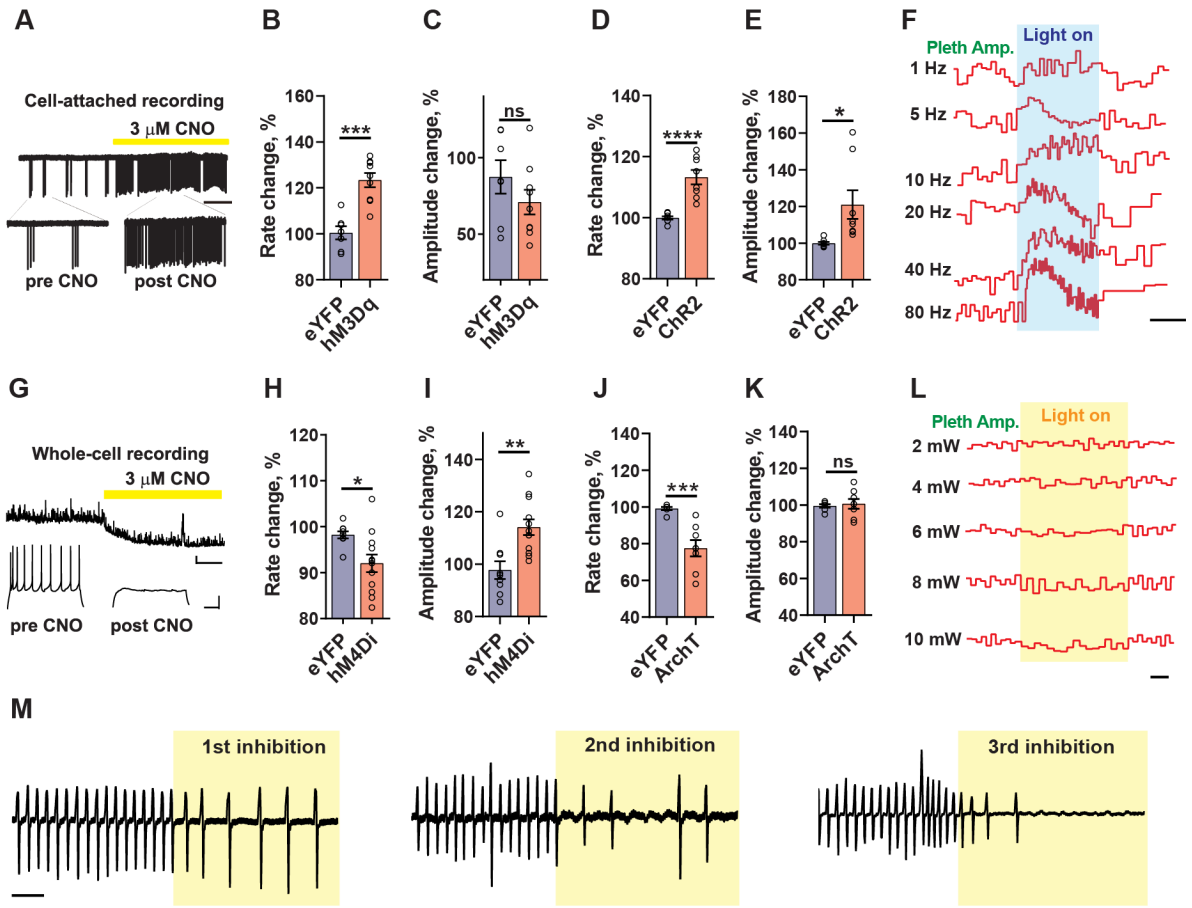
A
Cell-attached recording
3 μM CNO
pre CNO
post CNO
B
Rate change, %
***
eYFP
hM3Dq
C
Amplitude change, %
ns
eYFP
hM3Dq
D
Rate change, %
****
eYFP
ChR2
E
Amplitude change, %
*
eYFP
ChR2
F
Pleth Amp.
Light on
1 Hz
5 Hz
10 Hz
20 Hz
40 Hz
80 Hz
G
Whole-cell recording
3 μM CNO
pre CNO
post CNO
H
Rate change, %
*
eYFP
hM4Di
I
Amplitude change, %
**
eYFP
hM4Di
J
Rate change, %
***
eYFP
ArchT
K
Amplitude change, %
ns
eYFP
ArchT
L
Pleth Amp.
Light on
2 mW
4 mW
6 mW
8 mW
10 mW
M
1st inhibition
2nd inhibition
3rd inhibition

Figure S2.3. Input-output mapping of PBL^{Oprm1} neurons. Related to Figure 2.3

(A) Example images of the starter cells in the PBL with MOR immunohistochemistry. Scale, 10 μm.

(B) Example images showing the PBL region after injecting the same batch and volume of TVA-oG-GFP and RVdG-mCherry viruses into *Oprm1*$^{Cre/+}$ and wild-type mice. Scale, 100 μm.

(C) Illustration of the relative projection strength (% of total presynaptic projections) of each presynaptic region of PBL^{Oprm1} neurons (n = 7). Abbreviations follow those in the Figure 3B.

(D) Output mapping of PBL^{Oprm1} neurons by stereotaxic injection of AAV-DIO-ChR2-eYFP into the PBL of *Oprm1*$^{Cre/+}$ mice (top left panel) and visualization of the axon terminals in representative brain regions. Abbreviations: BNST: bed nuclei of the stria terminalis; MnPO: median preoptic nucleus; OVLT: organum vasculosum of the laminae terminalis; IC: insular cortex; CeA: central amygdala; PVT: paraventricular thalamus; ILN: intralaminar nucleus; PSTN: parasubthalamic nucleus; VPMpc: parvicellular portion of the ventroposteromedial nucleus of thalamus; PIL: posterior intralaminar complex of the thalamus; PAG: periaqueductal gray; VTA: ventral tegmental area; IPN: interpeduncular nucleus; RN: red nucleus; SNr: substantia nigra, reticular part; SNc: substantia nigra, compact part; PnC: caudal pontine reticular nucleus; RTN: retrotrapezoid nucleus; SPIV: spinal vestibular nucleus; NTS, nucleus tractus solitarius; preBötC: pre-Bötzinger complex; SpV: spinal trigeminal nucleus. Scale, 500 μm.

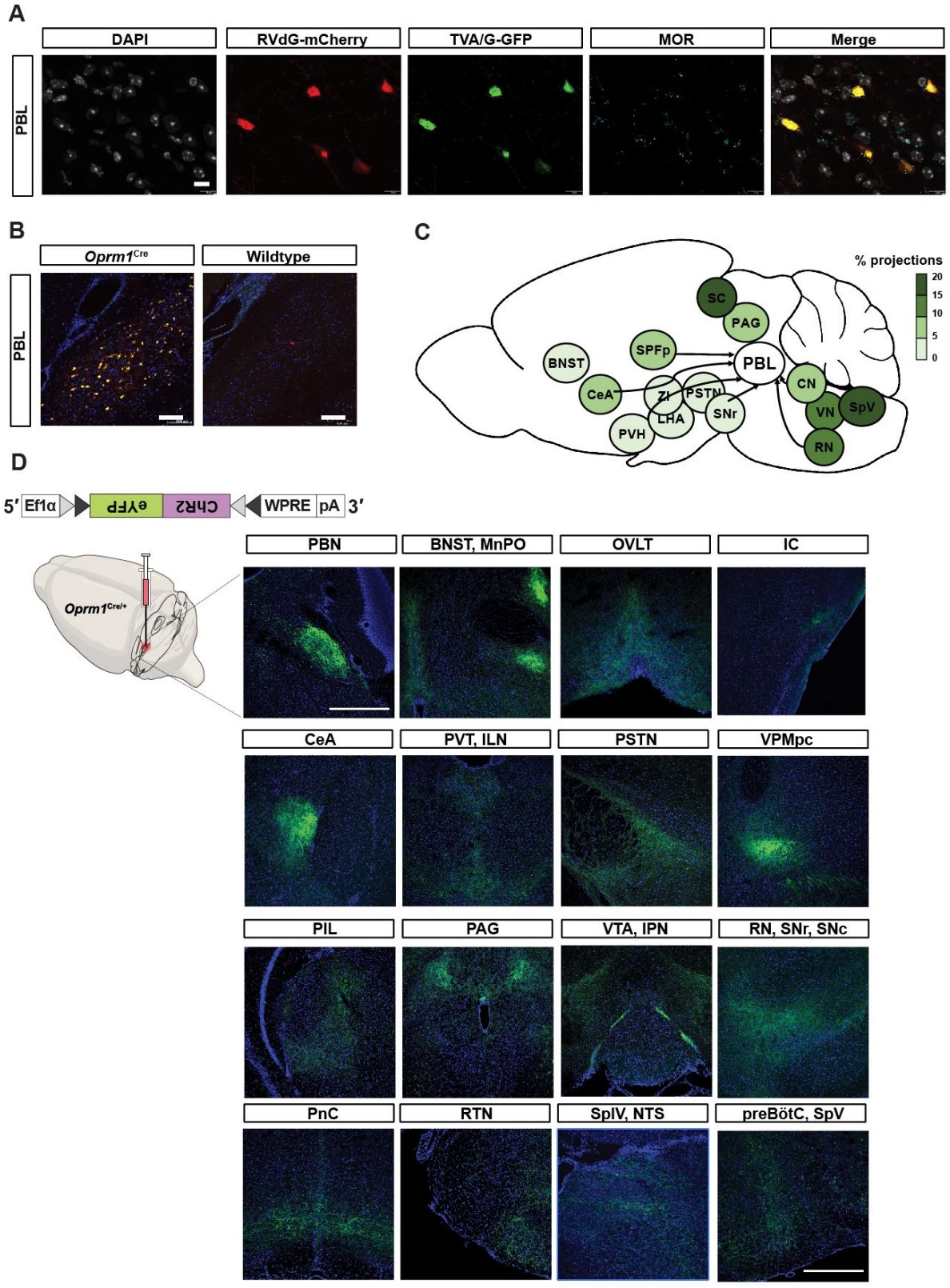
A
DAPI
RVdG-mCherry
TVA/G-GFP
MOR
Merge
PBL
B
Oprm1Cre
Wildtype
PBL
C
% projections
20
15
10
5
0
SC
PAG
SPFp
BNST
PBL
CN
CeA
ZI
PSTN
LHA
SNr
VN
SpV
PVH
RN
D
5′ Ef1α eYFP ChR2 WPRE pA 3′
Oprm1Cre/+
PBN
BNST, MnPO
OVLT
IC
CeA
PVT, ILN
PSTN
VPMpc
PIL
PAG
VTA, IPN
RN, SNr, SNc
PnC
RTN
SpIV, NTS
preBötC, SpV

Figure S2.4. Aversive stimuli induce different types of breathing changes, and PBL^{Oprm1} neuronal activity increases with pain-induced plethysmograph amplitude. Related to Figure 2.4

(A–C) Averaged breathing rate, plethysmograph amplitude, and velocity display distinct patterns when the following stimuli were presented to awake mice with different baseline breathing rates: (A) mild foot shocks (0.04 mA) with low basal breathing rate; (B) strong foot shocks that can induce fear memory (0.2 mA) with low basal breathing rate; (C) strong foot shocks (0.2 mA) with high basal breathing rate in actively moving mice. 2-s foot shocks are denoted in pink shades.

(D) Example traces showing breathing rate and amplitude changes during the EPM test.

(E) Breathing rate (E) but not amplitude (not shown) increased when animals approached the open arm and decreased when animals retreated from the open arm.

(F) Example traces showing breathing rate and amplitude changes when animals were placed on an elevated circular platform compared to baseline.

(G, H) Breathing rate (G) and amplitude (H) increased when animals were on the elevated platform compared to baseline.

(I) Representative traces of plethysmograph amplitude changes upon stimulation (grey shade) with a hot rod (noxious thermal stimulus; red trace) and a room-temperature rod (neutral control stimulus; grey trace). A significant increase was observed only upon stimulation with a hot rod. Scale, 1 s/1 mV.

(J) AUC of the plethysmograph amplitude traces during control (Con) and noxious thermal (Therm) rod stimulations (n = 14–17 stimulations from 7 mice).

(K) Representative traces of plethysmograph amplitude changes upon stimulation (grey shade) by tail pinches of 300 g (noxious mechanical stimulus; blue trace; measured by the pressuremeter) and 0 g (neutral control stimulus; grey trace) of pressure. A significant increase was observed only following 300 g tail pinches. Scale, 1 s/1 mV.

(L) AUC of plethysmograph amplitude traces during control (Con) and noxious mechanical stimulations (Mech) (n = 15–18 stimulations from 7 mice).

(M) Representative traces of plethysmograph amplitude and PBL^{Oprm1} calcium changes illustrating increases in both measures upon stimulation with thermal pain (grey).

(N) AUC analysis of plethysmograph amplitude during baseline and hot plate stimulation in awake animals (n = 7 trials from 7 mice).

(O) Respiratory plethysmograph amplitude and calcium signals displayed strong cross-correlation before and during thermal pain stimulation in awake animals (n = 7). Data are presented as mean ± SEM.

Statistical analyses were performed using two-tailed paired t-test (G, H, N) or two-tailed unpaired t-test (J, L), ns, not significant; *, $p < 0.05$; **, $p < 0.01$; ****, $p < 0.0001$. Data are presented as mean ± SEM.

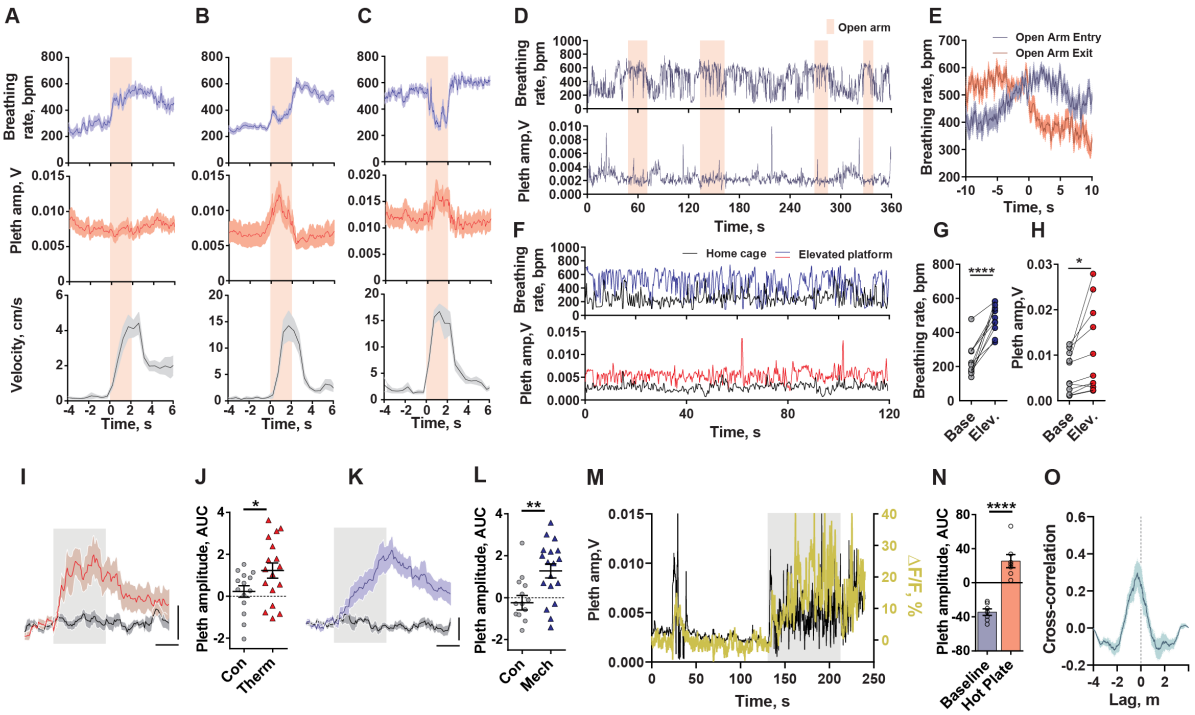
A
B
C
D
E
F
G
H
I
J
K
L
M
N
O
Breathing rate, bpm
Pleth amp, V
Velocity, cm/s
Time, s
Open arm
Pleth amp,V
Open Arm Entry
Open Arm Exit
Home cage
Elevated platform
Base
Elev.
****
*
Pleth amplitude, AUC
Con
Therm
**
Mech
ΔF/F, %
Baseline
Hot Plate
Cross-correlation
Lag, m

Figure S2.5. Chemogenetic inhibition of PBL^{Oprm1} neurons decreases affective pain responses and anxiety-like behaviors. Related to Figure 2.5

(A–E) During the formalin test, chemogenetic inhibition (7.5 mg/kg CNO) of PBL^{Oprm1} neurons did not alter licking time (A) or licking episodes (C, D) in hM4Di-expressing animals (n = 5) compared to eYFP controls (n = 7) during the acute phase, but significantly reduced licking time (B) and licking episodes (C, E) in these animals during the inflammatory phase.

(F, G) Mice expressing hM4Di visited the open arm of the Elevated Plus Maze more frequently (F) and traveled a longer distance (G) when injected with CNO (7.5 mg/kg) compared to saline, whereas the eYFP-expressing control group showed no significant differences following CNO versus saline injection (n = 7 per group).

Statistical analyses were performed using two-way ANOVA with Bonferroni's multiple comparison post-hoc test (C, F, G) or two-tailed unpaired t-test (A, B, D, E), ns, not significant; *, $p < 0.05$; **, $p < 0.01$; ****, $p < 0.0001$. Data are presented as mean ± SEM.

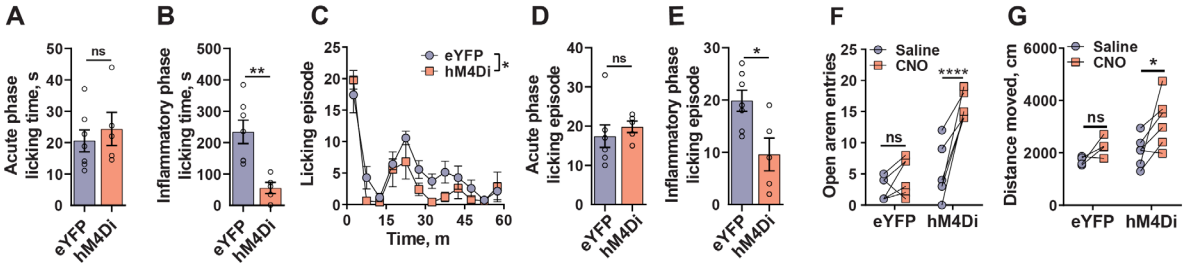
A
Acute phase licking time, s
ns
eYFP
hM4Di
B
Inflammatory phase licking time, s
**
C
Licking episode
eYFP
hM4Di
*
Time, m
D
Acute phase licking episode
E
Inflammatory phase licking episode
F
Open arem entries
Saline
CNO
****
G
Distance moved, cm

Figure S2.6. Molecular characterization of PBL^{Oprm1} neurons. Related to Figure 2.6

(A) Representative RNAscope image of PBel or PBdl that best demonstrates the colocalization of *Oprm1* (green) and several marker genes (*Calca*, *Tac1*, *Nts*, *Htr2a*, *FoxP2*, *Pdyn*, and *Tacr1,* red). Inset, magnified view showing representative neurons that express one or both marker genes. Scale, 100 μm (full) or 10 μm (inset).

(B) Quantification of colocalization between *Oprm1* and each of the candidate marker genes (n = 5–6 animals for each pair; all fluorescent cells from a 600 μm x 600 μm field of view were quantified, n = *Calca*: 1870; *Tac1*: 1437; *Nts*: 245; *Htr2a*: 886; *FoxP2*: 253; *Pdyn*: 360; *Tacr1*: 673).

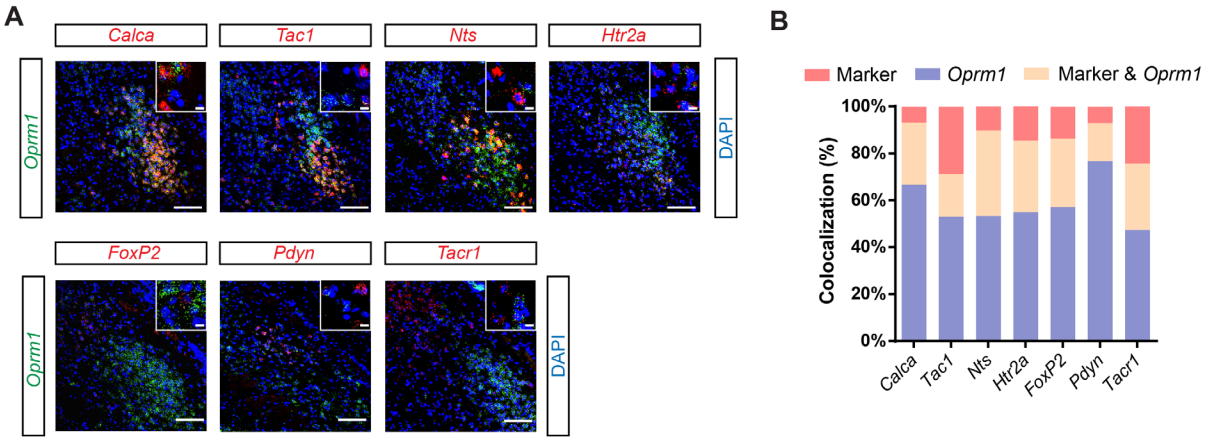
A
Calca
Tac1
Nts
Htr2a
Oprm1
DAPI
FoxP2
Pdyn
Tacr1
Oprm1
DAPI
B
Marker
Oprm1
Marker & Oprm1
Colocalization (%)
100%
80%
60%
40%
20%
0%
Calca
Tac1
Nts
Htr2a
FoxP2
Pdyn
Tacr1

Figure S2.7. Projection mapping and activity monitoring for PBL^{Oprm1} subpopulations. Related to Figure 2.7

(A, B) Schematic diagrams and representative images of subpopulation-specific labeling of PBL^{Oprm1} neurons that project to the CeA (A) and the preBötC (B).

(C, D) Core and shell subpopulations displayed different projection patterns to the forebrain/midbrain (C) and the hindbrain (D). Abbreviations defined in Figure S3D. Scale, 500 μm.

(E, L) Example traces of plethysmograph amplitude and *Oprm1*$^{PBL\rightarrow preBötC}$ (E) and *Oprm1*$^{PBL\rightarrow CeA}$ (L) calcium signals from 10-min recordings. Calcium signal ranges, *Oprm1*$^{PBL\rightarrow preBötC}$: -4.1% to 20.6%; *Oprm1*$^{PBL\rightarrow CeA}$: -7.7% to 41.7%.

(F, M) Cross-correlation between plethysmograph amplitude and *Oprm1*$^{PBL\rightarrow preBötC}$ (F) and *Oprm1*$^{PBL\rightarrow CeA}$ (M) calcium activities (n = 4 animals).

(G, H, N, O) For both *Oprm1*$^{PBL\rightarrow preBötC}$ (G, H) and *Oprm1*$^{PBL\rightarrow CeA}$ (N, O) neurons, areas under the curves (AUCs) of the breathing rate (G, N) and calcium (H, O) traces were significantly larger during noxious thermal stimulation (Therm), than during non-noxious control stimulation (Con).

(I, P) Averaged traces of change in breathing rate and *Oprm1*$^{PBL\rightarrow preBötC}$ (I) and *Oprm1*$^{PBL\rightarrow CeA}$ (P) calcium activity upon noxious mechanical stimulation.

(J, K, Q, R) For both *Oprm1*$^{PBL\rightarrow preBötC}$ (J, K) and *Oprm1*$^{PBL\rightarrow CeA}$ (Q, R) neurons, AUCs of breathing rate (J, Q) and calcium (K, R) traces were significantly larger during noxious mechanical stimulation (Mech) than during non-noxious control stimulation (Con). N = 15–21 stimulations from 5–7 mice.

Statistical analyses were performed using two-tailed unpaired t-tests (G, H, J, K, N, O, Q, R), **, $p < 0.01$; ***, $p < 0.001$; ****, $p < 0.0001$. Data are presented as mean ± SEM.

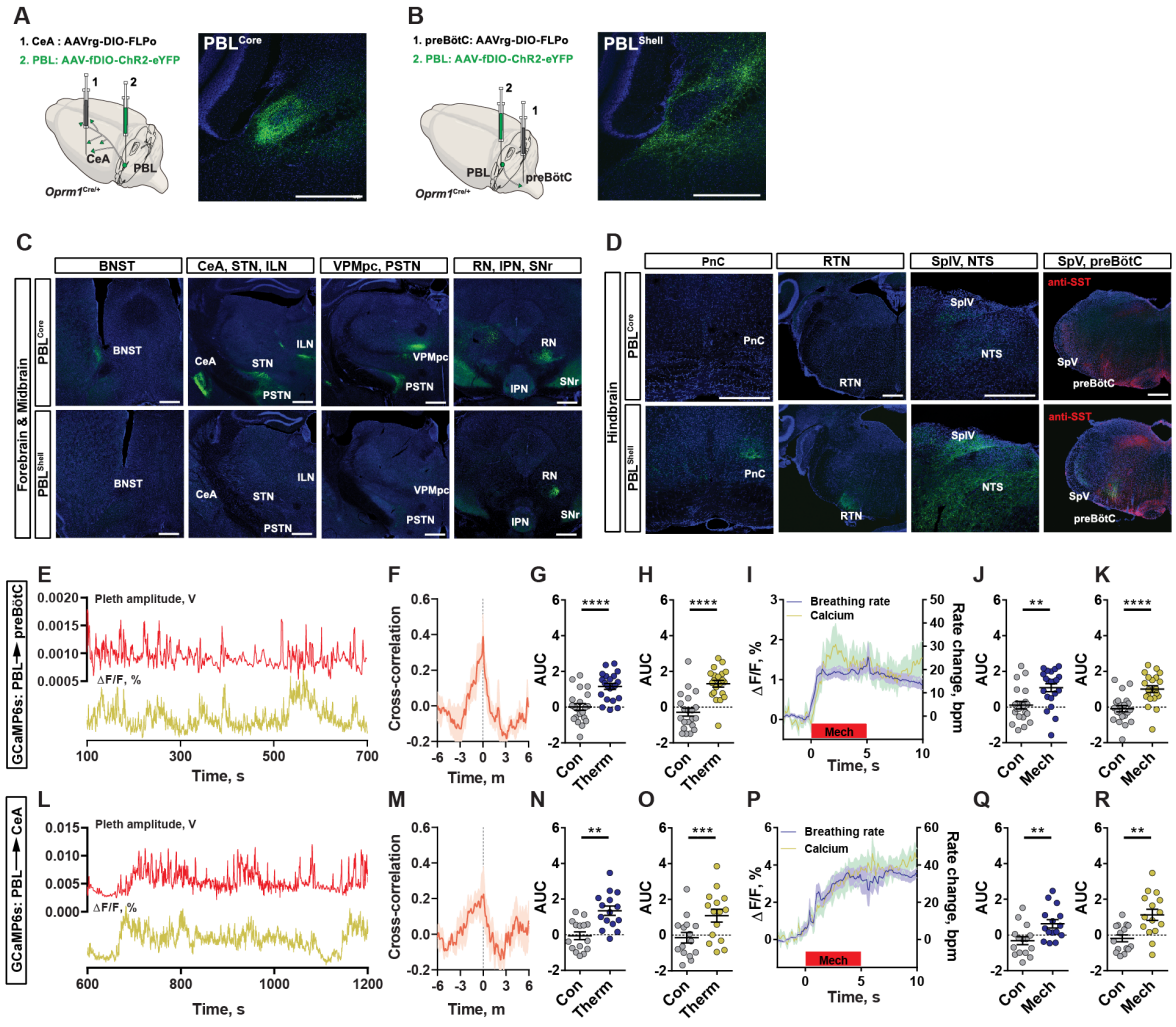
A
1. CeA : AAVrg-DIO-FLPo
2. PBL: AAV-fDIO-ChR2-eYFP
CeA
PBL
Oprm1Cre/+
PBLCore
B
1. preBötC: AAVrg-DIO-FLPo
2. PBL: AAV-fDIO-ChR2-eYFP
PBL
preBötC
Oprm1Cre/+
PBLShell
C
BNST
CeA, STN, ILN
VPMpc, PSTN
RN, IPN, SNr
Forebrain & Midbrain
PBLCore
PBLShell
BNST
CeA
STN
ILN
PSTN
VPMpc
RN
IPN
SNr
D
PnC
RTN
SpIV, NTS
SpV, preBötC
Hindbrain
PBLCore
PBLShell
PnC
RTN
SpIV
NTS
SpV
preBötC
anti-SST
E
GCaMP6s: PBL→preBötC
Pleth amplitude, V
ΔF/F, %
Time, s
F
Cross-correlation
Time, m
G
AUC
Con
Therm
****
H
AUC
Con
Therm
****
I
Breathing rate
Calcium
ΔF/F, %
Rate change, bpm
Mech
Time, s
J
AUC
Con
Mech
**
K
AUC
Con
Mech
****
L
GCaMP6s: PBL→CeA
Pleth amplitude, V
ΔF/F, %
Time, s
M
Cross-correlation
Time, m
N
AUC
Con
Therm
**
O
AUC
Con
Therm
***
P
Breathing rate
Calcium
ΔF/F, %
Rate change, bpm
Mech
Time, s
Q
AUC
Con
Mech
**
R
AUC
Con
Mech
**

Figure S2.8. Effects of manipulating PBL^{Oprm1} subpopulations in pain and negative emotion behavioral assays. Related to Figure 2.8

(A–C, E–G) In the optogenetics formalin assay, animals were administered photostimulation after 1% formalin injection to the hind paw. Animals expressing ChR2 in the *Oprm1*$^{PBL→CeA}$ (A–C) and *Oprm1*$^{PBL→preBötC}$ (E–G) neurons displayed more licking episodes compared to the eYFP-expressing control group during the inflammatory phase (C, G), but not the acute phase (B, F). (ChR2/eYFP: *Oprm1*$^{PBL→CeA}$: n = 6/6; *Oprm1*$^{PBL→preBötC}$: n = 10/8).

(D, H) Animals expressing ChR2 in *Oprm1*$^{PBL→CeA}$ (D) and *Oprm1*$^{PBL→preBötC}$ (H) neurons displayed robust freezing behaviors during repeated photostimulation compared to the eYFP-expressing control group (ChR2/eYFP: *Oprm1*$^{PBL→CeA}$: n = 6/6; *Oprm1*$^{PBL→preBötC}$: n = 5/7).

(I–M, P–T) Following CNO injection (5 mg/kg, same for below), animals expressing hM4Di in *Oprm1*$^{PBL→CeA}$ (I–M) neurons displayed fewer licking episodes and less licking time compared to the control group during the inflammatory phase of the formalin assay (I, K, M), but not during the acute phase (J, L). No differences were observed between animals expressing hM4Di in *Oprm1*$^{PBL→preBötC}$ neurons and controls (P–T).

(N, O, U, V) Animals expressing hM4Di in *Oprm1*$^{PBL→CeA}$ neurons (N, O), but not *Oprm1*$^{PBL→preBötC}$ neurons (U, V), displayed increased center time (N) and more center entries (O) in the open field assay after CNO injection compared to the eYFP-expressing control group (hM4Di/eYFP: *Oprm1*$^{PBL→CeA}$: n = 7/7; *Oprm1*$^{PBL→preBötC}$: n = 8/7).

(W) Schematic diagram of breathing monitoring during formalin-induced pain in animals with *Oprm1*$^{PBL→preBötC}$ neuronal inhibition.

(X) During the acute phase of the formalin test, no differences in breathing changes were observed between animals expressing hM4Di in *Oprm1*$^{PBL→preBötC}$ neurons and control animals.

(Y) During the inflammatory phase of the formalin test, animals expressing hM4Di in the *Oprm1*$^{PBL→preBötC}$ neurons displayed a significant reduction in breathing rate changes compared to control animals.

(Z) Summary of the role of divergent PBL^{Oprm1} circuits originating from the core and shell subpopulations (created using BioRender).

Statistical analyses were performed using two-way ANOVA with Bonferroni's multiple comparison post-hoc test (A, E, I, P) or two-tailed unpaired t-test (B–D, F–H, J–O, Q–V, X–Y), ns, not significant; *, $p < 0.05$; **, $p < 0.01$; ***, $p < 0.001$. Data are presented as mean ± SEM.

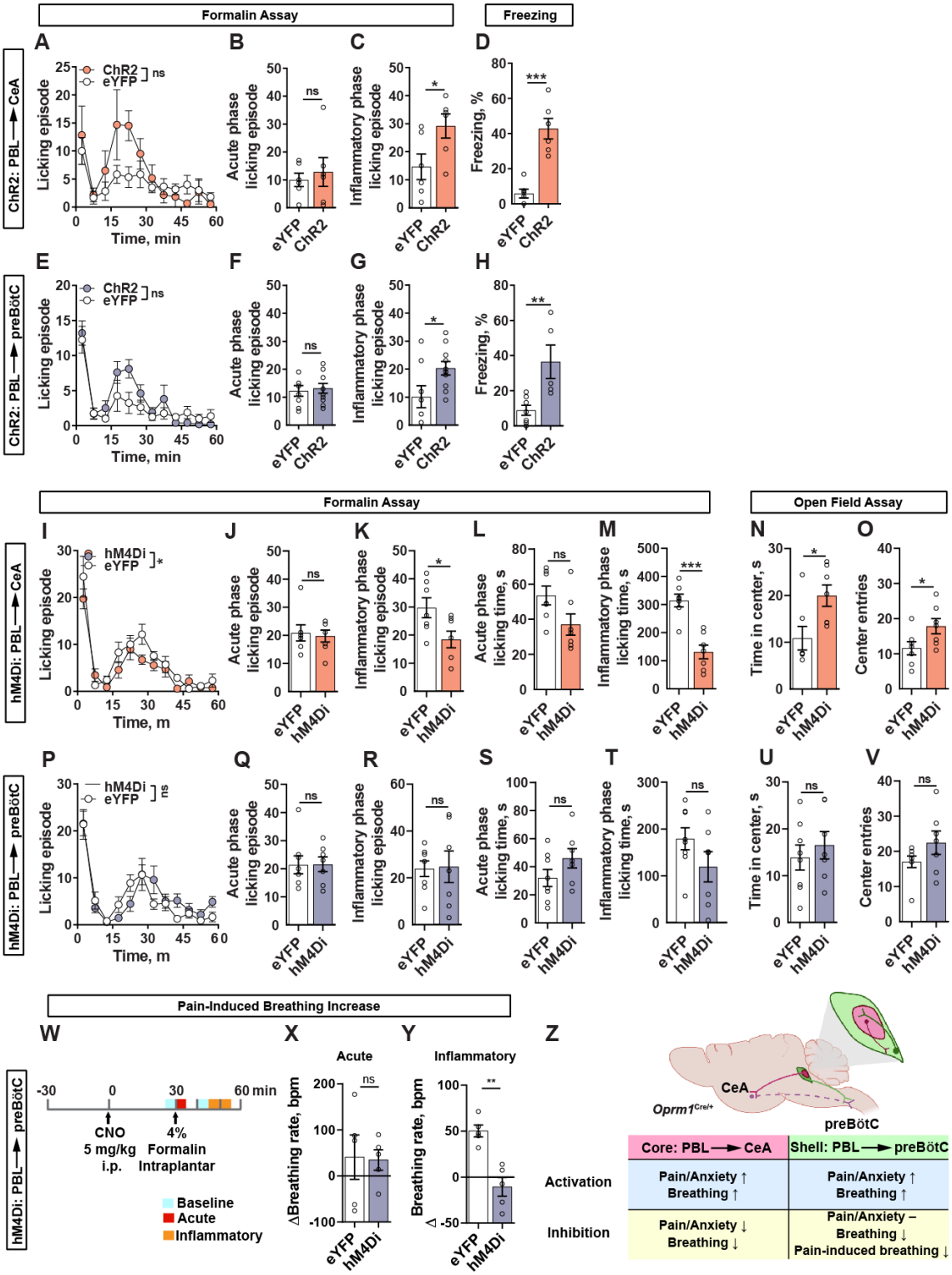
Formalin Assay
Freezing
ChR2: PBL → CeA
ChR2: PBL → preBötC
hM4Di: PBL → CeA
hM4Di: PBL → preBötC
Open Field Assay
Pain-Induced Breathing Increase
Licking episode
Time, min
Time, m
Acute phase licking episode
Inflammatory phase licking episode
Freezing, %
Acute phase licking time, s
Inflammatory phase licking time, s
Time in center, s
Center entries
Breathing rate, bpm
Acute
Inflammatory
ChR2
eYFP
hM4Di
ns
-30
0
30
60 min
CNO
5 mg/kg
i.p.
4%
Formalin
Intraplantar
Baseline
Acute
Inflammatory
CeA
preBötC
Oprm1Cre/+
Core: PBL → CeA
Shell: PBL → preBötC
Activation
Inhibition
Pain/Anxiety ↑
Breathing ↑
Pain/Anxiety ↓
Breathing ↓
Pain/Anxiety –
Breathing ↓
Pain-induced breathing ↓

Chapter 3: Neural basis of opioid-induced respiratory depression and its rescue

3.1 Abstract

Opioid-induced respiratory depression (OIRD) causes death following an opioid overdose, yet the neurobiological mechanisms of this process are not well understood. Here, we show that neurons within the lateral parabrachial nucleus that express the μ-opioid receptor (PBL^{Oprm1} neurons) are involved in OIRD pathogenesis. PBL^{Oprm1} neuronal activity is tightly correlated with respiratory rate, and this correlation is abolished following morphine injection. Chemogenetic inactivation of PBL^{Oprm1} neurons mimics OIRD in mice, whereas their chemogenetic activation following morphine injection rescues respiratory rhythms to baseline levels. We identified several excitatory G-protein coupled receptors expressed by PBL^{Oprm1} neurons and show that agonists for these receptors restore breathing rates in mice experiencing OIRD. Thus, PBL^{Oprm1} neurons are critical for OIRD pathogenesis, providing a promising therapeutic target for treating OIRD in patients.

3.2 Introduction

The misuse of prescription and recreational opioids has taken nearly 4.5 million lives between 1999 and 2018 in the United States alone (Hedegaard et al., 2020). The direct cause of death from opioid overdose is opioid-induced respiratory depression (OIRD) (Dahan et al., 2010; Pattinson, 2008). Currently, the only available antidote capable of reversing OIRD is naloxone, a nonselective opioid receptor antagonist. However, naloxone is associated with several disadvantages, namely the reappearance of OIRD due to its short half-life, the inability to reverse high-affinity opioid drugs (e.g., carfentanil and buprenorphine) due to its low binding affinity, and the potential to induce a catecholamine surge at high doses, which can cause cardiopulmonary arrest (Boyer, 2012; Dahan et al., 2018; Skolnick, 2018). Alternative non-opioid interventions are also promising candidates for rescuing OIRD (Dahan et al., 2018). These include potassium channel blockers that regulate the excitability

of carotid body cells (e.g. GAL-021) (Roozekrans et al., 2014), ampakines that activate the amino-3-hydroxy-5-methyl-D-aspartate (AMPA) receptors in the respiratory centers (e.g. CX717) (Oertel et al., 2010), and serotonin receptor agonists that activate the respiratory network (Manzke et al., 2003; Oertel et al., 2007). Among them, ampakines made the most progress in clinical trials (search of “opioids” and “respiratory depression” via clinicaltrials.gov in January 2021) (van der Schier et al., 2014). Although some of these alternatives are promising for OIRD rescue, the safety of these interventions has not been well documented. Therefore, novel treatment strategies are needed, and more effective countermeasures can only be developed with a mechanistic understanding of OIRD pathogenesis.

Neural substrates that contribute to OIRD pathogenesis should satisfy two criteria. They should localize to the breathing control network and express the μ-opioid receptor (MOR, encoded by the *Oprm1* gene), which has been demonstrated as the primary mediator of both the analgesic and respiratory effects of opioids (Dahan et al., 2001; Matthes et al., 1996). Two candidate structures satisfy these criteria, namely the pre-Bötzinger complex (preBötC) and the parabrachial complex (Bachmutsky et al., 2020; Cinelli et al., 2020; Lalley et al., 2014; Miller et al., 2017; Montandon and Horner, 2014; Montandon et al., 2011; Prkic et al., 2012; Varga et al., 2020; Wei and Ramirez, 2019). The former lies in the ventrolateral medulla and is the primary generator of the respiratory rhythm (Cui et al., 2016; Del Negro et al., 2018; Smith et al., 1991). The parabrachial complex, including the lateral parabrachial, medial parabrachial, and Kölliker-Fuse (KF) nuclei, is located in the dorsolateral pons and modulates breathing (Chamberlin and Saper, 1994; Dutschmann and Dick, 2012; Navarrete-Opazo et al., 2020), in response to homeostatic disturbances such as CO_2/O_2 imbalance and noxious stimuli (Jiang et al., 2004; Kaur et al., 2013; Kaur et al., 2017; Song and Poon, 2009a; b). Recent studies have suggested the involvement of these two brain regions on

OIRD pathogenesis by using either pharmacological or genetic approaches. Direct infusion of opioid agonists or antagonists into these brain areas induces or attenuates OIRD (Lalley, 2006; Miller et al., 2017; Prkic et al., 2012; Saunders and Levitt, 2020). Region-specific genetic deletion of the *Oprm1* genes by viral delivery of Cre-recombinase into these areas of the *Oprm1*-floxed mice also attenuates OIRD (Bachmutsky et al., 2020; Varga et al., 2020). However, the pharmacological approach lacks considerable specificity primarily due to the local diffusion of drugs and the difficulty of reproducible targeting, whereas the genetic deletion approach is often incomplete and prevents the possibility to directly control the neuronal activity in a spatially and temporally precise manner. As a result, discrepancies arise over the critical site of action responsible for OIRD (Bachmutsky et al., 2020; Lalley et al., 2014; Montandon and Horner, 2014; Varga et al., 2020). To expand the scope of current research, our paper utilizes contemporary cell-type-specific approaches to characterize the role of a defined neuronal population in morphine-induced respiratory depression. This will allow us to better understand its cellular and physiological mechanisms and make inroads in developing therapeutic strategies.

Here we report that a genetically defined population of neurons that encodes the *Oprm1* gene in the lateral parabrachial nucleus (PBL^{Oprm1} neurons) is an important regulator of respiratory rhythm. Inhibition of these neurons by opioids leads to respiratory depression. Furthermore, we show that both chemogenetic activation of these neurons and pharmacological activation of endogenous G-protein coupled receptors (GPCRs) expressed specifically in these neurons completely rescues OIRD in mice.

3.3 Materials and Methods

Mouse lines

The *Oprm1*$^{Cre:GFP}$ mouse line was generated from the lab of Dr. Richard Palmiter (see below). C57BL/6J (Stock No. 000664), *Oprm1*$^{fl/fl}$ (Stock No. 030074), RiboTag *Rpl22*$^{HA/HA}$ (Stock No. 011029) and Ai14 *Gt(ROSA)26Sor*$^{tm14(CAG-tdTomato)Hze}$ (Stock No. 007914) mouse lines were obtained from The Jackson Laboratory. Homozygous RiboTag and Ai14 mice were crossed with homozygous *Oprm1*^{Cre} mice for RiboTag and anatomy experiments, respectively. Both male and female mice were used in all studies. Animals were randomized to experimental groups, and no sex differences were noted. Mice were maintained on a 12-h light/dark cycle and provided with food and water *ad libitum*.

Generation of Oprm1^{Cre} mice

A cassette encoding Cre:GFP was inserted just 5’ of the initiation codon in the first coding exon of the *Oprm1* gene. The 5′ arm (~3.1 kb with *Pac*I and *Sal*I sites at 5’ and 3’ ends, respectively) and 3′ arm (~4.5 kb with *Xho*I and *Not*I sites at 5’ and 3’ ends, respectively) of *Oprm1* gene were amplified from a C57BL/6 BAC clone by PCR using Q5 Polymerase (New England Biolabs, USA) and cloned into polylinkers of a targeting construct that contained mnCre:GFP, a FRT-flanked Sv40Neo gene for positive selection, and HSV thymidine kinase and *Pgk*-diphtheria toxin A chain genes for negative selection. The mnCre:GFP cassette has a Myc-tag and nuclear localization signals at the N-terminus of Cre recombinase, which is fused to green fluorescent protein followed by a SV40 polyadenylation sequence. The construct was electroporated into G4 ES cells (C57BL/6 × 129 Sv hybrid), and correct targeting was determined by Southern blot of DNA digested with *Kpn*I using a ^{32}P-labeled probe downstream of the 3′ arm of the targeting construct. Twelve of the 84 clones analyzed were correctly targeted. One clone that was injected into blastocysts resulted in good chimeras that transmitted the targeted allele through the germline. Progeny were bred with *Gt(Rosa)26Sor-FLP* recombinase mice to remove the SV-Neo gene. Mice were then

continuously backcrossed to C57BL/6 mice. Routine genotyping is performed with three primers: 5’ CCT TCC ACT CAG AGA GTG GCG (*Oprm1* forward), 5’ CCT TCC ACT CAG AGA GTG GCG (*Oprm1* reverse), and 5’ GGC AAA TTT TGG TGT ACG GTC AG (Cre reverse). The wild type allele gives a band of ~500 bp, while the targeted allele provides a band with ~400 bp after 34 cycles with 20-s annealing at 60 °C.

Respiratory measurements

Inductance plethysmography

Inductance plethysmography was performed by placing a piezoelectric film beneath the chest of an anesthetized animal, which converts the chest movement into a voltage signal. The PowerLab system with LabChart 8 software (ADInstruments Inc., USA) was used for data acquisition, inspiratory and expiratory peak detection, and rate and amplitude calculation. Data were sampled at 100 or 400 Hz, low-pass filtered at 10 Hz, and smoothed with a 100-ms moving window. Automatic peak detection was validated with manual peak detection. Since the location of the sensor is subject to the slight movements of the animal’s body, the raw voltage value of the respiratory peak is less representative of the breathing amplitude.

Whole-body plethysmography (WBP)

A custom-built WBP chamber was utilized for measuring respiratory changes. The PowerLab system with LabChart 8 software was used for data acquisition, inspiratory and expiratory peak detection, and rate and amplitude calculation. Data were sampled at 1 kHz, band-pass filtered at 1–10 Hz, and smoothed with a 100-ms moving window. Automatic peak detection was validated with manual peak detection.

Micro thermistor-based plethysmography

A custom-built micro thermistor was implanted into the mouse nasal cavity to detect changes in temperature between inspiratory and expiratory airflow. The sensor was assembled using a Negative Temperature Coefficient (NTC) thermistor (TE Connectivity Ltd., Switzerland), an interconnector (Mill-Max Mfg. Corp., USA), and a voltage divider (Phidgets Inc., Canada). PowerLab was used for data acquisition, inspiratory and expiratory peak detection, and rate and amplitude calculation. Data were sampled at 1 kHz, filtered with a 0.4–25 Hz band-pass filter, and smoothed with a 50-ms moving window. Automatic peak detection was validated with manual peak detection.

Minute volume is approximated by first calculating the integral of the voltage channel for each breath, summing across one minute, then normalizing against the average value of the first 30 minutes. Values are shown after normalization as the raw values vary considerably across animals. Values during the episodes when the sensor accidentally fell off due to the animal body rotation were excluded.

Stereotaxic surgery

Mice were anesthetized with isoflurane (5% induction, 1.5–2% maintenance with a nose cone; Dräger Vapor 2000, Draegar, Inc., USA) and placed onto a water recirculating heating pad throughout the surgery. Mice were placed on a stereotaxic frame (David Kopf Instruments, USA), the skull was exposed, and the cranium was drilled with a micro motor handpiece drill (Foredom, USA: one or two holes for viral injection(s) or pharmacological delivery, two holes for screws with implantation, one or two holes for optic fibers, and one hole for a micro thermistor). The virus or drug was injected unilaterally (right side) or bilaterally into the PBL (anteroposterior (AP), -1 mm from lambda; mediolateral (ML), ±1.5 mm; dorsoventral (DV), -3.5 mm, re-zero at the midline with the same AP). Injection of the virus or drug was administered with a glass pipette (tips broken for an inner diameter of

20 μm) connected to the Nanoject III Programmable Nanoliter Injector (Drummond Scientific, USA) at a rate of 60 nL/min. Naloxone was injected at a rate of 100 nL/min with a syringe (65458-01, Hamilton, USA) connected to an ultra-micropump (UMP-3, World Precision Instruments, USA). A glass pipette or syringe needle was retracted from the brain slowly after 5–10 min. For implantation, optic fibers were implanted above the injection site with the DV noted below, and the micro thermistor head was carefully lowered into the hole above the nasal cavity (AP +3.5 from the nasal fissure, ML 0.3). The implants were covered with superglue and dental cement for stabilization. Behavioral experiments were performed three weeks after virus injection and one week after the micro-thermistor implantation unless otherwise noted.

For the PBL-specific conditional knockout of the *Oprm1* gene, $Oprm1^{fl/fl}$ mice were bilaterally injected with 200 nL of AAVDJ-CAG-Cre-GFP (1.25E+12 GC/mL) or control AAVDJ-CAG-GFP (2.10E+12 GC/mL) (Salk Institute Viral Vector Core) into the PBL.

For PBL-specific rescue of the *Oprm1* gene, $Oprm1^{Cre/Cre}$ mice were bilaterally injected with 200 nL of AAV-hSyn-DIO-mCherry-T2A-FLAG-hOprm1 (1.5E+13 GC/mL) or control AAV-DIO-eYFP (2.12E+12 GC/mL) into the PBL.

For fiber photometry, $Oprm1^{Cre/+}$ mice were unilaterally injected with 200 nL of AAV-DIO-jGCaMP7s (3.75 E+13 GC/mL) or control AAV-DIO-eYFP (2.12E+12 GC/mL) into the PBL, and a stainless steel mono fiberoptic cannula (400 μm diameter, 0.37 NA, Doric Lenses) was implanted 0.05 mm above the injection site.

For chemogenetics, 200 nL of AAV-DIO-hM3Dq-mCherry (6.56E+11 GC/mL), AAV-DIO-KORD-mCitrine, or control AAV-DIO-eYFP (2.12E+12 GC/mL) was bilaterally injected into the PBL of $Oprm1^{Cre/+}$ (for hM3Dq) or $Oprm1^{Cre/Cre}$ (for KORD) mice.

Pharmacology

Morphine sulfate (Spectrum Chemical, USA) was dissolved in 0.9% saline to make a 4 mg/mL working concentration. The final concentration of morphine was 10 mg/kg in PBL-specific *Oprm1* knockout tests (intraperitoneal, i.p.), 80 mg/kg in PBL-specific rescue of OIRD (subcutaneous, s.c.), and 40 mg/kg in all other experiments (i.p.) (**Table S3.1**). The loss of the *Oprm1* gene decreases morphine sensitivity (**Figure 3.1C**, $p < 0.0001$ between each genotype pairs after morphine injection, two-way ANOVA with Bonferroni's *post hoc* comparison), so we used a higher dose (40 mg/kg) in the $Oprm1^{Cre}$ background and a lower dose (10 mg/kg) in the wild type *Oprm1* background ($Oprm1^{fl/fl}$). Anesthesia reduces the breathing rate and morphine responses, therefore, a higher dose of 80 mg/kg was used in anesthetized mice.

For the characterization of morphine-induced respiratory depression with the WBP, animals were introduced into the WBP chamber for three 20 min habituation sessions before testing. During testing, mice were introduced into the WBP chamber 0–10 min before morphine injection and 30–40 min after morphine injection. For each recording session, after 5–8 min of chamber introduction, a stable pattern, defined as the baseline fluctuation less than 20 bpm within any minute, was reached and maintained until the end of the recording. The average value of a stabilized 1-min segment was analyzed. In each experiment, control and experimental groups were analyzed with the same criteria described above.

For PBL-specific rescue of OIRD with naloxone, wild type mice were kept under isoflurane anesthesia until the breathing rate was stable (fluctuation < 10 bpm) for 10 min. Then, 80 mg/kg morphine (s.c.) was systemically administered. After 30 min, 200 nL of 0.4 mg/mL naloxone (Somerset Therapeutics, USA) and FluoSpheres (540/560, 10% v/v, Thermo Fisher, USA) mixture or a control 0.9% saline-FluoSpheres mixture was

stereotaxically injected bilaterally into the PBL, at a rate of 100 nL/min. Breathing was analyzed from three 2-min episodes: immediately before morphine injection, 30 min after morphine injection, and 10 min after naloxone or saline injection.

For hM3Dq-dependent activation of PBL^{Oprm1} neurons, *Oprm1*$^{Cre/+}$ mice were attached with the patch cord to their respiration sensor and placed in an empty standard mouse cage. After 30 minutes, 40 mg/kg morphine was intraperitoneally injected into the test animal. After another 30 minutes, 5 mg/kg CNO was intraperitoneally injected into the test animal. For quantification of the breathing rate and minute volume, two time periods (0–10 min before and 20–30 min after CNO injection) were analyzed.

For endogenous receptor activation of PBL^{Oprm1} neurons, wild type mice were kept under 1–1.5% isoflurane anesthesia until breathing rate is stable (fluctuation < 10 bpm) for 10 min. Then, 80 mg/kg morphine (s.c.) was systemically administered. After 30 min, 200 nL of the pharmacological agent (**Table S3.1**) was stereotaxically injected into the PBL bilaterally. 50 nL of Cholera Toxin Subunit B (CTB)-555 was subsequently injected with the same coordinates to mark the injection site. Breathing was analyzed from three 2-min episodes: immediately before morphine injection, 30 min after morphine injection, and 30 min after drug injection.

Fiber photometry

Fiber photometry (1-site Fiber Photometry System, 405 and 465 nm, Doric Lenses Inc, Canada) with Doric Neuroscience Studio software was used to record PBL^{Oprm1} neural activities. GCaMP isosbestic fluorescence (405-nm excitation) and calcium-dependent fluorescence (465-nm excitation) were recorded at a sampling rate of 12 kHz, and data were analyzed with the Doric Neuroscience Studio software. F0 was calculated by a least mean squares fitting of the 405-nm channel relative to the 465-nm channel, and ΔF/F was

calculated as (F_{465}-F_{405_fitted})/F_{405_fitted}. Data were further analyzed with custom MATLAB scripts. Animals with fluctuating isosbestic signals indicating insecure implants were not used for the experiment.

For concurrent measurements of PBL^{Oprm1} neural activity and respiration, animals were recorded in their home cage for 30 min before and 30 min after i.p. morphine injection at 40 mg/kg. Cross-correlation analysis between the calcium signals and respiration data was performed with the z-scored data, then with the MATLAB “xcorr” function using the normalized option such that autocorrelations at zero lag equal 1. Calcium peaks were detected with the MATLAB “findpeaks” function.

Convergent cross-mapping

State-space reconstruction models were generated using the framework of convergent cross mapping (Sugihara et al., 2012), a nonlinear time series embedding method (Sugihara and May, 1990) based on the Takens theorem and its generalized form (Deyle and Sugihara, 2011) that builds low-dimensional manifolds from time series and makes predictions across variables. Analysis and predictions were calculated using the R package rEDM 0.7.2 (https://cran.r-project.org/web/packages/rEDM/) for evaluation and rEDM 0.7.4 (https://ha0ye.github.io/rEDM/) for model predictions in the RStudio environment. This program was run on a dual Intel Xeon Gold 6148 Server with 384GB RAM or an Intel Core i9 2.4 GHz MacBook Pro with 32 GB RAM. Key parameters were determined individually by lagged coordinate embedding using the simplex function implementation in rEDM to optimize predictive skill as measured by the predicted over observed rho. Parameters include the delay tau, which gives the characteristic timescale of the time series, and the embedding dimensionality, which estimates the number of variables driving the system and approximates the real number of variables as given by the Whitney embedding

theorem (Whitney, 1936) as minimally equal to the real number n of variables, but no more than two times n + 1 ($n \leq E \leq 2n + 1$). The choice of tau was also informed by minimizing mutual information (Fraser and Swinney, 1986). This approximately corresponds to an autocorrelation of ~0.3, which was applied if it maximized predictive skill across datasets. To prevent data contamination, an exclusion radius was applied that was larger than the respiration rate smoothing window of five timesteps. Whenever the data allowed, an exclusion radius of E*tau was applied, unless the data was insufficient to apply this upper bound. In this case, the exclusion radius would be made just larger than tau.

Chemogenetics

For KORD-mediated inhibition, salvinorin B (SALB, Cayman Chemical, USA) was diluted in 100% DMSO to make a 15 mg/mL stock solution, then further diluted in 0.9% saline (10% v/v) to make a 1.5 mg/mL working suspension. The control used consisted of DMSO diluted in 0.9% saline to make 10% v/v. Mice were injected with 5 µL/g of body weight. The final concentration was 7.5 mg/kg. Breathing recording was performed with the WBP 0–10 min before and 0–10 min after the DMSO/SALB injection, following protocols as described for WBP experiments in the “Pharmacology” section. Animals that did not show the viral expression on one side were excluded from the analysis.

For hM3Dq-mediated excitation, clozapine-N-oxide (CNO, Cayman Chemical, USA) was diluted in 0.9% saline to make a 1 mg/mL working solution. No precipitate in the solution was observed, indicating that the specific polymorph of the drug exhibits sufficient water solubility. Mice were injected with 5 µL/g of body weight, and the final concentration was 5 mg/kg. Breathing recording and quantification were performed as described in the “Pharmacology” section.

RiboTag profiling and library generation

Isolation of polysome-associated mRNA using RiboTag was performed as previously described with minor modification (Sanz et al., 2019; Sanz et al., 2009). Briefly, 250-μm thick slices containing the PBL were obtained using a VT 1200S Vibratome (Leica, Germany). The region of interest was further dissected with surgical scissors. Tissues were transferred into 1.5 mL microcentrifuge tubes containing homogenization buffer (50 mM Tris, pH 7.5, 100 mM KCl, 12 mM $MgCl_2$, 1% Nonidet P-40, 1 mM dithiothreitol (DTT), 200 U/mL RNasin, 1 mg/mL heparin, 100 μg/mL cycloheximide, and 1× protease inhibitor mixture) and mechanically dissociated and lysed using pellet pestles (7495211500-DS, DWK Life Sciences LLC, USA). Lysates were centrifugated for 10 min at 12,000 rpm at 4 °C. Post mitochondrial supernatants were transferred to fresh 1.5 mL microcentrifuge tubes. For immunoprecipitation, 4 μL of anti-hemagglutinin1.1 antibody (BioLegend, USA) was added to the lysate-containing tube and incubated for 4 h at 4 °C on a microtube rotator. After incubation, magnetic protein A/G beads (Cat. No. 88803; Thermo Fisher Scientific) were added to the lysate with antibody prior to incubation on a microtube rotator at 4 °C overnight. The following day, the microcentrifuge tubes were placed into the magnetic stand on ice. The supernatant was removed from sample tubes and used for non-Oprm1 control subsequently. The magnetic beads were washed with high-salt buffer (50 mM Tris, pH 7.5, 300 mM KCl, 12 mM $MgCl_2$, 1% Nonidet P-40, 1 mM DTT, and 100 μg/mL cycloheximide) to remove the non-specific binding from immunoprecipitation. After washing, 350 μL of RLT plus buffer with β-mercaptoethanol from the RNeasy Mini Kit (Qiagen, Germany) was added. The extraction of total RNA was performed with the RNeasy Mini Kit. All RNA samples were quantified with the Qubit RNA Assay Kit (Invitrogen, USA) and analyzed with the RNA 6000 Pico Kit (Agilent, USA).

Isolated RNA was prepared using the Trio RNA-Seq (Cat. No. 0507-08; NuGEN, USA). Briefly, cDNA was synthesized from the total RNA using reverse transcriptase with

oligo dT and resynthesized to produce double-stranded cDNA. After amplification of double-stranded cDNA, cDNA was purified with AMPure XP Beads (Cat. No. A63881; Beckman Coulter, USA), fragmented to the library, and classified using a barcoded adaptor. All libraries were quantified by qPCR and analyzed *with the RNA 6000 Pico Kit.*

RiboTag profiling analysis

RNA library quality was confirmed using the 2100 Bioanalyzer (Agilent, USA). Barcoded samples *were pooled* and sequenced on the NextSeq500 (Illumina, USA) with the 75-bp read length single-end format. Image analysis and base calling were conducted using the Illumina CASAVA-1.8.2 software. Sequencing read quality was evaluated with the FastQC package (http://www.bioinformatics.babraham.ac.uk/projects/fastqc). Fastq reads were aligned to the reference genome (GRCm38.p6) using the STAR tool (version 2.7.2) (Dobin et al., 2013). The quantification package RSEM (version 1.2.28) (Li and Dewey, 2011) was utilized to calculate gene expression from BAM files. In doing so, estimated count and TPM (Transcripts Per Million) were computed. Fold changes were calculated from TPM values (estimated counts > 20) between HA-tag and controls. To visualize fold changes, we utilized the ggplot2 package from R. UP (> 3 fold change) and DOWN (< -3 fold change) were highlighted with orange and blue colors, respectively. Key genes for the parabrachial marker and GPCRs were further annotated.

Histology

Mice were euthanized with CO_2 at a flow rate of 1.2 liters per minute (LPM), perfused intracardially with ice-cold phosphate-buffered saline (PBS), and fixed with 4% paraformaldehyde (PFA) in phosphate buffer (PB). The brain was extracted, post-fixed in 4% PFA overnight and dehydrated in 30% sucrose in PBS until sliced. Frozen brains were cut into 50 μm coronal slices using a CM 1950 cryostat (Leica, Germany) and stored in PBS

before mounting. The slices were mounted on Superfrost Microscope Slides (Fisher Scientific, USA) with DAPI Fluoromount-G mounting media (Southern Biotech, USA) for imaging.

Immunohistochemistry

To validate the co-expression of Cre:GFP and Rpl22:HA in PBL^{Oprm1} neurons, immunohistochemistry for HA and GFP was performed. To validate the conditional knockout of the *Oprm1* gene in the PBL, we performed immunohistochemistry for MOR.

Mice were euthanized with CO_2 at a flow rate of 1.2 LPM, perfused intracardially with ice-cold PBS, and fixed with 4% PFA in PB. The brain was extracted, post-fixed in 4% PFA overnight and dehydrated in 30% sucrose in PBS until sliced. Frozen brains were cut into 30 µm coronal slices with a CM 1950 cryostat and stored in PBS.

Sections were washed with PBST (PBS with 3% Tween-20, Fisher BioReagents, USA). After blocking with 3% normal donkey serum (NDS, Jackson ImmunoResearch Inc., USA) for 1 h at room temperature and rinsing with PBST, the slices were incubated with the corresponding antibodies: mouse monoclonal anti-HA1.1 (1:1000, BioLegend, USA), chicken anti-GFP (1:1000, Aves Labs Inc, USA), and rabbit anti-MOR (1:1000, ImmunoStar, USA) antibodies at 4 °C for overnight (anti-HA1.1 and anti-GFP) or 24 h (anti-MOR). The next day, brain tissues were rinsed with PBST and incubated in Alexa Fluor® 647-conjugated Donkey Anti-Mouse IgG, Alexa Fluor® 488-conjugated Donkey Anti-Chicken IgY, and Alexa Fluor® 647-conjugated Donkey Anti-Rabbit IgG (1:1000, Jackson ImmunoResearch Inc., USA) in 3% NDS for 90 min at room temperature. After washing with PBS, brain slices were mounted on Superfrost Microscope Slides with DAPI Fluoromount-G mounting media for imaging.

RNA in situ hybridization

RNA *in situ* hybridization was performed using the RNAscope Fluorescent Multiplex Assay using the probes and kits purchased from Advanced Cell Diagnostics (ACD, USA). Brains were collected from wild type mice and immediately frozen with 2-methylbutane chilled with dry ice. Frozen brains were cut into 20-µm coronal slices with a CM 1950 cryostat and directly mounted onto the Superfrost Plus Microscope Slides (Fisher Scientific). Sample preparation, pretreatment, and signal detection were performed according to the ACD protocols. Probes used are listed below: *Oprm1* (ACD #315841), *Htr2a* (#401291), *Cckar* (#313751), *Drd5* (#494411), *Tacr3* (#481671), *Tacr1* (#428781), *Cre* (#402551), *Slc17a6* (#319171), and *Slc32a1* (#319191).

Two to three representative images from the PBL (AP = -5.0 to -5.2) were selected from n = 3 mice, and PBL cells within a field of view of 300 µm x 300 µm (for *Oprm1* colocalization with *Cre*, *Htr2a*, *Cckar*, *Tacr3*, *Tacr1*, and *Drd5*) or 600 µm x 600 µm (for *Oprm1* colocalization with *Slc17a6* and *Slc32a1*) were used for quantification. Quantification of the colocalization is done manually with ImageJ software according to the ACDBio technical note. DAPI-stained nuclei were first identified, then the cell contour was defined with a 2-µm radius surrounding the DAPI signals. Cells containing at least five puncta inside the imaginary boundary were labeled as positive.

Imaging

Images for verification of injection and implantation site and anti-MOR staining for conditional knockout validation were taken with a BZ-X710 all-in-one fluorescence microscope with BZ-X viewer software under a 10X, 0.45 NA objective (Keyence, Japan). Images for anti-HA & anti-GFP immunostaining, RNAscope, and *Oprm1*^{Cre}::Ai14 expression characterization were acquired with an FV3000 Confocal Laser Scanning Microscope with FV31S-SW software under a 20X, 0.75 NA or 40X, 0.95 NA UPLSAPO objective (Olympus,

Japan). For comparison, images were processed with the same gain, offset, and exposure time.

Locomotor activity test

To measure the locomotor activity after morphine injection, *Oprm1*$^{Cre/+}$ mice were injected with 40 mg/kg morphine or saline intraperitoneally and placed back into the home cage. After 30–40 minutes, animals were introduced to the center of an open field arena (50 cm x 50 cm) and allowed to explore for 10 minutes. The velocity of the animal was analyzed using the video-tracking software (EthoVision XT 12, Noldus Information Technology Inc., USA).

Statistical Analysis

All data are shown as mean ± SEM and analyzed using either a student's t-test, one-way ANOVA with Tukey's *post hoc* comparison, or two-way ANOVA with Bonferroni's *post hoc* comparison. All statistical analyses were performed with Prism 6 (GraphPad Software Inc., USA). ns $p > 0.05$, * $p < 0.05$, ** $p < 0.01$, *** $p < 0.001$, **** $p < 0.0001$.

For a detailed list of resources, please refer to **Table S3.2**.

3.4 Results

To examine the contributions of global MOR signaling to OIRD, we generated an *Oprm1* reporter mouse line in which the endogenous *Oprm1* gene was knocked out by inserting a Cre:GFP cassette upstream of the start codon (*Oprm1*^{Cre}) (**Figure 3.1B and Figure S3.1A** for validation), and measured the effects of systemic morphine injection on breathing rhythms via whole-body plethysmography (**Figure 3.1A**). After receiving a morphine injection (40 mg/kg, i.p.), wild type mice exhibited a significantly lower respiratory rate (363.1 ± 11.1 bpm to 168.1 ± 8.0 bpm, data are represented as mean ± SEM throughout

the paper). In contrast, mice lacking one or both functional copies of the *Oprm1* gene (*Oprm1*$^{Cre/+}$ and *Oprm1*$^{Cre/Cre}$) exhibited more moderate reductions in respiratory rate (384.2 ± 5.7 bpm to 242.2 ± 8.0 bpm; 370.6 ± 1.6 bpm to 337.9 ± 11 bpm, respectively) (**Figure 3.1C, D**). No significant differences in baseline respiratory rate were observed among genotypes, indicating that the knockout of *Oprm1* gene does not influence the baseline breathing rate (**Figure 3.1D and Figure S3.1D**). It should be noted that the differences in the morphine-induced respiratory responses across genotypes may be partially influenced by morphine pharmacokinetics, if opioid receptor deficiency, in turn, affects opioid metabolizers and transporters. *Oprm1*, therefore, plays a vital role in OIRD.

We then used pharmacological and genetic tools to manipulate opioid signaling specifically in the PBL. First, wild type mice received a systemic injection of morphine followed by an infusion of naloxone directly into the PBL (**Figure 3.1E**). To facilitate stereotaxic naloxone delivery, we lightly anesthetized mice with 1–1.5% isoflurane and monitored their breathing using a piezoelectric sensor that detects chest movements (Levitt et al., 2015). After systemic injection of morphine (80 mg/kg, s.c.), a high concentration was used in anesthetized animals), the breathing rate dramatically decreased from 121.0 ± 3.4 bpm to 89.1 ± 3.5 bpm, and subsequent stereotaxic injection of naloxone into the PBL recovered the breathing rate back to pre-morphine baseline (120.8 ± 3.7 bpm) (**Figure 3.1F, G**). We then explored whether the expression of the *Oprm1* gene in the PBL is necessary and sufficient for OIRD. To assess necessity, we conditionally knocked out the *Oprm1* gene using stereotaxic delivery of a recombinant adeno-associated virus (AAV) expressing Cre recombinase into the PBL of the *Oprm1*$^{fl/fl}$ mice, in which the *Oprm1* gene is flanked by loxP sites (**Figure 3.1H**). Compared to mice receiving GFP-expressing control virus, PBL-specific knockout of the *Oprm1* gene attenuated OIRD following systemic injection of morphine (10 mg/kg, i.p.), as measured by whole-body plethysmography (breathing rate

changes in GFP group: -136.6 ± 21.1 bpm; Cre group: -76.4 ± 11.6 bpm) (**Figure 3.1I and Figure S3.2A–C**). To test sufficiency, we reintroduced the wild type *Oprm1* gene into the PBL^{Oprm1} neurons of Cre-expressing *Oprm1*-null mice. This was achieved by injecting an AAV expressing Cre-dependent human MOR (AAV-hSyn-DIO-mCherry-T2A-FLAG-hMOR) (**Figure 3.1J**) into the PBL of *Oprm1*$^{Cre/Cre}$ mice. Selective expression of hMOR in the PBL restored the OIRD phenotype (hMOR group, post-saline: 359.0 ± 5.1 bpm; post-morphine: 299.0 ± 3.6 bpm, 40 mg/kg, i.p.) compared to the control group (**Figure 3.1K and Figure S3.2D**). Note that the breathing rate measured by the piezoelectric sensor under anesthesia (**Figure 3.1G**) is ~3-fold lower than that measured in a plethysmography chamber (**Figure 3.1K**). Together, these data strongly support the conclusion that the *Oprm1* gene expression in the PBL mediates OIRD in mice.

We then focused on PBL^{Oprm1} neurons and explored their relationship with OIRD. PBL^{Oprm1} neurons are mostly glutamatergic and express higher levels of the *Oprm1* gene than the adjacent KF nucleus, which provides post-inspiratory drive (Dutschmann and Herbert, 2006; Levitt et al., 2015; Navarrete-Opazo et al., 2020; Varga et al., 2020) (**Figure 3.1B–C**). We devised an experimental platform to simultaneously measure PBL^{Oprm1} neuronal activity and respiration in awake, freely moving mice using fiber photometry calcium-mediated fluorescence measurements with a thermistor implanted into the nasal cavity (**Figure 3.2A**). The thermistor-based respiration monitoring device detects the temperature change between inhaled and exhaled air and converts breath-to-breath fluctuations in resistance into voltage signals (McAfee et al., 2016). We stereotaxically injected an AAV expressing Cre-dependent jGCaMP7s (AAV-DIO-jGCaMP7s) into the PBL, then implanted an optic fiber into the PBL of *Oprm1*$^{Cre/+}$ mice and a respiration sensor in the nasal cavity (**Figure 3.2B**). PBL^{Oprm1} activity and breathing rate exhibited a tight positive correlation (**Figure 3.2C–D, H**). Moreover, morphine administration substantially decreased

the breathing rate (326.5 ± 17.0 bpm to 151.8 ± 14.7 bpm, 40 mg/kg, i.p.) (**Figure 3.2H, J, L, and N**) despite the morphine-induced increase in locomotor activity (**Figure S3.3**), which one would expect to elevate the breathing rate. Besides, morphine decreased calcium activity (**Figure 3.2H, J, O, and Q**), as well as eliminated any spontaneous fluctuations in both breathing and calcium signals (**Figure 3.2N, Q**). The opposite effects on locomotion and calcium activity observed after morphine administration demonstrated that the breathing-associated fluctuation of PBL^{Oprm1} activity is not affected by the movement, which is further demonstrated in another manuscript (Liu et al., 2020). In contrast, saline injection largely preserved the original patterns of the signals (**Figure 3.2D, F, L–M, and O–P**). Using convergent cross-mapping (CCM) (Sugihara et al., 2012), a statistical algorithm that makes predictions from independent time-series data, we predicted changes in respiratory rate using the calcium signal as input (76.2 ± 8.1%, pre-morphine predictability) (**Figure S3.4**). Interestingly, systemic morphine administration not only reduced the correlation coefficient (**Figure 3.2I, K**) but also completely abolished the predictive relationship between respiratory rate and the calcium signal (12.5 ± 20.2%, post-morphine predictability) (**Figure S3.4C–D**). Conversely, the saline injection did not alter the correlation between these signals (**Fig 3.2E, G, and Figure S3.4A–B**). These results indicate that PBL^{Oprm1} neurons are critically involved in modulating respiratory rate and that morphine suppresses both the PBL^{Oprm1} neuronal activity and its coupling with the breathing rate.

To further investigate PBL^{Oprm1} neurons' role in breathing regulation, we specifically manipulated their activity using chemogenetic tools, namely Designer Receptor Exclusively Activated by Designer Drugs (DREADD) (Roth, 2016). If PBL^{Oprm1} neurons directly regulate breathing, inhibiting their activity via a $G_{i/o}$-coupled DREADD should recapitulate the OIRD phenotype. Furthermore, this should also happen in *Oprm1* knockout mice, which failed to display OIRD when given systemic morphine (**Figure 3.1C–D**). We expressed a κ-opioid

receptor-derived DREADD (KORD) (Vardy et al., 2015) Cre-dependently and bilaterally in PBL^{Oprm1} neurons of *Oprm1*$^{Cre/Cre}$ mice (**Figure 3.3A**), to phenocopy the inhibition of MOR by morphine, because KOR and MOR have high structural similarity (Che et al., 2018) and engage with conserved intracellular signaling pathways (Al-Hasani and Bruchas, 2011). Systemic injection of the synthetic ligand of KORD, salvinorin B (SALB, 7.5 mg/kg, i.p.), decreased the respiratory rate (352.8 ± 18.4 bpm to 317.8 ± 3.6 bpm) compared to the DMSO-injected control group (344.8 ± 13.8 bpm to 342.4 ± 4.1 bpm) (**Figure 3.3B and Figure S3.5A–B**). We did not observe significant breathing amplitude changes upon SALB injection in either control or KORD-expressing animals (**Figure 3.5B–C**).

We next asked whether artificial activation of PBL^{Oprm1} neurons could prevent OIRD in mice. We expressed hM3Dq, a metabotropic acetylcholine receptor-derived excitatory DREADD, in PBL^{Oprm1} neurons via bilateral injection of an AAV encoding Cre-dependent hM3Dq into *Oprm1*$^{Cre/+}$ mice (**Figure 3.3C**). Additionally, we implanted a micro-thermistor sensor into the nasal cavity to monitor respiratory rhythm in awake, freely moving mice over the course of OIRD (**Figure S3.5D**). Upon systemic morphine injection (40 mg/kg, i.p.), the respiratory rate decreased significantly within 10 min (from 332.0 ± 25.6 bpm to 124.6 ± 9.1 bpm) (**Figure 3.3D–E**). We then systemically injected the hM3Dq agonist, clozapine-N-oxide (CNO, 5 mg/kg, i.p.), into the same animal to activate PBL^{Oprm1} neurons. CNO injection increased the breathing rate in hM3Dq-expressing animals (268.0 ± 13.5 bpm) to a level comparable to controls that did not receive morphine (275.7 ± 24.9 bpm). Nevertheless, CNO did not rescue breathing rates in eYFP-expressing control animals (120.0 ± 4.3 bpm) (**Figure 3.3D–F and Figure S3.5E**). A complete rescue was also observed in minute volume (**Figure S3.5F–G**). These data show that activation of PBL^{Oprm1} neurons is sufficient to restore normal breathing rhythms in mice displaying OIRD.

Having determined that chemogenetic activation of PBL^{Oprm1} neurons could effectively prevent OIRD, we sought to identify endogenous signaling pathways that could be used to activate PBL^{Oprm1} neurons. To identify the active transcriptome enriched in PBL^{Oprm1} neurons, we sequenced ribosome-associated mRNAs from the PBL of *Oprm1*^{Cre}::RiboTag mice, which express hemagglutinin (HA)-tagged ribosomal protein Rpl22 in *Oprm1*$^{+}$ neurons (**Figure 3.4A–B**) (Sanz et al., 2019). We identified 69 mRNAs upregulated over three-fold in PBL^{Oprm1} neurons than non-*Oprm1* neurons in the PBL (**Figure 3.4C**). *Oprm1*, as well as other major parabrachial markers (*Tac1, Foxp2*, and *Adcyap1*) were enriched, but *Calca* and *Pdyn*, markers for the external lateral and dorsal lateral parabrachial nucleus, were not (Huang et al., 2020; Palmiter, 2018). Notably, the PBL^{Oprm1} active transcriptome revealed several GPCRs expressed at high levels in these neurons, which we subsequently investigated as potential pharmacological targets to rescue OIRD.

We selected five excitatory GPCRs for pharmacological manipulation and confirmed that they were expressed in PBL^{Oprm1} neurons by RNA *in situ* hybridization (**Figure S3.6A–B**). These GPCRs were 5-hydroxytryptamine receptor 2A (*Htr2a*), cholecystokinin A receptor (*Cckar*), tachykinin receptor 1 (*Tacr1*), tachykinin receptor 3 (*Tacr3*), and dopamine receptor D5 (*Drd5*). We systemically injected their agonists (TCB-2, CCK8S, Substance P, Senktide, and SKF83959, respectively) into the PBL of anesthetized mice after inducing OIRD with morphine (80 mg/kg, s.c.; breathing rate before morphine: 115.4 ± 1.6 bpm, after morphine: 77.9 ± 2.3 bpm; **Figure 3.4D–E and Table S3.1**). Three of the five agonists tested (TCB-2, CCK8S, and Substance P) increased the respiratory rate (98.1 ± 7.9, 117.1 ± 6.4, 100.8 ± 4.6 bpm; **Figure 3.4F and Figure S3.6C–E**). Notably, these same drugs have been shown to modulate respiratory rhythm in different contexts by activating other respiratory centers, and some have been associated with an anti-morphine effect (Ellenberger and Smith, 1999; Hedner et al., 1984; Niebert et al., 2011). Our findings suggest that activating

PBL^{Oprm1} neurons through endogenous signaling pathways may effectively treat OIRD in patients.

3.5 Discussion

We have identified a population of neurons in the pontine respiratory group, the PBL^{Oprm1} neurons, as critical mediators of morphine-induced respiratory depression and candidates for its rescue in intact mice. Genetic deletion of *Oprm1* from the PBL attenuated OIRD, while reintroducing human MOR into the PBL^{Oprm1} neurons restored OIRD. By combining cell-type-specific tools with breathing monitoring in awake behaving mice, we have demonstrated that PBL^{Oprm1} neurons are regulators of the breathing rhythm and pattern. Systemic morphine administration dramatically abolishes the activity of these neurons and weakens their control on breathing. Furthermore, chemogenetic inhibition of PBL^{Oprm1} neurons mimics OIRD, and prolonged optogenetic inhibition of PBL^{Oprm1} neurons induces apnea (observations from our group (Liu et al., 2020)), which precedes cardiorespiratory collapse prior to overdose-induced death. By contrast, artificial activation of PBL^{Oprm1} neurons, either chemogenetically or pharmacologically, successfully restores breathing in mice experiencing OIRD (**Figure S3.7**).

Investigating OIRD with cell-type-specific approaches

Recent studies have demonstrated the involvement of both pontine and medullary respiratory groups in OIRD (Bachmutsky et al., 2020; Varga et al., 2020) without reaching a consensus on the key players. We think this is mostly due to the lack of specificity from the pharmacological and genetic deletion approaches and the intricacies of physiological preparations, both of which hampers reproducibility. In comparison, we exploited the *Oprm1*^{Cre} mouse line which provides access to a restricted neuronal population, and obtained multi-faceted evidence supporting the role of the parabrachial nucleus in OIRD. In our view,

OIRD is a synergistic outcome from impairment of the interconnected pontomedullary breathing network that widely expresses MOR both pre- and post-synaptically (Arvidsson et al., 1995; Cinelli et al., 2020; Hurlé et al., 1985; Lalley, 2006; Wei and Ramirez, 2019). For example, parabrachial neurons send tonic excitatory inputs to the preBötC (Fulwiler and Saper, 1984; Huang et al., 2020; Liu et al., 2020; Yokota et al., 2015), and both of these areas express MOR (Del Negro et al., 2018; Erbs et al., 2015). Besides, the preBötC, as the breathing pattern generator, has been known to contribute to the OIRD phenotype, yet the level of its involvement varies across species and overdose models. Deletion of the *Oprm1* gene from the preBötC by injecting AAV that encodes Cre-recombinase into the preBötC of the *Oprm1*$^{fl/fl}$ mice attenuated the respiratory rate depression by intraperitoneal morphine injection (Bachmutsky et al., 2020; Varga et al., 2020). Interestingly, the effect largely depends on the dosage of opioids (Varga et al., 2020). Naloxone infusion into the preBötC prevented the respiratory rate depression induced by intravenous fentanyl/remifentanil injection in rats (Montandon et al., 2011), but not in dogs (Mustapic et al., 2010) or rabbits (Stucke et al., 2015). It would thus be valuable to test the contribution of *Oprm1*-expressing neurons within the preBötC in regulating breathing rhythm with multiple OIRD models.

One challenge of elucidating the OIRD mechanism is how to access a group of neurons while simultaneously record breathing over the course of OIRD. Traditional respiratory monitoring approaches in rodents, such as *in situ* or *in vivo* anesthetized preparations and plethysmography chambers, are more challenging to achieve this goal. Therefore, we utilized the implantable temperature sensor to monitor breathing in awake, unrestrained, behaving mice with unprecedented freedom to access the brain due to its open configuration. With this approach, we implemented chemogenetics and *in vivo* neural activity monitoring simultaneously with breathing rhythm recording. Similar techniques can be applied to the *Oprm1*-expressing neurons in the preBötC, KF, the postinspiratory complex

(Anderson et al., 2016), and other respiratory centers to resolve the long-standing debate on their contributions in OIRD (Lalley et al., 2014; Montandon and Horner, 2014).

PBL^{Oprm1} neurons' role in breathing regulation and OIRD

The parabrachial complex has long been reported to modulate respiration and sometimes exert opposing effects depending on the location of artificial manipulation (Chamberlin and Saper, 1994; Dutschmann and Dick, 2012; Navarrete-Opazo et al., 2020). Stimulation of the PBL results in tachypnea, whereas stimulation of the KF elicits prolonged post-inspiration and bradypnea (Dutschmann and Herbert, 2006; Levitt et al., 2015; Varga et al., 2020). Consistent with these previous reports, our monitoring and manipulation data suggest that PBL^{Oprm1} neurons have the most substantial effect on the breathing rate (Navarrete-Opazo et al., 2020). In addition to breathing, the PBL also regulates various homeostatic functions (Huang et al., 2020) and incorporates the alarm center, which senses deviations from the homeostasis and relays aversive signals to higher-order brain structures (Palmiter, 2018; Tokita et al., 2009). At the same time, by sending tonic excitatory outputs to medulla respiratory centers (Huang et al., 2020; Liu et al., 2020; Yokota et al., 2015), the parabrachial neurons can increase breathing rhythm under conditions that immediately require more oxygen due to metabolic needs, such as hypoxia (Song and Poon, 2009b) and hypercapnia (Song and Poon, 2009a), in particular, hypercapnic arousal during sleep (Kaur et al., 2020; Kaur et al., 2013; Kaur et al., 2017); or non-metabolic behavioral demands, such as escaping from a threat (Jiang et al., 2004). As a representative glutamatergic population in the PBL (**Figure S3.1**), *Oprm1*-positive neurons are likely to participate in similar physiological processes. Our data demonstrated that an overdose of morphine shuts down PBL^{Oprm1} neurons' activity, preventing them from responding to conditions that decrease respiratory rhythm. These conditions may include hypoxia, hypercapnia, anesthesia, or

sedative drug treatment. Indeed, the incidence of OIRD is dramatically increased when opioids are used together with sedatives and anesthetics (Gupta et al., 2018), and the failure to increase respiratory behavior in response to hypercapnic gas is one characteristic of OIRD (Dahan et al., 2010). On the contrary, a mild inhibition of PBL^{Oprm1} neurons may explain many of the behavioral effects of lower doses of endogenous or exogenous opioids, such as slowed breathing, calmness, and reward (Liu et al., 2020). The current study used morphine as a starting point to induce OIRD, and further investigation is required to determine the involvement of PBL^{Oprm1} neurons under the challenge of other types of sedative agents.

A proof of principle of rescuing OIRD by activating a pontine population

PBL^{Oprm1} neurons are among the key node most vulnerable to opioid action, and their activation is sufficient to restore the breathing rate and tidal volume following morphine administration. This activation can be achieved by exploiting both artificial and, more importantly, endogenous signaling pathways. Besides, manipulating PBL^{Oprm1} neurons located in the dorsolateral pons is associated with lower risk than the respiratory rhythm generators within the deep medulla. We have provided a proof of concept of rescuing OIRD by activating endogenous $G_{q/s}$-coupled GPCRs expressed in PBL^{Oprm1} neurons (**Figure S3.7**). In principle, cell-type-specific manipulation can also be achieved through the collective activation of multiple GPCRs.

Our transcriptomic profiling data suggested that other neuromodulators, such as serotonin, cholecystokinin, and tachykinin, may also involve in respiratory regulation with potential interplay with the opioid system (Ellenberger and Smith, 1999; Hedner et al., 1984; Niebert et al., 2011). The same receptor that we identified, Htr2a, has recently been confirmed to express in the PBL and mediate hypercapnia-induced arousal by integrating serotonergic inputs from the dorsal raphe (Kaur et al., 2020). It would be interesting to

identify other neuromodulatory circuits that may be involved in the regulation of OIRD. Similar transcriptomic profiling strategies can also be applied to the broader breathing control network to exploit the therapeutic potential of GPCRs in reversing OIRD.

3.6 Acknowledgements

Chapter 3, in full, is a reprint of the material as it appears in **Liu, S.**, Kim, D.I., Oh, T.G., Pao, G.M., Kim, J.H., Palmiter, R.D., Banghart, M.R., Lee, K.F., Evans, R.M., Han, S. Neural basis of opioid-induced respiratory depression and its rescue. *Proc. Natl. Acad. Sci.,* 2021, 118(23). The dissertation author was a primary investigator and the first author of this material. The authors would like to thank the Han lab members for the critical discussion of the paper and D. O'Keefe and M. Shields for critical inputs on the manuscript. Supported by grants from the US National Institutes of Health (1R01MH116203 to S.H., MH114831, OD023076, AG062232, NS115183 and AG064049 to K.F.L.), the Bridge to Independence award from the Simons Foundation Autism Research Initiative (SFARI388708) and Brain Research Foundation Fay/Frank Seed Grant (to S.H.), the Salk Women & Science Special Award, the Mary K. Chapman Foundation, and the Jesse & Caryl Philips Foundation graduate fellowships (to S.L.).

3.7 References

Al-Hasani, R., and Bruchas, M.R. (2011). Molecular mechanisms of opioid receptor-dependent signaling and behavior. Anesthesiology, *115*, 1363-1381.

Anderson, T.M., Garcia, A.J., Baertsch, N.A., Pollak, J., Bloom, J.C., Wei, A.D., Rai, K.G., and Ramirez, J.-M. (2016). A novel excitatory network for the control of breathing. Nature *536*, 76-80.

Arvidsson, U., Riedl, M., Chakrabarti, S., Lee, J.-H., Nakano, A.H., Dado, R., Loh, H.H., Law, P.-Y., Wessendorf, M.W., and Elde, R. (1995). Distribution and targeting of a mu-opioid receptor (MOR1) in brain and spinal cord. J. Neurosci. *15*, 3328-3341.

Bachmutsky, I., Wei, X.P., Kish, E., and Yackle, K. (2020). Opioids depress breathing through two small brainstem sites. eLife *9*, e52694.

Boyer, E.W. (2012). Management of opioid analgesic overdose. N. Engl. J. Med. *367*, 146-155.

Chamberlin, N.L., and Saper, C.B. (1994). Topographic organization of respiratory responses to glutamate microstimulation of the parabrachial nucleus in the rat. J. Neurosci. *14*, 6500-6510.

Che, T., Majumdar, S., Zaidi, S.A., Ondachi, P., McCorvy, J.D., Wang, S., Mosier, P.D., Uprety, R., Vardy, E., and Krumm, B.E. (2018). Structure of the nanobody-stabilized active state of the kappa opioid receptor. Cell *172*, 55-67.

Cinelli, E., Bongianni, F., Pantaleo, T., and Mutolo, D. (2020). Activation of μ-opioid receptors differentially affects the preBötzinger Complex and neighbouring regions of the respiratory network in the adult rabbit. Respir. Physiol. Neurobiol. *280*, 103482.

Cui, Y., Kam, K., Sherman, D., Janczewski, W.A., Zheng, Y., and Feldman, J.L. (2016). Defining preBötzinger complex rhythm- and pattern-generating neural microcircuits in vivo. Neuron *91*, 602-614.

Dahan, A., Aarts, L., and Smith, T.W. (2010). Incidence, reversal, and prevention of opioid-induced respiratory depression. Anesthesiology *112*, 226-238.

Dahan, A., Sarton, E., Teppema, L., Olievier, C., Nieuwenhuijs, D., Matthes, H.W.D., and Kieffer, B.L. (2001). Anesthetic potency and influence of morphine and sevoflurane on respiration in μ-opioid receptor knockout mice. Anesthesiology *94*, 824-832.

Dahan, A., van der Schrier, R., Smith, T., Aarts, L., van Velzen, M., and Niesters, M. (2018). Averting opioid-induced respiratory depression without affecting analgesia. Anesthesiology *128*, 1027-1037.

Del Negro, C.A., Funk, G.D., and Feldman, J.L. (2018). Breathing matters. Nat. Rev. Neurosci. *19*, 351-367.

Deyle, E.R., and Sugihara, G. (2011). Generalized theorems for nonlinear state space reconstruction. PLoS One *6*, e18295.

Dobin, A., Davis, C.A., Schlesinger, F., Drenkow, J., Zaleski, C., Jha, S., Batut, P., Chaisson, M., and Gingeras, T.R. (2013). STAR: ultrafast universal RNA-seq aligner. Bioinformatics *29*, 15-21.

Dutschmann, M., and Dick, T.E. (2012). Pontine mechanisms of respiratory control. Compr. Physiol. *2*, 2443-2469.

Dutschmann, M., and Herbert, H. (2006). The Kölliker-Fuse nucleus gates the postinspiratory phase of the respiratory cycle to control inspiratory off-switch and upper airway resistance in rat. Eur. J. Neurosci. *24*, 1071-1084.

Ellenberger, H.H., and Smith, F.M. (1999). Sulfated cholecystokinin octapeptide in the rat: pontomedullary distribution and modulation of the respiratory pattern. Can. J. Physiol. Pharmacol. *77*, 490-504.

Erbs, E., Faget, L., Scherrer, G., Matifas, A., Filliol, D., Vonesch, J.L., Koch, M., Kessler, P., Hentsch, D., Birling, M.C. and Koutsourakis, M. (2015). A mu-delta opioid receptor brain atlas reveals neuronal co-occurrence in subcortical networks. Brain Struct. Funct. *220*, 677-702.

Fraser, A.M., and Swinney, H.L. (1986). Independent coordinates for strange attractors from mutual information. Phys. Rev. A *33*, 1134-1140.

Fulwiler, C.E., and Saper, C.B. (1984). Subnuclear organization of the efferent connections of the parabrachial nucleus in the rat. Brain Res. Rev. *7*, 229-259.

Gupta, K., Prasad, A., Nagappa, M., Wong, J., Abrahamyan, L., and Chung, F.F. (2018). Risk factors for opioid-induced respiratory depression and failure to rescue: a review. Curr. Opin. Anaesthesiol. *31*, 110-119.

Hedegaard, H., Miniño, A.M., and Warner, M. (2020). Drug overdose deaths in the United States, 1999-2018. NCHS data brief *356*.

Hedner, J., Hedner, T., Wessberg, P., and Jonason, J. (1984). Interaction of substance P with the respiratory control system in the rat. Pharmacol. Exp. Ther. *228*, 196-201.

Huang, D., Grady, F.S., Peltekian, L., and Geerling, J.C. (2021). Efferent projections of Vglut2, Foxp2 and Pdyn parabrachial neurons in mice. J. Comp. Neurol. *529*, 657-693.

Hurlé, M.A., Mediavilla, A., and Florez, J. (1985). Differential respiratory patterns induced by opioids applied to the ventral medullary and dorsal pontine surfaces of cats. Neuropharmacology *24*, 597-606.

Jiang, M., Alheid, G.F., Calandriello, T., and McCrimmon, D.R. (2004). Parabrachial-lateral pontine neurons link nociception and breathing. Respir. Physiol. Neurobiol. *143*, 215-233.

Kaur, S., De Luca, R., Khanday, M.A., Bandaru, S.S., Thomas, R.C., Broadhurst, R.Y., Venner, A., Todd, W.D., Fuller, P.M., and Arrigoni, E. (2020). Role of serotonergic dorsal raphe neurons in hypercapnia-induced arousals. Nat. Comm. *11*, 1-15.

Kaur, S., Pedersen, N.P., Yokota, S., Hur, E.E., Fuller, P.M., Lazarus, M., Chamberlin, N.L., and Saper, C.B. (2013). Glutamatergic signaling from the parabrachial nucleus plays a critical role in hypercapnic arousal. J. Neurosci. *33*, 7627-7640.

Kaur, S., Wang, J.L., Ferrari, L., Thankachan, S., Kroeger, D., Venner, A., Lazarus, M., Wellman, A., Arrigoni, E., Fuller, P.M., and Saper, C.B. (2017). A genetically defined circuit for arousal from sleep during hypercapnia. Neuron *96*, 1153-1167.

Lalley, P.M. (2006). Opiate slowing of feline respiratory rhythm and effects on putative medullary phase-regulating neurons. Am. J. Physiol. Regul. Integr. Comp. Physiol. *290*, R1387-1396.

Lalley, P.M., Pilowsky, P.M., Forster, H.V., and Zuperku, E.J. (2014). CrossTalk opposing view: The pre-Bötzinger complex is not essential for respiratory depression following systemic administration of opioid analgesics. J. Physiol. *592*, 1163-1166.

Levitt, E.S., Abdala, A.P., Paton, J.F., Bissonnette, J.M., and Williams, J.T. (2015). Mu opioid receptor activation hyperpolarizes respiratory-controlling Kölliker-Fuse neurons and suppresses post-inspiratory drive. J. Physiol. *593*, 4453-4469.

Li, B., and Dewey, C.N. (2011). RSEM: accurate transcript quantification from RNA-Seq data with or without a reference genome. BMC Bioinformatics *12*, 323.

Liu, S., Ye, M., Pao, G.M., Song, S.M., Jhang, J., and Han, S. (2020). Identification of a novel breathing circuit that controls pain and anxiety. bioRxiv. https://doi.org/10.1101/2020.01.09.900738.

Manzke, T., Guenther, U., Ponimaskin, E.G., Haller, M., Dutschmann, M., Schwarzacher, S., and Richter, D.W. (2003). 5-HT4 (a) receptors avert opioid-induced breathing depression without loss of analgesia. Science *301*, 226-229.

Matthes, H.W., Maldonado, R., Simonin, F., Valverde, O., Slowe, S., Kitchen, I., Befort, K., Dierich, A., Le Meur, M., and Dollé, P. (1996). Loss of morphine-induced analgesia, reward effect and withdrawal symptoms in mice lacking the μ-opioid-receptor gene. Nature *383*, 819.

McAfee, S.S., Ogg, M.C., Ross, J.M., Liu, Y., Fletcher, M.L., and Heck, D.H. (2016). Minimally invasive highly precise monitoring of respiratory rhythm in the mouse using an epithelial temperature probe. J. Neurosci. Methods *263*, 89-94. 10.1016/j.jneumeth.2016.02.007.

Miller, J.R., Zuperku, E.J., Stuth, E.A.E., Banerjee, A., Hopp, F.A., and Stucke, A.G. (2017). A subregion of the parabrachial nucleus partially mediates respiratory rate depression from intravenous remifentanil in young and adult rabbits. Anesthesiology *127*, 502-514.

Montandon, G., and Horner, R. (2014). CrossTalk proposal: The preBötzinger complex is essential for the respiratory depression following systemic administration of opioid analgesics. J. Physiol. *592*, 1159-1162.

Montandon, G., Qin, W., Liu, H., Ren, J., Greer, J.J., and Horner, R.L. (2011). PreBötzinger complex neurokinin-1 receptor-expressing neurons mediate opioid-induced respiratory depression. J. Neurosci. *31*, 1292-1301.

Mustapic, S., Radocaj, T., Sanchez, A., Dogas, Z., Stucke, A.G., Hopp, F.A., Stuth, E.A., and Zuperku, E.J. (2010). Clinically relevant infusion rates of μ-opioid agonist remifentanil cause bradypnea in decerebrate dogs but not via direct effects in the pre-Bötzinger complex region. J. Neurophysiol. *103*, 409-418.

Navarrete-Opazo, A.A., Cook-Snyder, D.R., Miller, J.R., Callison, J.J., McCarthy, N., Palkovic, B., Stuth, E.A., Zuperku, E.J., and Stucke, A.G. (2020). Endogenous glutamatergic inputs to the Parabrachial Nucleus/Kölliker-Fuse Complex determine respiratory rate. Respir. Physiol. Neurobiol. *277*, 103401.

Niebert, M., Vogelgesang, S., Koch, U.R., Bischoff, A.M., Kron, M., Bock, N., and Manzke, T. (2011). Expression and function of serotonin 2A and 2B receptors in the mammalian respiratory network. PLoS One *6*, e21395.

Oertel, B., Felden, L., Tran, P., Bradshaw, M., Angst, M., Schmidt, H., Johnson, S., Greer, J., Geisslinger, G., and Varney, M. (2010). Selective antagonism of opioid-induced ventilatory depression by an ampakine molecule in humans without loss of opioid analgesia. Clin. Pharmacol. Ther. *87*, 204-211.

Oertel, B., Schneider, A., Rohrbacher, M., Schmidt, H., Tegeder, I., Geisslinger, G., and Lötsch, J. (2007). The partial 5-hydroxytryptamine1A receptor agonist buspirone does not antagonize morphine-induced respiratory depression in humans. Clin. Pharmacol. Ther. *81*, 59-68.

Palmiter, R.D. (2018). The parabrachial nucleus: CGRP neurons function as a general alarm. Trends Neurosci. *41*, 280-293.

Pattinson, K.T. (2008). Opioids and the control of respiration. Br. J. Anaesth. *100*, 747-758.

Prkic, I., Mustapic, S., Radocaj, T., Stucke, A.G., Stuth, E.A., Hopp, F.A., Dean, C., and Zuperku, E.J. (2012). Pontine mu-opioid receptors mediate bradypnea caused by intravenous remifentanil infusions at clinically relevant concentrations in dogs. J. Neurophysiol. *108*, 2430-2441.

Roozekrans, M., van der Schrier, R., Okkerse, P., Hay, J., McLeod, J.F., and Dahan, A. (2014). Two studies on reversal of opioid-induced respiratory depression by BK-channel blocker GAL021 in human volunteers. Anesthesiology *121*, 459-468.

Roth, B.L. (2016). DREADDs for Neuroscientists. Neuron *89*, 683-694.

Sanz, E., Bean, J.C., Carey, D.P., Quintana, A., and McKnight, G.S. (2019). RiboTag: ribosomal tagging strategy to analyze cell-type-specific mRNA expression in vivo. Curr. Protoc. Neurosci. *88*, e77.

Sanz, E., Yang, L., Su, T., Morris, D.R., McKnight, G.S., and Amieux, P.S. (2009). Cell-type-specific isolation of ribosome-associated mRNA from complex tissues. Proc. Natl. Acad. Sci. U.S.A. *106*, 13939-13944.

Saunders, S.E., and Levitt, E.S. (2020). Kölliker-Fuse/Parabrachial complex mu opioid receptors contribute to fentanyl-induced apnea and respiratory rate depression. Respir. Physiol. Neurobiol. *275*, 103388.

Skolnick, P. (2018). On the front lines of the opioid epidemic: rescue by naloxone. Eur. J. Pharmacol. *835*, 147-153.

Smith, J.C., Ellenberger, H.H., Ballanyi, K., Richter, D.W., and Feldman, J.L. (1991). Pre-Bötzinger complex: a brainstem region that may generate respiratory rhythm in mammals. Science *254*, 726-729.

Song, G., and Poon, C.S. (2009a). Lateral parabrachial nucleus mediates shortening of expiration and increase of inspiratory drive during hypercapnia. Respir. Physiol. Neurobiol. *165*, 9-12.

Song, G., and Poon, C.S. (2009b). Lateral parabrachial nucleus mediates shortening of expiration during hypoxia. Respir. Physiol. Neurobiol. *165*, 1-8.

Stucke, A.G., Miller, J.R., Prkic, I., Zuperku, E.J., Hopp, F.A., and Stuth, E.A. (2015). Opioid-induced respiratory depression is only partially mediated by the preBötzinger complex in young and adult rabbits in vivo. Anesthesiology *122*, 1288-1298.

Sugihara, G., May, R., Ye, H., Hsieh, C.-h., Deyle, E., Fogarty, M., and Munch, S. (2012). Detecting causality in complex ecosystems. Science *338*, 496-500.

Sugihara, G., and May, R.M. (1990). Nonlinear forecasting as a way of distinguishing chaos from measurement error in time series. Nature *344*, 734-741.

Tokita, K., Inoue, T., and Boughter, J.D. (2009). Afferent connections of the parabrachial nucleus in C57BL/6J mice. Neuroscience *161*, 475-488.

van der Schier, R., Roozekrans, M., van Velzen, M., Dahan, A., and Niesters, M. (2014). Opioid-induced respiratory depression: reversal by non-opioid drugs. F1000Prime Rep *6*.

Vardy, E., Robinson, J.E., Li, C., Olsen, R.H., DiBerto, J.F., Giguere, P.M., Sassano, F.M., Huang, X.-P., Zhu, H., and Urban, D.J. (2015). A new DREADD facilitates the multiplexed chemogenetic interrogation of behavior. Neuron *86*, 936-946.

Varga, A.G., Reid, B.T., Kieffer, B.L., and Levitt, E.S. (2020). Differential impact of two critical respiratory centres in opioid-induced respiratory depression in awake mice. The Journal of Physiology *598*, 189-205.

Wei, A.D., and Ramirez, J.-M. (2019). Presynaptic mechanisms and KCNQ potassium channels modulate opioid depression of respiratory drive. Front. Physiol. *10*, 1407.

Whitney, H. (1936). The imbedding of manifolds in families of analytic manifolds. Ann. Math., 865-878.

Yokota, S., Kaur, S., VanderHorst, V.G., Saper, C.B., and Chamberlin, N.L. (2015). Respiratory-related outputs of glutamatergic, hypercapnia-responsive parabrachial neurons in mice. J. Comp. Neurol. *523*, 907-920.

Figure 3.1. MOR signaling in the PBL mediates morphine-induced respiratory depression

(A) Schematics of breathing monitoring in awake mice with whole-body plethysmography (WBP) before and after systemic morphine injection (refer to C, D, I, K). Grey shade indicates the 10-min WBP recording, and yellow shade indicates the 1-min episode used for data analysis.

(B–D) *Oprm1*$^{+/+}$, *Oprm1*$^{Cre/+}$, and *Oprm1*$^{Cre/Cre}$ mice (B) displayed different breathing patterns (C) and rate changes (D) in response to systemic morphine injection.

(E) Schematics of breathing monitoring in anesthetized mice with inductance plethysmography, during systemic morphine injection and PBL-specific blockade of MOR signaling. Yellow shade indicates the 2-min plethysmography recording before morphine, after morphine, and after naloxone/saline injections; purple shade indicates the naloxone/saline injection which lasts ~4 minutes. Onset, histology of the co-injected FluoSpheres in the PBL. Scp, superior cerebellar peduncle.

(F) Representative plethysmographs from naloxone (NLX) and saline (SAL) injected groups before morphine, after morphine, and after drug injections into the PBL.

(G) Injecting naloxone (n = 5), but not saline (n = 5) into the PBL rescued morphine-induced respiratory depression.

(H) Schematics of PBL-specific knockout of the *Oprm1* gene by stereotaxically injecting AAV-Cre-GFP into the PBL of the *Oprm1*$^{fl/fl}$ mice.

(I) PBL-specific Oprm1 knockout (n = 9) significantly attenuated OIRD compared to the GFP injected control group (n = 9) after systemic morphine injection.

(J) Schematics of PBL-specific rescue of the *Oprm1* gene in *Oprm1*-null background by stereotaxically injecting AAV-DIO-hMOR into the PBL of the *Oprm1*$^{Cre/Cre}$ mice.

(K) Mice with PBL-specific rescue of *Oprm1* (n = 6) displayed OIRD phenotype, whereas eYFP injected control group (n = 6) remained insensitive after systemic morphine injection. Morphine doses were determined according to different genetic background or experimental conditions: 10 mg/kg (I); 40 mg/kg (C, D, K); 80 mg/kg (F, G). Data are presented as mean ± SEM. Statistical tests, Two-way ANOVA with Bonferroni's multiple comparison post-hoc test (D, G, I, K). ns, not significant; *, $p < 0.05$; **, $p < 0.01$; ***, $p < 0.001$; ****, $p < 0.0001$. Scale bar, 1s (C, F) or 200 μm (E, H, J). See also Figure S3.1, S3.2.

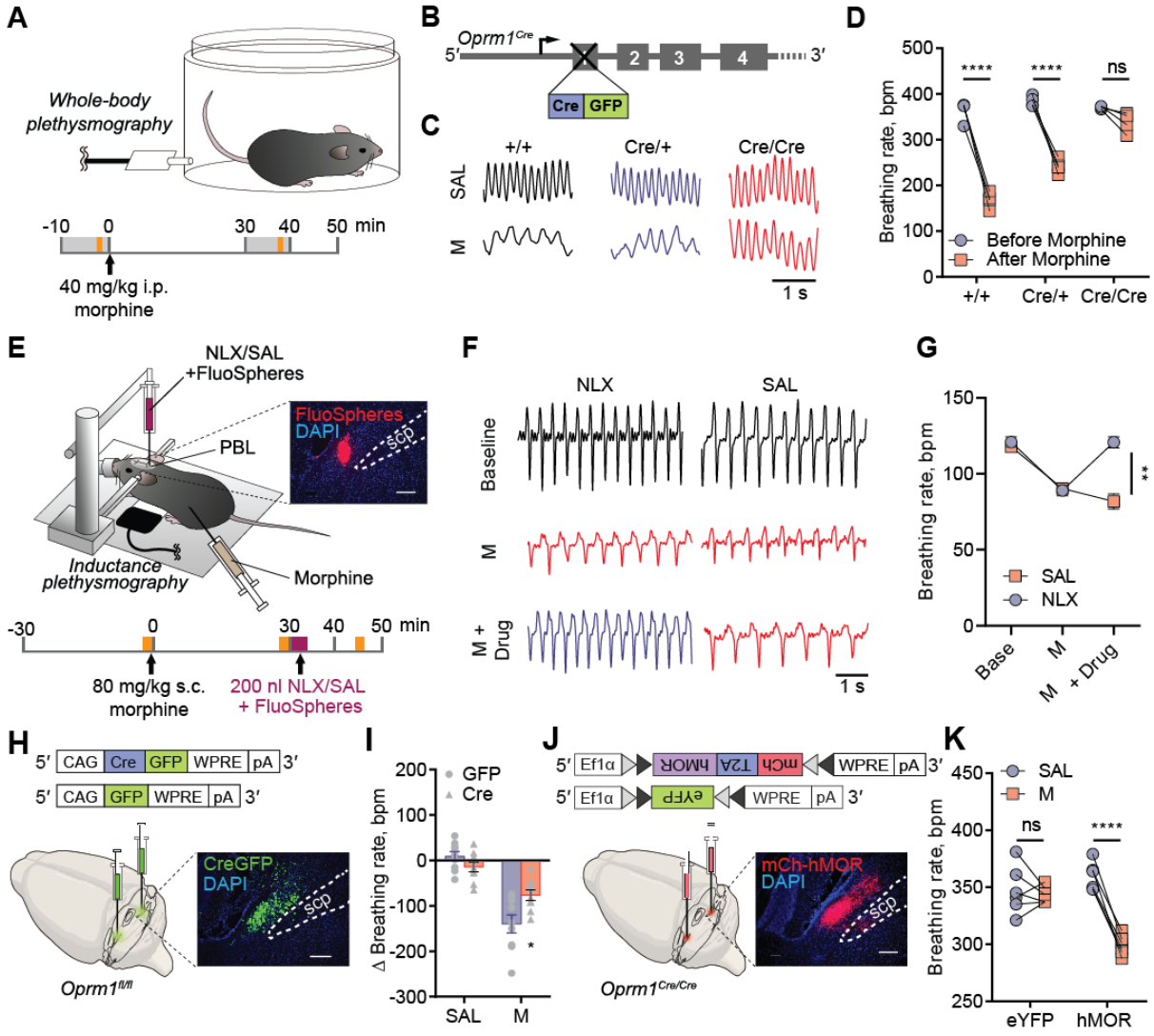
A
Whole-body plethysmography
-10 0 30 40 50 min
40 mg/kg i.p. morphine
B
Oprm1Cre
5′
2 3 4
3′
Cre GFP
C
+/+
Cre/+
Cre/Cre
SAL
M
1 s
D
Breathing rate, bpm
500 400 300 200 100 0
**** **** ns
Before Morphine
After Morphine
+/+ Cre/+ Cre/Cre
E
NLX/SAL +FluoSpheres
PBL
FluoSpheres DAPI
scp
Inductance plethysmography
Morphine
-30 0 30 40 50 min
80 mg/kg s.c. morphine
200 nl NLX/SAL + FluoSpheres
F
NLX
SAL
Baseline
M
M + Drug
1 s
G
Breathing rate, bpm
150 100 50 0
**
SAL
NLX
Base M M + Drug
H
5′ CAG Cre GFP WPRE pA 3′
5′ CAG GFP WPRE pA 3′
CreGFP DAPI
scp
Oprm1fl/fl
I
Δ Breathing rate, bpm
200 100 0 -100 -200 -300
GFP
Cre
SAL M
J
5′ Ef1α hMOR T2A mCh WPRE pA 3′
5′ Ef1α eYFP WPRE pA 3′
mCh-hMOR DAPI
scp
Oprm1Cre/Cre
K
Breathing rate, bpm
450 400 350 300 250
SAL
M
ns ****
eYFP hMOR

Figure 3.2. Morphine disrupts the tight correlation between PBL^{Oprm1} neuronal activity and respiratory rate

(A) Schematics of simultaneous recording of respiration and PBL^{Oprm1} calcium activity with a thermistor sensor (implanted in the nasal cavity) and fiber photometry.

(B) The genetically encoded calcium indicator, jGCaMP7s, was specifically expressed in the PBL^{Oprm1} neurons by stereotaxic injection of AAV-DIO-jGCaMP7s into the PBL of the *Oprm1*$^{Cre/+}$ mice.

(C) Time-matched traces of PBL^{Oprm1} activity and breathing rate as calculated from the thermistor sensor.

(D, F, H, J) Simultaneously recorded PBL^{Oprm1} calcium activity and respiratory rate before and after systemic saline or morphine (40 mg/kg) injection.

(E, G, I, K) Cross-correlogram of calcium signal and respiratory rate in the pre-saline, post-saline, pre-morphine, and post-morphine groups (n = 4).

(L) Morphine injection significantly depressed respiratory rate (n = 4), whereas saline injection (n = 4) did not significantly affect the respiratory rate.

(M–N) Normalized distribution of breathing rate before and after saline (M) and morphine (N) injections (n = 4). (O) The number of calcium peaks was significantly decreased after morphine injection (n = 4) compared to saline injection (n = 4).

(P–Q) Normalized distribution of calcium signals before and after saline (P) and morphine (Q) injections (n = 4). Data are presented as mean ± SEM. Statistical tests, Unpaired t-test (O) or Two-way ANOVA with Bonferroni's multiple comparison post-hoc test (L, M, N, P, Q). ns, not significant; *, $p < 0.05$; **, $p < 0.01$; ****, $p < 0.0001$. Scale bar, 200 μm. See also Figure S3.3, S3.4.

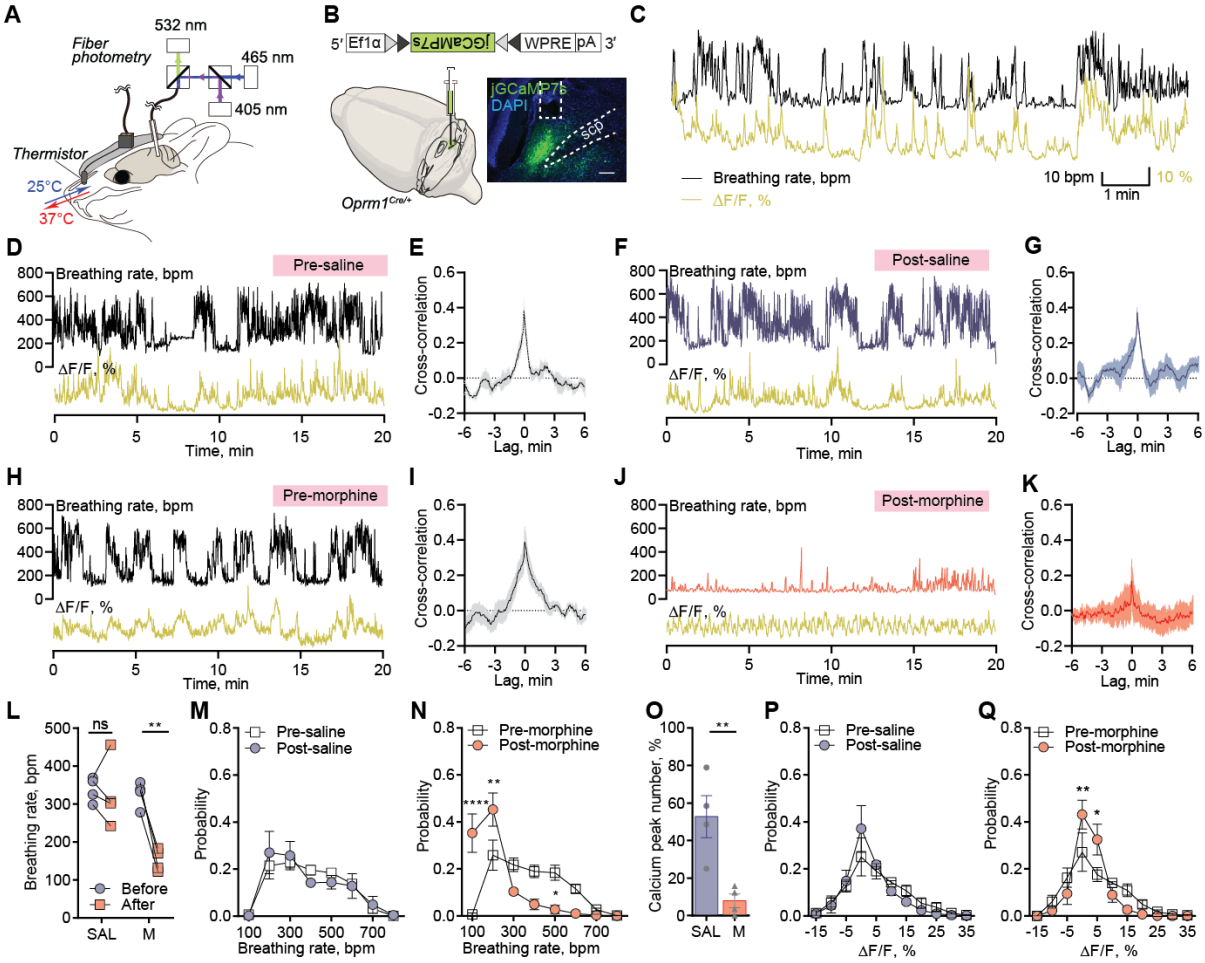
A
532 nm
Fiber photometry
465 nm
405 nm
Thermistor
25°C
37°C
B
5′ Ef1α jGCaMP7s WPRE pA 3′
jGCaMP7s
DAPI
SCp
Oprm1Cre/+
C
Breathing rate, bpm
ΔF/F, %
10 bpm
10 %
1 min
D
Pre-saline
Breathing rate, bpm
ΔF/F, %
Time, min
E
Cross-correlation
Lag, min
F
Post-saline
Breathing rate, bpm
ΔF/F, %
Time, min
G
Cross-correlation
Lag, min
H
Pre-morphine
Breathing rate, bpm
ΔF/F, %
Time, min
I
Cross-correlation
Lag, min
J
Post-morphine
Breathing rate, bpm
ΔF/F, %
Time, min
K
Cross-correlation
Lag, min
L
ns
**
Breathing rate, bpm
Before
After
SAL
M
M
Pre-saline
Post-saline
Probability
Breathing rate, bpm
N
Pre-morphine
Post-morphine
Probability
Breathing rate, bpm
O
**
Calcium peak number, %
SAL
M
P
Pre-saline
Post-saline
Probability
ΔF/F, %
Q
Pre-morphine
Post-morphine
Probability
ΔF/F, %

Figure 3.3. Inhibition of PBL^{Oprm1} neurons mimics OIRD, and chemogenetic activation of PBL^{Oprm1} neurons rescues OIRD

(A) Schematics of mimicking OIRD through PBL^{Oprm1} inhibition using an inhibitory κ-opioid receptor-derived DREADD (KORD). Here, AAV-DIO-KORD-mCitrine is stereotaxically injected into the bilateral PBL of *Oprm1*$^{Cre/Cre}$ mice to express in the PBL^{Oprm1} neurons.

(B) Salvinorin B (SALB, 7.5 mg/kg) injection significantly decreased respiratory rate compared to the DMSO control in the KORD-expressing mice (n = 11). In contrast, no changes were observed in eYFP-expressing mice (n = 8).

(C) Schematics of rescuing OIRD through PBL^{Oprm1} activation by an excitatory DREADD, hM3Dq. Here, AAV-DIO-hM3Dq-mCherry was expressed in the bilateral PBL of *Oprm1*$^{Cre/+}$ mice.

(D) Activation of PBL^{Oprm1} neurons by injecting Clozapine N-oxide (CNO, 5 mg/kg) rescued the morphine-induced respiratory depression (40 mg/kg) to control levels in the hM3Dq-expressing group (n = 6), but not the eYFP-expressing group (n = 5).

(E–F) Representative plethysmograph and quantitative analysis depicting OIRD rescued by CNO injection in the hM3Dq-expressing group (n = 7), but not in the eYFP-expressing group (n = 5). Statistical tests, Two-way ANOVA with Bonferroni's multiple comparison post-hoc test. ns, not significant; ****, $p < 0.0001$. Scale bar, 200 μm. See also Figure S3.5.

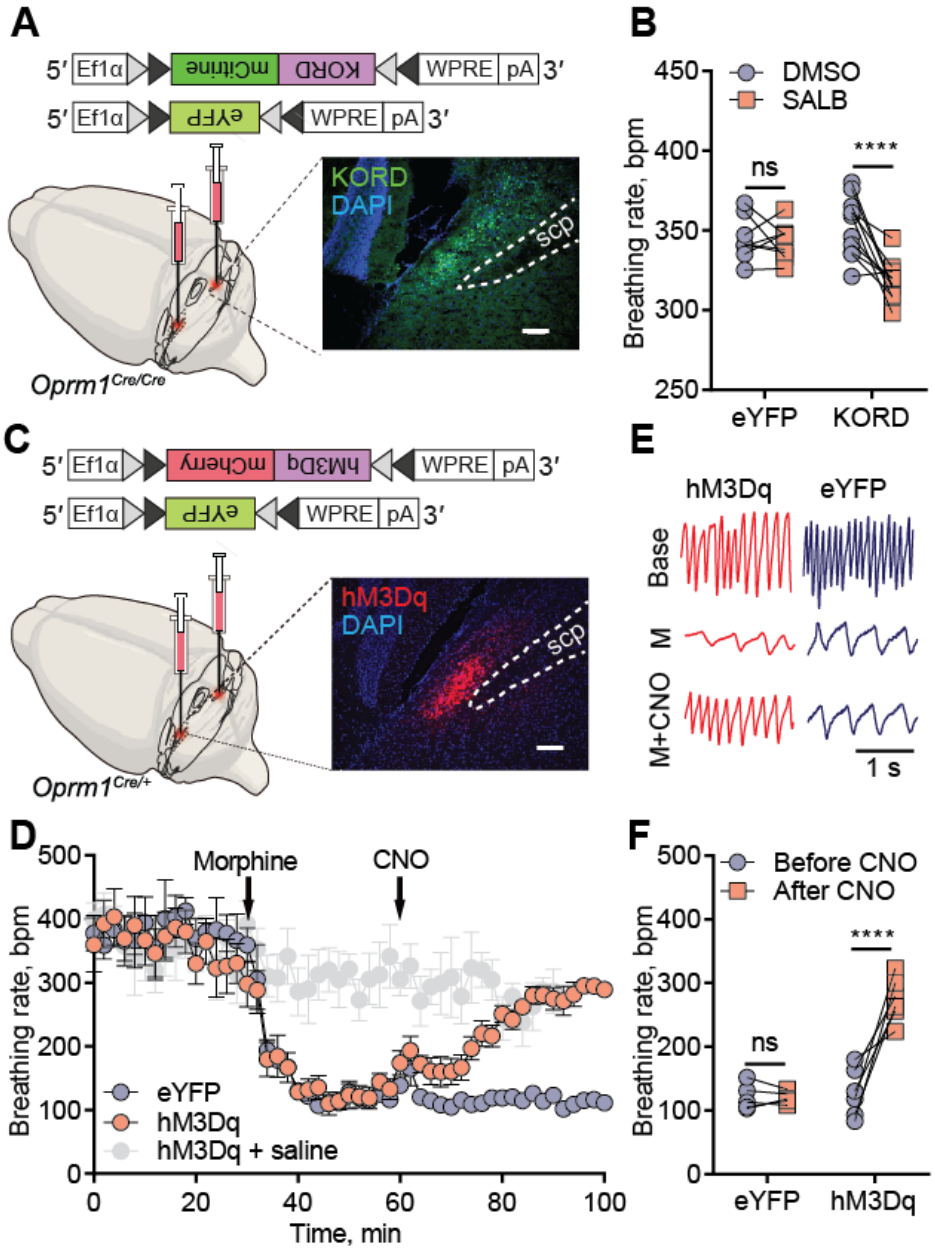
A
5′ Ef1α mCitrine KORD WPRE pA 3′
5′ Ef1α eYFP WPRE pA 3′
KORD
DAPI
scp
Oprm1Cre/Cre
B
DMSO
SALB
Breathing rate, bpm
450
400
350
300
250
ns
****
eYFP
KORD
C
5′ Ef1α mCherry hM3Dq WPRE pA 3′
5′ Ef1α eYFP WPRE pA 3′
hM3Dq
DAPI
scp
Oprm1Cre/+
E
hM3Dq
eYFP
Base
M
M+CNO
1 s
D
Morphine
CNO
Breathing rate, bpm
500
400
300
200
100
0
eYFP
hM3Dq
hM3Dq + saline
0
20
40
60
80
100
Time, min
F
Before CNO
After CNO
Breathing rate, bpm
500
400
300
200
100
0
ns
****
eYFP
hM3Dq

Figure 3.4. Rescue of OIRD through PBL^{Oprm1} stimulation via receptors identified by RiboTag RNA sequencing

(A) Schematics of obtaining PBL^{Oprm1} active transcriptome. *Oprm1*$^{Cre/Cre}$ mice were crossed with RiboTag mice, which express hemagglutinin-tagged ribosomal protein L22 (*Rpl22*^{HA}) in a Cre-dependent manner. After collecting the PBL, active mRNAs bound to the *Rpl22*^{HA} were isolated with anti-HA antibody-mediated ribosome pull-down and sequenced.

(B) Immunohistochemistry of the PBL region of the *Oprm1*^{Cre}::*Rpl22*^{HA} mice with anti-GFP and anti-HA antibodies showed that the Cre:GFP and Rpl22^{HA} were co-expressed in PBL^{Oprm1} neurons.

(C) Fourteen GPCR mRNAs (magenta and green) were enriched more than three-fold in PBL^{Oprm1} neurons compared with non-*Oprm1* neurons in the PBL. Conventional parabrachial markers (dark blue), such as *Foxp2*, *Tac1*, and *Adcyap1* genes were enriched in PBL^{Oprm1} neurons, but not *Pdyn* and *Calca*.

(D–E) Schematics of rescuing OIRD through artificial stimulation of receptors expressed on PBL^{Oprm1} neurons by PBL-specific injection of the agonists. Yellow shade indicates the 2-min plethysmography recording before morphine (80 mg/kg), after morphine, and after drug/CTB injections; green shade indicates the drug injection which lasts ~400 sec. Onset, histology of cholera toxin subunit B (CTB)-555 for marking the injection site.

(F) Breathing rate decreased upon systemic morphine injection and rescued by PBL-specific injection of the agonists of 5-HT$_{2A}$, CCK$_1$R, and NK$_1$R. For the list of pharmacological agents, see **Table S3.1**. Statistical tests, RM One-way ANOVA with Tukey's multiple comparison post-hoc test, ns, not significant; *, $p < 0.05$; **, $p < 0.01$; ***, $p < 0.001$, ****, $p < 0.0001$. Scale bar, 100 μm (B) or 200 μm (D). See also Figure S3.6.

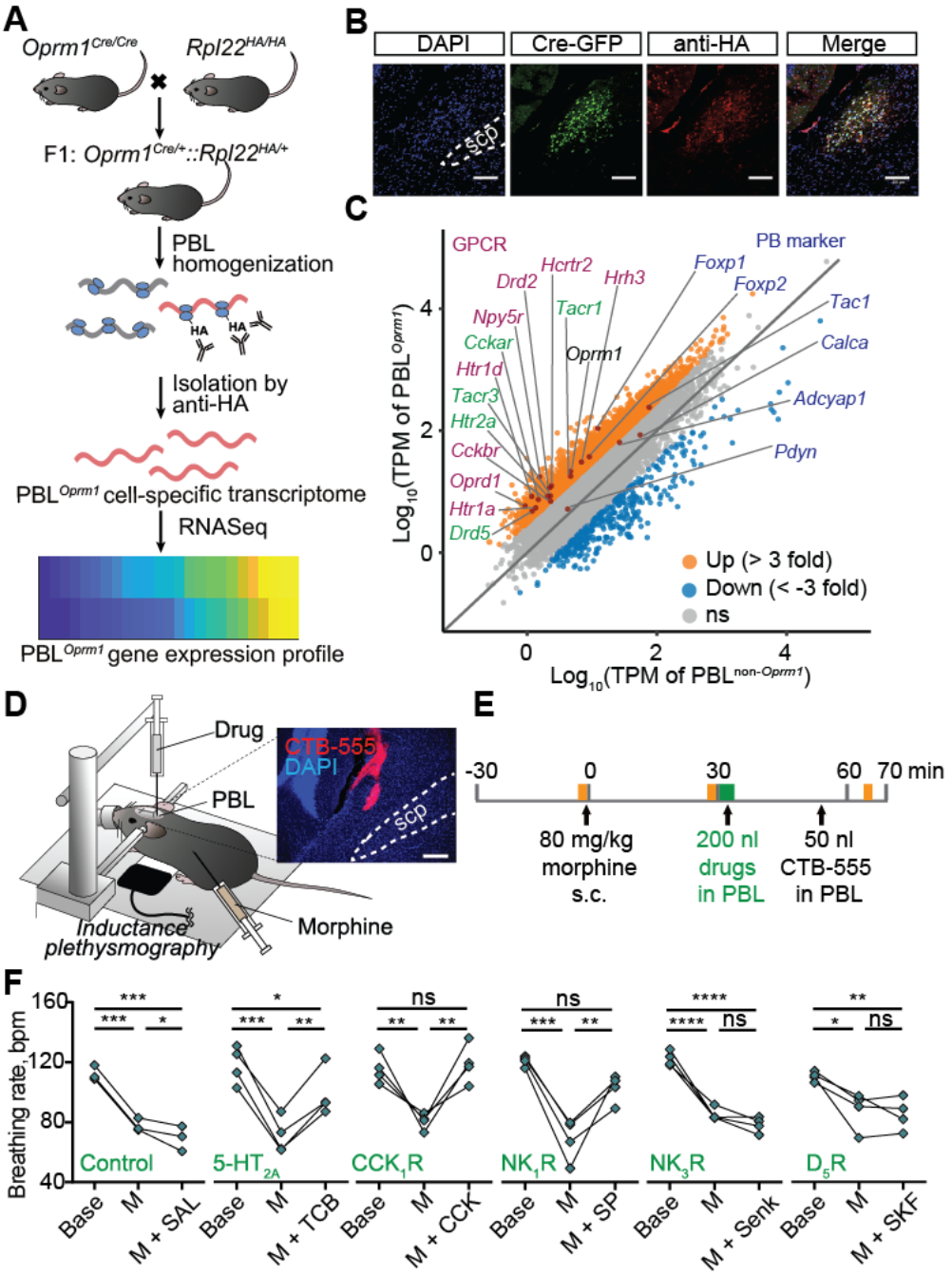
A
Oprm1Cre/Cre
Rpl22HA/HA
F1: Oprm1Cre/+::Rpl22HA/+
PBL homogenization
HA
HA
Isolation by anti-HA
PBLOprm1 cell-specific transcriptome
RNASeq
PBLOprm1 gene expression profile
B
DAPI
Cre-GFP
anti-HA
Merge
scp
C
GPCR
PB marker
Drd2
Hcrtr2
Hrh3
Foxp1
Foxp2
Tac1
Npy5r
Tacr1
Cckar
Oprm1
Calca
Htr1d
Tacr3
Adcyap1
Htr2a
Cckbr
Pdyn
Oprd1
Htr1a
Drd5
Up (> 3 fold)
Down (< -3 fold)
ns
Log10(TPM of PBLOprm1)
Log10(TPM of PBLnon-Oprm1)
D
Drug
PBL
CTB-555
DAPI
scp
Morphine
Inductance plethysmography
E
-30
0
30
60
70 min
80 mg/kg morphine s.c.
200 nl drugs in PBL
50 nl CTB-555 in PBL
F
Breathing rate, bpm
Control
5-HT2A
CCK1R
NK1R
NK3R
D5R
Base
M
M + SAL
M + TCB
M + CCK
M + SP
M + Senk
M + SKF
ns

Figure S3.1. Characterization of the *Oprm1*^{Cre} mouse line and PBL^{Oprm1} neurons. Related to Figure 3.1

(A) RNA *in situ* hybridization and quantification of the colocalization for *Oprm1* and *Cre* mRNAs in the PBL of *Oprm1*$^{Cre/+}$ mice (n = 902 cells from 3 animals). Arrowheads, double-labeled cells. Scale bar, 10 μm.

(B) RNA *in situ* hybridization and quantification of the colocalization for *Oprm1*, *Slc17a6* (encoding VGLUT2), and *Slc32a1* (encoding VGAT) mRNAs in the PBL of wild type mice (n = 1552 and 1431 cells from 3 animals). Arrowheads, *Oprm1*$^{+}$ / *Slc17a6*$^{+}$ cells; asterisks, *Oprm1*$^{-}$ / *Slc32a1*$^{+}$ cells. Scale bar, 50 μm.

(C) Example histology from *Oprm1*^{Cre}*::*Ai14 double transgenic mice showing tdTomato expression in the PBL and KF under the same microscope settings. Anatomical landmarks for PBL: stcv, ventral spinocerebellar tract; scp, superior cerebellar peduncle; mcp, middle cerebellar peduncle. Scale bar, 200 μm.

(D) *Oprm1*^{Cre} mice do not exhibit baseline breathing differences compared to the wild type mice. Breathing rate before and after saline injection did not display considerable differences across genotypes and within each genotype. Two-way ANOVA with Bonferroni's multiple comparison post-hoc test. ns, not significant.

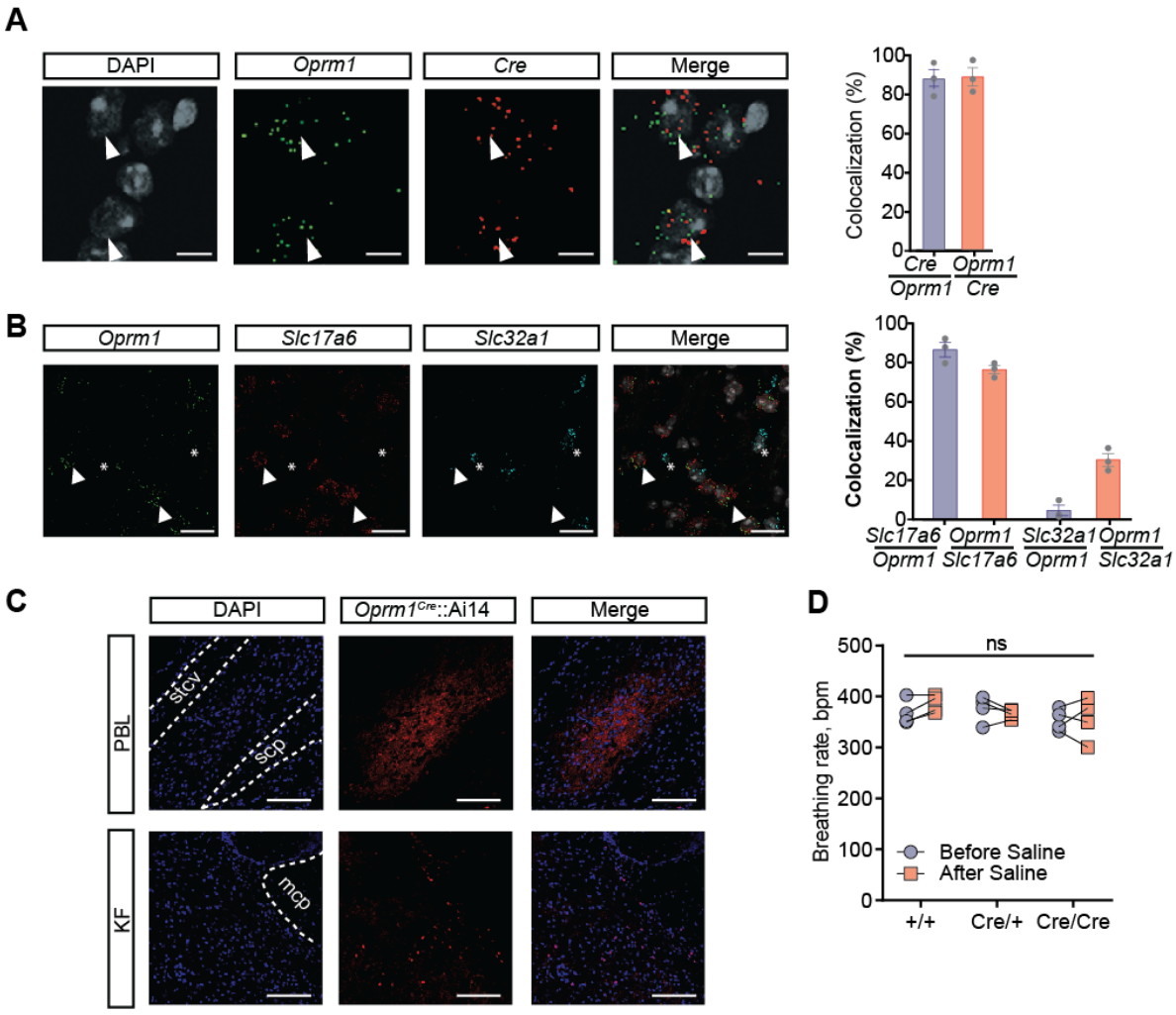
A
DAPI
Oprm1
Cre
Merge
Colocalization (%)
100
80
60
40
20
0
Cre
Oprm1
Oprm1
Cre
B
Oprm1
Slc17a6
Slc32a1
Merge
Colocalization (%)
Slc17a6
Oprm1
Oprm1
Slc17a6
Slc32a1
Oprm1
Oprm1
Slc32a1
C
DAPI
Oprm1Cre::Ai14
Merge
PBL
KF
sfcv
scp
mcp
D
ns
Breathing rate, bpm
500
400
300
200
100
0
Before Saline
After Saline
+/+
Cre/+
Cre/Cre

Figure S3.2. MOR signaling in the PBL is indispensable for OIRD. Related to Figure 3.1

(A) Whole-body plethysmography measured respiratory parameters before and after systemic injection of saline and morphine, after conditional ablation (B) and rescue (D) of the MOR signaling in the PBL.

(B) Example plethysmograph after saline and morphine injections into the *Oprm1*$^{fl/fl}$ mice expressing AAV-GFP and AAV-Cre-GFP in the PBL.

(C) Confirmation of MOR deletion by MOR immunohistochemistry after stereotaxic injection of AAV-Cre-GFP and control AAV-GFP into the PBL of the *Oprm1*$^{fl/fl}$ mice. Scale bar, 100 μm.

(D) Example plethysmograph after saline and morphine injections into the *Oprm1*$^{Cre/Cre}$ mice expressing AAV-DIO-eYFP and AAV-DIO-hMOR in the PBL.

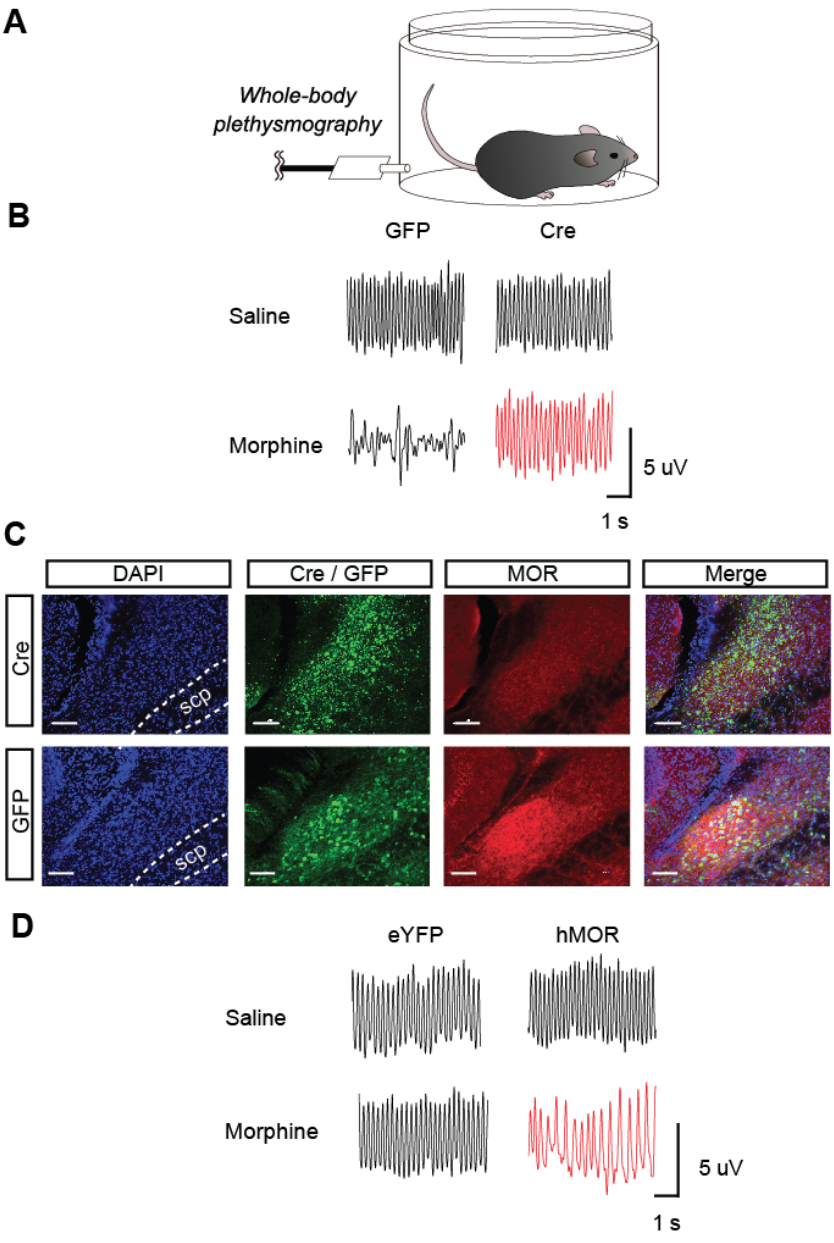
A
Whole-body
plethysmography
B
GFP
Cre
Saline
Morphine
5 uV
1 s
C
DAPI
Cre / GFP
MOR
Merge
Cre
GFP
scp
scp
D
eYFP
hMOR
Saline
Morphine
5 uV
1 s

Figure S3.3. Morphine effect on locomotor activity. Related to Figure 3.2

(A) Locomotor activity of *Oprm1*$^{Cre/+}$ mice after morphine (40 mg/kg, i.p.) or saline injection was measured in the open field.

(B) Systemic morphine injection increased locomotor activity in *Oprm1*$^{Cre/+}$ mice. Paired t-test, **, $p < 0.01$.

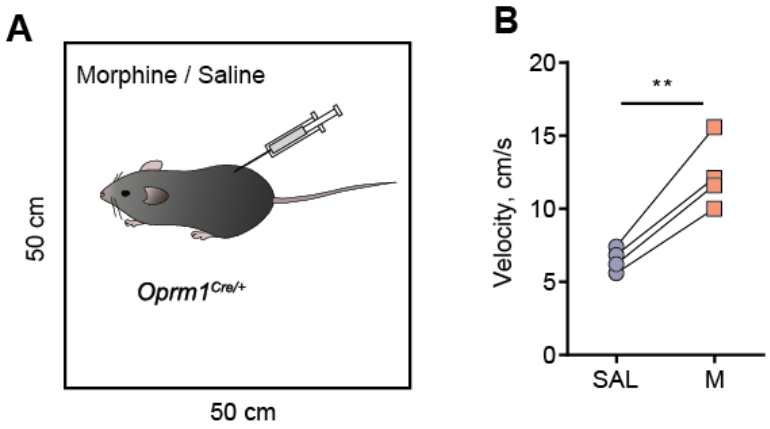
A
Morphine / Saline
50 cm
Oprm1Cre/+
50 cm
B
Velocity, cm/s
20
15
10
5
0
**
SAL
M

Figure S3.4. Morphine eliminated the breathing predictor. Related to Figure 3.2

Convergent cross-mapping (CCM) prediction of breathing rate using calcium activity as inputs before and after saline (0.9%, i.p., A and B) and morphine (40 mg/kg, i.p., C and D) injection.

(A) After saline injection, the predicted and observed breathing rate traces followed closely with each other during the 10-min example.

(B) Model predictability increased with the sample size before and after saline injection (n = 4).

(C) After morphine injection, the predicted and observed breathing rate traces no longer matched with each other.

(D) Model predictability increased with the sample size before morphine injection, but the relationship was completely abolished after morphine injection (n = 4).

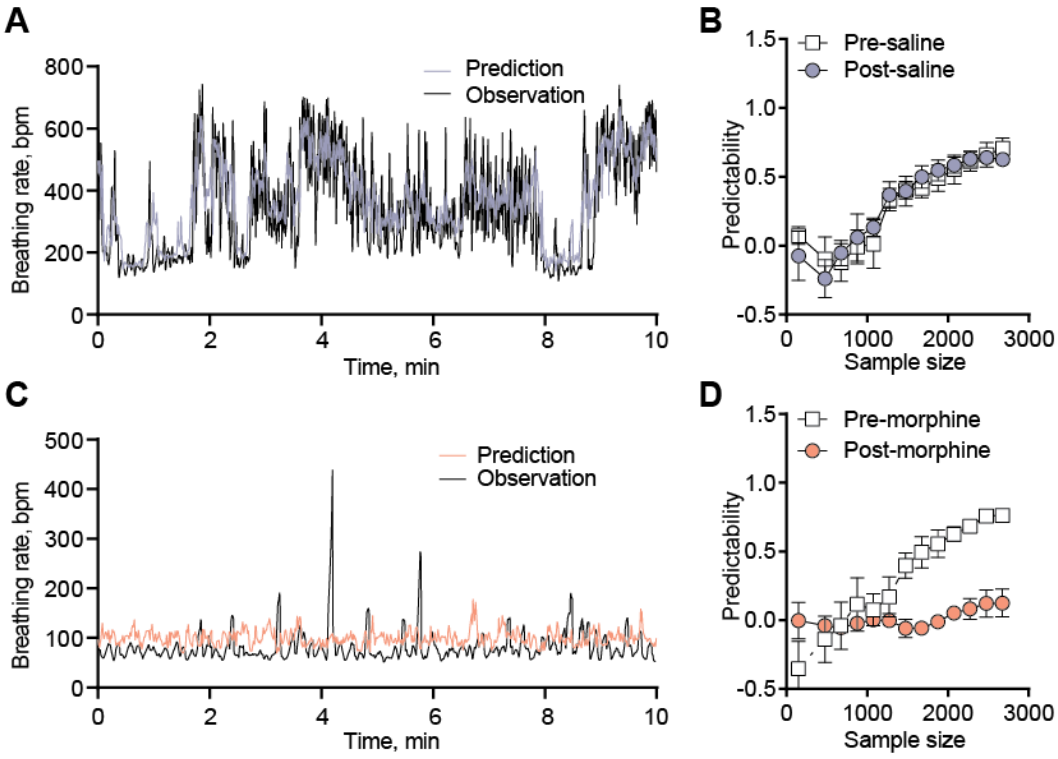
A
Prediction
Observation
Breathing rate, bpm
800
600
400
200
0
0
2
4
6
8
10
Time, min
B
Pre-saline
Post-saline
Predictability
1.5
1.0
0.5
0.0
-0.5
0
1000
2000
3000
Sample size
C
Prediction
Observation
Breathing rate, bpm
500
400
300
200
100
0
0
2
4
6
8
10
Time, min
D
Pre-morphine
Post-morphine
Predictability
1.5
1.0
0.5
0.0
-0.5
0
1000
2000
3000
Sample size

Figure S3.5. Chemogenetic activation of PBL^{Oprm1} neurons rescues OIRD. Related to Figure 3.3

(A) Whole-body plethysmography was used to measure respiratory parameters before and after systemic injection of DMSO and SALB in the *Oprm1*$^{Cre/Cre}$ mice expressing AAV-DIO-eYFP and AAV-DIO-KORD in PBL^{Oprm1} neurons.

(B) Example plethysmograph after DMSO and 7.5 mg/kg SALB injections in eYFP and KORD groups. KORD-expressing animals displayed a slower respiratory rate after SALB injection compared to other groups.

(C) Respiratory amplitude was not significantly changed before and after SALB injection, in both eYFP (n = 8) and KORD (n = 11)-expressing animals. Two-way ANOVA with Bonferroni's multiple comparison post-hoc test, ns, not significant.

(D) Thermistor-based plethysmography was used for measuring respiration before and after systemic injection of 40 mg/kg morphine and CNO in the *Oprm1*$^{Cre/+}$ mice expressing AAV-DIO-eYFP and AAV-DIO-hM3Dq in PBL^{Oprm1} neurons.

(E) Respiratory amplitude was not significantly changed before and after CNO injection, in both eYFP (n = 5) and hM3Dq-expressing animals (n = 6). Although there was a trend of increase in the hM3Dq group, it failed to reach statistical significance. Two-way ANOVA with Bonferroni's multiple comparison post-hoc tests, ns, not significant.

(F) Activation of PBL^{Oprm1} neurons by injecting CNO (5 mg/kg, i.p.) in the hM3Dq-expressing group (n = 6) completely rescued the minute volume to baseline level after morphine-induced respiratory depression, but not in eYFP-expressing group (n = 4).

(G) Quantitative analysis of F showing CNO injection significantly increased the minute volume in the hM3Dq-expressing group (n = 6), whereas failed to rescue in the eYFP-expressing group (n = 4). Two-way ANOVA with Bonferroni's multiple comparison post-hoc test. **, $p < 0.01$.

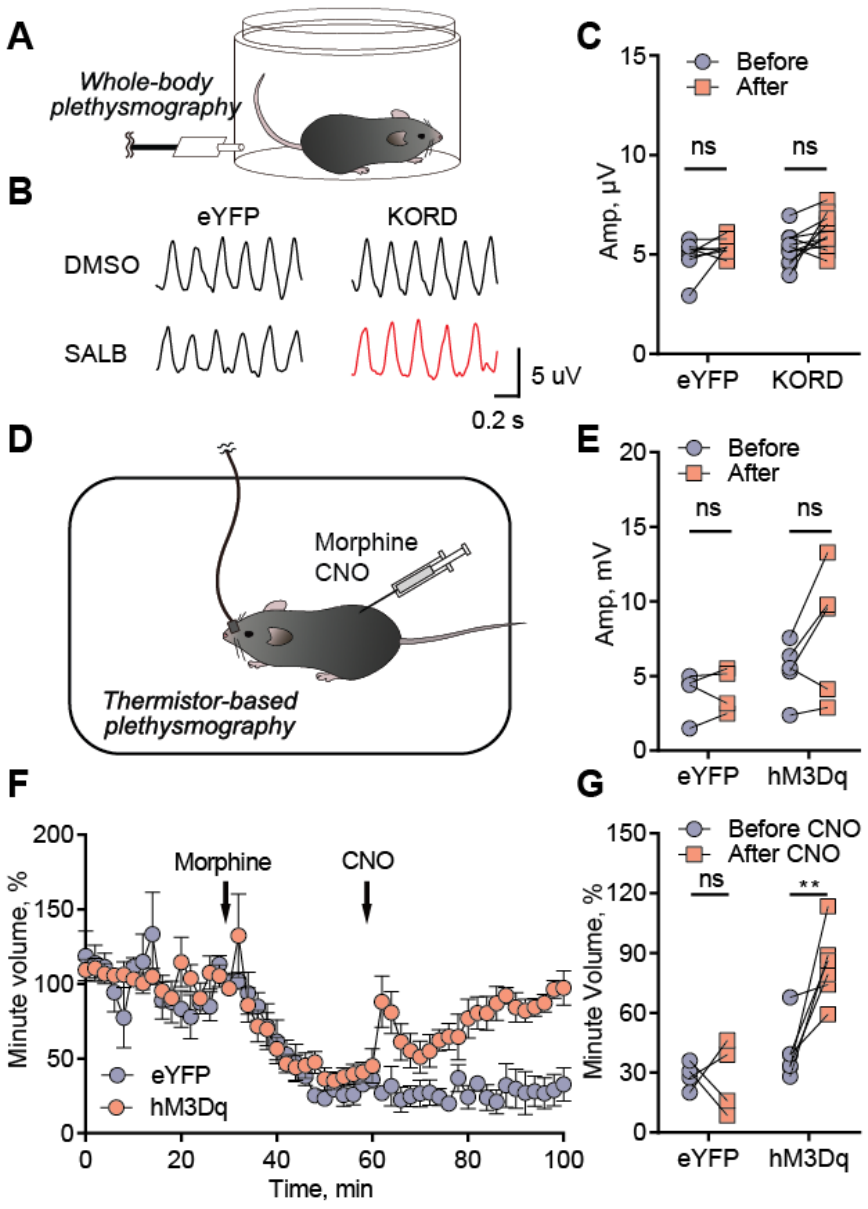
A
Whole-body plethysmography
B
eYFP
KORD
DMSO
SALB
5 uV
0.2 s
C
Before
After
ns
ns
Amp, µV
eYFP
KORD
D
Morphine
CNO
Thermistor-based plethysmography
E
Before
After
ns
ns
Amp, mV
eYFP
hM3Dq
F
Morphine
CNO
Minute volume, %
eYFP
hM3Dq
Time, min
G
Before CNO
After CNO
ns
**
Minute Volume, %
eYFP
hM3Dq

Figure S3.6. Rescuing of OIRD by activating endogenous GPCRs expressed on PBL^{Oprm1} neurons. Related to Figure 3.4

(A) RNA *in situ* hybridization confirms the co-expression of mRNA of *Oprm1* and five selected GPCRs, *Htr2a*, *Cckar*, *Tacr1*, *Tacr3*, and *Drd5*, in the wild type mice. Arrowheads, double-labeled cells. Scale bar, 50 μm.

(B) Quantification of RNA *in situ* hybridization showing the colocalization of *Oprm1* and selective GPCR genes in the PBL of wild type mice (770, 539, 836, 657, 431 cells for *Htr2a*, *Cckar*, *Tacr1*, *Tacr3*, and *Drd5*, respectively).

(C–D) Normalized breathing rate (C) and amplitude (D) before morphine injection (Baseline), 30 minutes after morphine injection (80 mg/kg, s.c., M), and 30 minutes after drug injection into the PBL (M + Drug), for all six drugs tested. Large variations in amplitude are due to the technical limitations of the piezoelectric sensor since its location is subjective to the slight movements of the animal's body. Paired t-test, *, $p < 0.05$; **, $p < 0.01$.

(E) Example plethysmograph showing the breathing rhythm changes at each stage of the experiment. Note the decreased breathing rate after morphine injection and increased breathing rate after TCB-2, CCK8S, and SP injections. The exact shape of the plethysmograph varies due to the placement of the piezoelectric sensor.

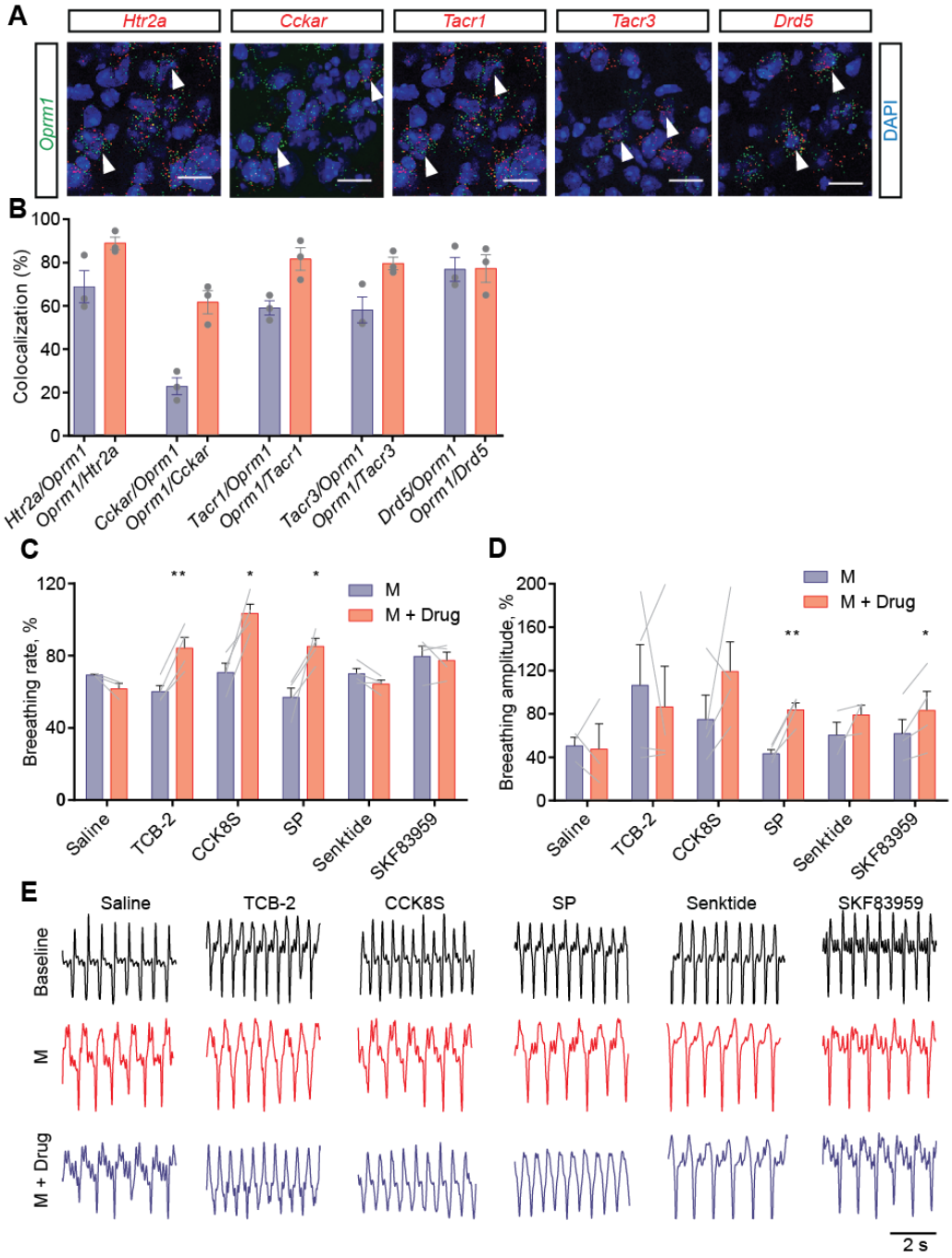
A
Htr2a
Cckar
Tacr1
Tacr3
Drd5
Oprm1
DAPI
B
Colocalization (%)
100
80
60
40
20
0
Htr2a/Oprm1
Oprm1/Htr2a
Cckar/Oprm1
Oprm1/Cckar
Tacr1/Oprm1
Oprm1/Tacr1
Tacr3/Oprm1
Oprm1/Tacr3
Drd5/Oprm1
Oprm1/Drd5
C
Breathing rate, %
120
80
40
0
M
M + Drug
**
*
*
Saline
TCB-2
CCK8S
SP
Senktide
SKF83959
D
Breathing amplitude, %
200
160
120
80
40
0
M
M + Drug
**
*
Saline
TCB-2
CCK8S
SP
Senktide
SKF83959
E
Saline
TCB-2
CCK8S
SP
Senktide
SKF83959
Baseline
M
M + Drug
2 s

Figure S3.7. Summary of the current study

PBL^{Oprm1} neurons are critical players in OIRD pathogenesis and promising therapeutic targets for treating OIRD. In intact mice, inhibition of PBL^{Oprm1} neurons through G_i-coupled GPCRs via endogenous MOR (mMOR), human MOR (hMOR), and KOR-derived DREADD (KORD) leads to respiratory depression. In contrast, activation of these neurons via artificial (hM3Dq) or endogenous $G_{q/s}$-coupled GPCRs (*Htr2a*, *Cckar*, *Tacr1*) rescues OIRD. Artificial GPCRs are marked with asterisks. Created with BioRender.com.

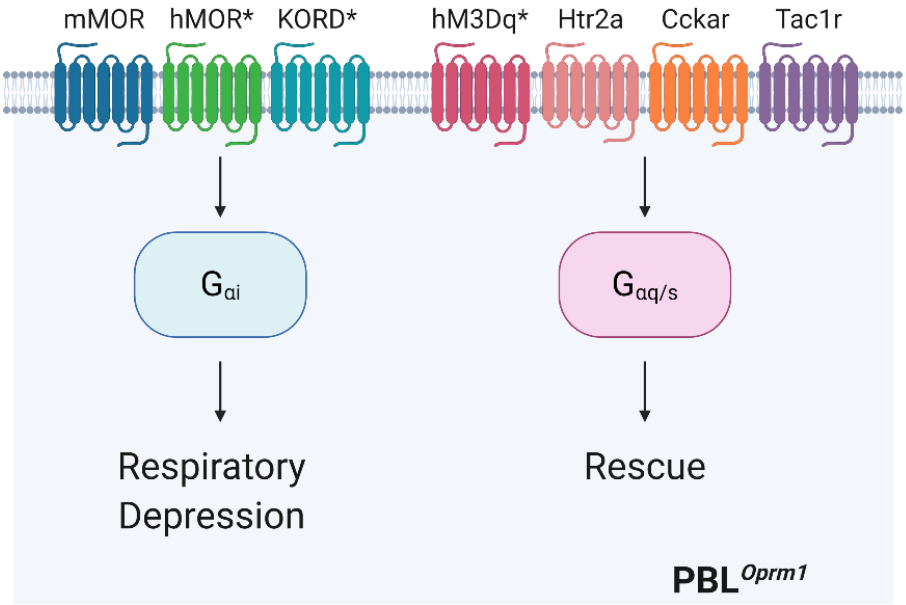
mMOR
hMOR*
KORD*
hM3Dq*
Htr2a
Cckar
Tac1r
$G_{\alpha i}$
$G_{\alpha q/s}$
Respiratory Depression
Rescue
PBL Oprm1

Table S3.1. List of pharmacological agents used in the current study

Drug Name	**Receptor (Gene)**	**Receptor Family**	**Concentration**	**Solvent**	**Company**
Naloxone	MOR (*Oprm1*)	Gi	0.4 mg/mL (i.c., intracranial)	0.9% saline	Somerset Therapeutics
Morphine	MOR (*Oprm1*)	Gi	80 mg/kg (s.c., for anesthesia experiments); 10 mg/kg (i.p., for PBL-specific *Oprm1* knockout); 40 mg/kg (i.p., for all other experiments)	0.9% saline	Spectrum Chemical
Salvinorin B (SALB)	KORD	Gi	7.5 mg/kg (i.p.)	0.9% saline containing 10% DMSO	Cayman Chemical
Clozapine-N-oxide (CNO)	hM3Dq	Gq	5 mg/kg (i.p.)	0.9% saline	Cayman Chemical
TCB-2	5-HT_{2A} (*Htr2a*)	Gq	1 mg/mL (i.c.)	0.9% saline	Tocris Bioscience
CCK Octapeptide, sulfated (CCK8S)	CCK_1R (*Cckar*)	Gq	1 mg/mL (i.c.)	0.9% saline	Abcam
Substance P	NK_1R (*Tacr1*)	Gq, Gs	1 mg/mL (i.c.)	0.9% saline	Cayman Chemical
Senktide	NK_3R (*Tacr3*)	Gq	1 mg/mL (i.c.)	0.9% saline	Cayman Chemical
SKF-83959	D_5R (*Drd5*)	Gs	1 mg/mL (i.c.)	0.9% saline containing 5% DMSO	Tocris Bioscience

Table S3.2. Key Resources Table

Type	Designation	Source or reference	Identifiers
Mouse strains	Oprm1-Cre:GFP	Laboratory of Dr. Richard Palmiter	N/A
	Wild type C57BL/6J	Jackson Laboratory	Stock No. 000664
	RiboTag *Rpl22*$^{HA/HA}$	Jackson Laboratory	Stock No. 011029
	Ai14 *Gt(ROSA)26Sor*$^{tm14(CAG-tdTomato)Hze}$	Jackson Laboratory	Stock No. 007914
Virus	AAVDJ-CAG-Cre-GFP	Salk Institute Viral Vector Core	N/A
	AAVDJ-CAG-GFP	Salk Institute Viral Vector Core	N/A
	AAV-hSyn-DIO-mCherry-T2A-FLAG-hOprm1	Laboratory of Dr. Matthew Banghart	N/A
	AAV1-syn-FLEX-jGCaMP7s-WPRE	Addgene	Addgene# 104491
	AAVDJ-EF1a-DIO-hM3D(Gq)-mCherry	Salk Institute Viral Vector Core	Addgene# 50460
	AAV-DIO-KORD-mCitrine	Laboratory of Dr. Richard Palmiter	N/A

Table S3.2. Key Resources Table, continued

Type	Designation	Source or reference	Identifiers
	AAV1-DIO-eYFP	Laboratory of Dr. Richard Palmiter	N/A
Antibodies	Anti-hemagglutinin1.1, mouse (1:1000)	BioLegend	RRID AB_2565335
	Anti-GFP, chicken (1:1000)	Aves Labs	RRID AB_2307313
	Anti-MOR, rabbit (1:1000)	ImmunoStar	RRID AB_572251
	Alexa Fluor® 647-conjugated Donkey Anti-Mouse IgG (1:1000)	Jackson ImmunoResearch Laboratories	RRID AB_2340863
	Alexa Fluor® 488-conjugated Donkey Anti-Chicken IgY (1:1000)	Jackson ImmunoResearch Laboratories	RRID AB_2340375
	Alexa Fluor® 647-conjugated Donkey Anti-Rabbit IgG (1:1000)	Jackson ImmunoResearch Laboratories	RRID AB_2492288
RNAscope probes	Oprm1	Advanced Cell Diagnostics	315841
	Htr2a	Advanced Cell Diagnostics	401291
	Cckar	Advanced Cell Diagnostics	313751
	Drd5	Advanced Cell Diagnostics	494411

Table S3.2. Key Resources Table, continued

Type	Designation	Source or reference	Identifiers
	Tacr3	Advanced Cell Diagnostics	481671
	Tacr1	Advanced Cell Diagnostics	428781
	Cre	Advanced Cell Diagnostics	402551
	Slc17a6	Advanced Cell Diagnostics	319171
	Slc32a1	Advanced Cell Diagnostics	319191
Chemicals	FluoSpheres 540/560 (10% v/v)	Thermo Fisher	Cat# F8809
	Cholera Toxin Subunit B-555	Invitrogen	Cat# C34776
	Naloxone	Somerset Therapeutics	Cat# 70069007110
	Morphine	Spectrum Chemical	Cat# M1167
	TCB-2	Tocris Bioscience	Cat# 2592
	CCK Octapeptide, sulfated	Abcam	Cat# ab120209
	Substance P	Cayman Chemical	Cat# 24035
	Senktide	Cayman Chemical	Cat# 16721
	SKF-83959	Tocris Bioscience	Cat# 2074
	Clozapine N-oxide	Cayman Chemical	Cat# 16882
	Salvinorin B	Cayman Chemical	Cat# 11488
	2-methylbutane	Fisher Chemical	Cat# O35514

Table S3.2. Key Resources Table, continued

Type	Designation	Source or reference	Identifiers
Software	Doric Neuroscience Studio	Doric Lenses	N/A
	RStudio	RStudio	Version 1.2.5001
	rEDM	https://cran.r-project.org/web/packages/rEDM/	Version 0.7.2
	rEDM	https://ha0ye.github.io/rEDM/	Version 0.7.4
	LabChart	ADInstruments	Version 8
	BZ-X viewer	Keyence	N/A
	OlyVIA	Olympus Life Science	N/A
	PRISM	GraphPad Software	Version 6
	Illustrator	Adobe	Version CS6 and CC2018

Chapter 4: Conclusion

4.1 Significance and future directions

Breathing is a vital behavior that supports basic life functions and plays a role in sensation, emotion, and cognition. Here, we studied how multiple dimensions of breathing—the baseline modulation of breathing, the coordination of breathing with pain and anxiety-like behaviors, and the impact of different pharmacological agents on breathing—are controlled by a group of cells in the pontine respiratory center, PBL^{Oprm1} neurons.

In Chapter 2, we described the roles of PBL^{Oprm1} neurons in baseline breathing modulation, affective pain, and anxiety-like behaviors. Single PBL^{Oprm1} neurons encoded both breathing and pain information, suggesting that these neurons could regulate breathing and pain simultaneously. Serendipitously, we discovered a core-shell pattern composed of two distinct subpopulations of PBL^{Oprm1} neurons that diverge to the pain/emotion center (CeA) and the breathing center (preBötC). Core and shell subpopulations differentially contribute to breathing and pain/anxiety regulation, and they send excitatory projections to each other. This circuit organization could explain why breathing and pain/anxiety are often coupled, for example, during pain-induced hyperventilation.

Why is the coupling between breathing and pain/anxiety beneficial for animals? One possible explanation is that when animals encounter a harmful or threatening situation, a rapid increase in oxygen levels can help them escape danger (Hsia et al., 2013). Besides pain-induced hyperventilation, parabrachial neurons are also critical for coping with metabolic challenges, such as hypoxia (Song and Poon, 2009a) and hypercapnia (Song and Poon, 2009b), by inducing shortness of breath and increasing inspiratory drive. Indeed, PBel^{CGRP} neurons, which partly overlap with PBL^{Oprm1} neurons, are required for arousal from sleep during hypercapnia (Kaur et al., 2017). Going further, our results support the idea that PBL^{Oprm1} neurons are a part of the central alarm system in the brain (Palmiter, 2018).

Activating PBL^{Oprm1} neurons triggers behavioral and physiological responses that help animals cope with external threats, like predators, and internal threats, like low oxygen levels.

Another remaining question we have yet to answer is the neural basis for slow breathing-induced hypoalgesia. Human studies have demonstrated that slow breathing reduces pain perception, anxiety, and depression (Busch et al., 2012; Garland et al., 2017; Jafari et al., 2020; Seppälä et al., 2014). During slow breathing, sensory feedback from decreased chest movement could modulate pain perception, presumably through the vagal parasympathetic nervous system (Duschek et al., 2013; Jafari et al., 2017). On the other hand, slow breathing could enhance top-down modulation of brain rhythms, especially in the somatosensory cortex, which subsequently alters the processing of noxious information (Kerr et al., 2013). Our results showed that inhibiting the *Oprm1*$^{PBL\rightarrow preBötC}$ shell neurons did not affect pain and anxiety-like behaviors, whereas inhibiting the *Oprm1*$^{PBL\rightarrow CeA}$ core neurons did. Therefore, we think that slow breathing-mediated hypoalgesia is likely mediated by the cortex or limbic system (Jafari et al., 2017) rather than directly via the shell neurons. Yet, during slow breathing, the core and shell neurons may be simultaneously inhibited by top-down (e.g., the cortex (Grady et al., 2020)) and bottom-up inputs (e.g., the NTS, the primary brain region that receives vagal sensory inputs (Duschek et al., 2013)), allowing the shell neurons to maintain a low breathing rate while the core neurons reduce pain and anxiety-like behaviors.

Our work is an attempt to link the PBL's well-determined role as a hub for pain and aversion (Chiang et al., 2019) with its less-investigated role in respiratory control (Chamberlin and Saper, 1994). Other subpopulations of PBL^{Oprm1} neurons may be involved in cardiovascular control (Chamberlin and Saper, 1992), thermosensation (Nakamura and

Morrison, 2008), gut mechanosensation (Kim et al., 2020), and gustatory-visceroceptive interaction (Chen et al., 2018). How multiple interoceptive functions are converged at the PBL, and whether the information is integrated at the single-neuron or network level, are exciting fields for the future.

In Chapter 3, we further investigated how the same PBL^{Oprm1} neurons are modulated by exogenous opioids, or in other words, how they contribute to the expression and rescue of opioid-induced respiratory depression. We demonstrated this question from genetic, cellular, and transcriptomic perspectives. First, from the genetic level, we showed that the MOR signaling pathway and the *Oprm1* gene expression in the PBL are necessary and sufficient for OIRD. Next, from the cellular level, we monitored breathing over the entire course of OIRD while recording from the PBL^{Oprm1} neurons. We found that systemic morphine injection inhibited PBL^{Oprm1} activity while significantly reducing breathing rate. Subsequently, we performed loss-of-function and gain-of-function manipulation experiments to investigate the necessity and sufficiency of PBL^{Oprm1} neurons in mediating OIRD. Chemogenetic inactivation of PBL^{Oprm1} neurons mimicked OIRD in mice, whereas chemogenetically activating PBL^{Oprm1} neurons following morphine injection rescued respiratory rhythms to baseline levels. Lastly, we leveraged the endogenous GPCR system to manipulate PBL^{Oprm1} neurons and showed a proof of principle of rescuing OIRD by pharmacologically activating these GPCRs. If similar neurons are found in humans, such as the PBel^{CGRP} neurons (de Lacalle and Saper, 2000), we could potentially reduce opioid overdose deaths and guide the development of safer painkillers without respiratory side effects.

We have yet to answer one outstanding question: whether the core and shell neurons contribute to OIRD differentially. A simple experiment is to knock out MOR specifically in each population and measure OIRD responses. Another experiment is to re-activate each

population under excessive morphine (where the local recurrent network might be disrupted and preBötC^{Oprm1} neurons are inhibited) and see whether this manipulation can selectively affect pain or breathing. If so, one can search for GPCRs enriched explicitly in the core or shell neurons with spatial transcriptomics and use similar pharmacological approaches to activate either population. These experiments could potentially guide the design of OIRD treatments without disrupting the analgesic effects.

Moreover, our studies and other research in the field suggest that the OIRD is synergistically mediated by multiple breathing centers, such as the KF (Varga et al., 2020) and the preBötC (Bachmutsky et al., 2020; Baertsch et al., 2021). While the investigations described here primarily focus on the parabrachial nucleus, we believe these studies can guide future investigations into other breathing centers with cell-type-specific circuit dissection approaches.

Another line of future research is how endogenous opioid and other neuromodulator systems regulate PBL^{Oprm1} neurons. Possible sources of endogenous opioids include CeA^{Penk} (Kim et al., 2017), NTS^{Pomc} (Wang et al., 2015), and PB$^{Penk/Pdyn}$ neurons (Norris et al., 2021). Sensors for imaging MOR signaling *in vivo*, which is still under development, will significantly contribute to our understanding of the function of PBL^{Oprm1} neurons. Since PBL^{Oprm1} neurons harbor numerous receptors, they are also good candidates to study the interaction of multiple neuromodulatory systems, which can be learned by simultaneous imaging of engineered biosensors for different neuromodulators.

Taken together, the original work described in this dissertation highlights the PBL^{Oprm1} neurons as a converging point for multiple neuromodulatory systems, and can in turn, give rise to changes in physiology and emotions. Understanding the opioidergic pathways that collectively control breathing, pain, and emotions can provide insights into how different

systems in the brain interact to maintain complex behavioral and physiological homeostasis in response to the changing environment.

4.2 References

Bachmutsky, I., Wei, X.P., Kish, E., and Yackle, K. (2020). Opioids depress breathing through two small brainstem sites. eLife *9*, e52694.

Baertsch, N.A., Bush, N.E., Burgraff, N.J., and Ramirez, J.-M. (2021). Dual mechanisms of opioid-induced respiratory depression in the inspiratory rhythm-generating network. eLife *10*, e67523.

Busch, V., Magerl, W., Kern, U., Haas, J., Hajak, G., and Eichhammer, P. (2012). The effect of deep and slow breathing on pain perception, autonomic activity, and mood processing—an experimental study. Pain. Med. *13*, 215–228.

Chamberlin, N., and Saper, C. (1994). Topographic organization of respiratory responses to glutamate microstimulation of the parabrachial nucleus in the rat. J. Neurosci. *14*, 6500–6510.

Chamberlin, N.L., and Saper, C.B. (1992). Topographic organization of cardiovascular responses to electrical and glutamate microstimulation of the parabrachial nucleus in the rat. J. Comp. Neurol. *326*, 245–262.

Chen, J.Y., Campos, C.A., Jarvie, B.C., and Palmiter, R.D. (2018). Parabrachial CGRP neurons establish and sustain aversive taste memories. Neuron *100*, 891-899.e5.

Chiang, M.C., Bowen, A., Schier, L.A., Tupone, D., Uddin, O., and Heinricher, M.M. (2019). Parabrachial complex: a hub for pain and aversion. J. Neurosci. *39*, 8225–8230.

Duschek, S., Werner, N.S., and Reyes del Paso, G.A. (2013). The behavioral impact of baroreflex function: A review. Psychophysiology *50*, 1183–1193.

Garland, E.L., Baker, A.K., Larsen, P., Riquino, M.R., Priddy, S.E., Thomas, E., Hanley, A.W., Galbraith, P., Wanner, N., and Nakamura, Y. (2017). Randomized controlled trial of brief mindfulness training and hypnotic suggestion for acute pain relief in the hospital setting. J. Gen. Intern. Med. *32*, 1106–1113.

Grady, F., Peltekian, L., Iverson, G., and Geerling, J.C. (2020). Direct parabrachial–cortical connectivity. Cereb. Cortex *30*, 4811–4833.

Hsia, C.C.W., Schmitz, A., Lambertz, M., Perry, S.F., and Maina, J.N. (2013). Evolution of air breathing: oxygen homeostasis and the transitions from water to land and sky. Compr. Physiol. *3*, 849–915.

Jafari, H., Courtois, I., Van den Bergh, O., Vlaeyen, J.W.S., and Van Diest, I. (2017). Pain and respiration: a systematic review. Pain *158*, 995–1006.

Jafari, H., Gholamrezaei, A., Franssen, M., Van Oudenhove, L., Aziz, Q., Van den Bergh, O., Vlaeyen, J.W.S., and Van Diest, I. (2020). Can slow deep breathing reduce pain? An experimental study exploring mechanisms. J Pain *21*, 1018–1030.

Kaur, S., Wang, J.L., Ferrari, L., Thankachan, S., Kroeger, D., Venner, A., Lazarus, M., Wellman, A., Arrigoni, E., Fuller, P.M., et al. (2017). A genetically defined circuit for arousal from sleep during hypercapnia. Neuron *96*, 1153-1167.e5.

Kerr, C.E., Sacchet, M.D., Lazar, S.W., Moore, C.I., and Jones, S.R. (2013). Mindfulness starts with the body: somatosensory attention and top-down modulation of cortical alpha rhythms in mindfulness meditation. Front. Hum. Neurosci. *7*, 12.

Kim, D.-Y., Heo, G., Kim, M., Kim, H., Jin, J.A., Kim, H.-K., Jung, S., An, M., Ahn, B.H., Park, J.H., et al. (2020). A neural circuit mechanism for mechanosensory feedback control of ingestion. Nature *580*, 376–380.

Kim, J., Zhang, X., Muralidhar, S., LeBlanc, S.A., and Tonegawa, S. (2017). Basolateral to central amygdala neural circuits for appetitive behaviors. Neuron *93*, 1464-1479.e5.

de Lacalle, S., and Saper, C.B. (2000). Calcitonin gene-related peptide-like immunoreactivity marks putative visceral sensory pathways in human brain. Neuroscience *100*, 115–130.

Nakamura, K., and Morrison, S.F. (2008). A thermosensory pathway that controls body temperature. Nat. Neurosci. *11*, 62–71.

Norris, A.J., Shaker, J.R., Cone, A.L., Ndiokho, I.B., and Bruchas, M.R. (2021). Parabrachial opioidergic projections to preoptic hypothalamus mediate behavioral and physiological thermal defenses. eLife *10*, e60779.

Palmiter, R.D. (2018). The Parabrachial Nucleus: CGRP neurons function as a general alarm. Trends Neurosci. *41*, 280–293.

Seppälä, E.M., Nitschke, J.B., Tudorascu, D.L., Hayes, A., Goldstein, M.R., Nguyen, D.T.H., Perlman, D., and Davidson, R.J. (2014). Breathing-based meditation decreases posttraumatic stress disorder symptoms in U.S. military veterans: a randomized controlled longitudinal study. J Trauma Stress. *27*, 397–405.

Simon, M.J., Zafra, M.A., and Puerto, A. (2019). Differential rewarding effects of electrical stimulation of the lateral hypothalamus and parabrachial complex: Functional characterization and the relevance of opioid systems and dopamine. J Psychopharmacol *33*, 1475–1490.

Song, G., and Poon, C.-S. (2009a). Lateral parabrachial nucleus mediates shortening of expiration during hypoxia. Respir. Physiol. Neurobiol. *165*, 1–8.

Song, G., and Poon, C.-S. (2009b). Lateral parabrachial nucleus mediates shortening of expiration and increase of inspiratory drive during hypercapnia. Respir. Physiol. Neurobiol. *165*, 9–12.

Varga, A.G., Reid, B.T., Kieffer, B.L., and Levitt, E.S. (2020). Differential impact of two critical respiratory centres in opioid-induced respiratory depression in awake mice. J. Physiol. *598*, 189–205.

Wang, D., He, X., Zhao, Z., Feng, Q., Lin, R., Sun, Y., Ding, T., Xu, F., Luo, M., and Zhan, C. (2015). Whole-brain mapping of the direct inputs and axonal projections of POMC and AgRP neurons. Front. Neuroanat. *9*, 40.